Ab initio and Monte Carlo investigations of structural, electronic and magnetic properties of new ferromagnetic Heusler alloys with high Curie temperatures

Dissertation

zur Erlangung des Grades
Doktor der Naturwissenschaften

an der Fakultät für Physik
der Universität Duisburg-Essen

vorgelegt von
Dipl.-Phys. Antje Dannenberg

Erstgutachter: Prof. Dr. P. Entel
Zweitgutachter: Prof. Dr. J. Neugebauer

Tag der Disputation: 30.08.2011

Contents

List of Figures

List of Tables

1 Abstract

The mechanism which causes many of the unusual thermomechanical properties of martensitic alloys, as for example, superelasticity and the shape-memory effect, is the martensitic transformation. The prototype ferromagnetic shape memory alloy (FSMA) is Ni_2MnGa. But a technological breakthrough is missing due to its poor ductility and low operation temperatures. The goal of this thesis is the proposal of new FSMA appropriate for future technological applications. I focus on X_2YZ Heusler alloys which are mainly based on Mn, Fe, Co, and Ni for the X and Y sites and Z = Ga or Zn. The big challenge of this work is to find material classes which combine the unique magnetomechanical properties of FSMA which are large recoverable magnetostrictive strains, high magnetocrystalline anisotropy energy, and highly mobile twin boundaries with transformation temperatures clearly above room temperature and a reduced brittleness. Such a study, providing material classes which from a theoretical point of view are promising candidates for future FSMA, will help the experimental physicists to select interesting subgroups in the vast number of possible chemical compositions of X_2YZ Heusler alloys.

I have systematically varied the composition in the new Heusler alloys in order to find trends indicating generic tendencies of the material properties, for instance, as a function of the valence electron concentration e/a. A main feature of this thesis is the attempt to find the origin of the competing structural ordering tendencies between conventional X_2YZ and inverse (XY)XZ Heusler structures which are observed for all systems investigated.

In the first part of this work the accuracy and predictive power of *ab initio* and Monte Carlo simulations is demonstrated by reproducing the experimental phase diagram of Ni-Mn-(Ga, In, Sn, Sb). The linear increasing and decreasing slopes of T_M and T_C can be reproduced by total and free energy calculations and the analysis of magnetic coupling constants as a function of the interatomic distances yields insight into the underlying physics. In the second part the focus is on Mn-free Ni-Co-Ga(Zn) and Fe-Co-Ga(Zn) systems. The third part addresses the influence of Zn substitution in $Fe_2CoGa_{1-x}Zn_x$. I discuss the modifications in the structural, electronic, magnetic, and vibrational properties induced by replacing Ga with Zn in terms of e/a. A detailed nearest neighbor analysis allows to explain the strong preference of the cubic inverse over the conventional phase found for the Fe-rich Fe-Co-based systems. In the last part the Ni-Co-Fe-Ga(Zn) systems are presented of which the Ni-Co-Fe-Ga appears to be very interesting. The phonon dispersions of ordered (NiCo)FeGa bear strong resemblance to Ni_2MnGa and a two-fold modulated twin structure emerges in the disordered system rendering this material a very promising candidate for future FSMA purposes.

2 Zusammenfassung

Ein großer Teil der aussergewöhnlichen thermomechanischen Eigenschaften martensitischer Legierungen, wie z. B. der Form-Gedächtniseffekt basieren auf dem martensitischen Phasenübergang. Die typische magnetische Formgedächtnislegierung (FSMA) ist Ni_2MnGa. Ein technologischer Durchbruch konnte jedoch aufgrund von zu niedrigen Curie- und Martensittemperaturen und zu geringer Duktilität noch nicht erzielt werden. Das Ziel dieser Arbeit ist es neue FSMA zu finden, die den technologischen Ansprüchen gerecht werden. In dieser Arbeit werden verschiedene X_2YZ Heusler Legierungen untersucht, in denen die X- und Y- Plätze größtenteils von Mn, Fe, Co und Ni und Z von Ga oder Zn besetzt werden. Eine große Herausforderung stellt dabei die Suche nach Materialklassen dar, die große magnetostriktive Verzerrungen, große magnetokristalline Anisotropieenergie, große Zwillingsgrenzenbeweglichkeit mit Übergangstemperaturen deutlich oberhalb Raumtemperatur verbinden. Eine solche Studie ist eine große Hilfe für Experimentalphysiker, interessante Untergruppen in der überwältigenden Anzahl von Kombinationsmöglichkeiten der Elemente im Periodensystem herauszufiltern. Die Zusammensetzung der neuen Systeme wurde systematisch variiert, mit dem Ziel, Trends in den Materialeigenschaften, z. B. als Funktion der Valenzelektronenzahl e/a zu finden. In einer Vielzahl der Systeme wird eine Konkurrenz zwischen der konventionellen X_2YZ und der inversen (XY)XZ Heusler-Ordnung beobachtet. Ein Hauptaugenmerk dieser Arbeit richtet sich darauf, die Ursachen für diese konkurrierenden strukturellen Ordnungstendenzen zu finden. Im ersten Teil dieser Arbeit konnte die Genauigkeit und Zuverlässigkeit der *ab initio* und Monte Carlo Simulationen durch die Reproduktion des experimentellen Phasendiagramms von Ni-Mn-(Ga, In, Sn, Sb) bestätigt werden. Der linear steigende und fallende Gradient von T_M und T_C kann mittels Berechnung der Gesamt- und der freien Energie und einer genauen Analyse der magnetischen Austauschkopplungskonstanten rekonstruiert werden. Im zweiten Teil konzentriere ich mich auf die Mn-freien Ni-Co-Ga(Zn) und Fe-Co-Ga(Zn) Systeme. Im dritten Teil wird der Einfluss von Zn in $Fe_2CoGa_{1-x}Zn_x$ untersucht und die Modifikationen der strukturellen, elektronischen und magnetischen Eigenschaften in Abhängigkeit von e/a diskutiert. Die Analyse der nächsten Nachbarschaften ermöglicht es, die Ursache für die Bevorzugung der kubisch inversen gegenüber der konventionellen Heusler Struktur herauszufinden. Im letzten Teil wird das interessante Ni-Co-Fe-Ga System vorgestellt. Die Phononendispersion von geordnetem (NiCo)FeGa weist starke Ähnlichkeit zum Prototyp Ni_2MnGa auf und im ungeordneten System beobachtet man eine 2-fach modulierte Zwillingsstruktur. Diese theoretischen Resultate machen Ni-Co-Fe-Ga zu einem vielversprechenden Kandidaten für zukünftige Formgedächtnislegierungen.

3 Introduction

3.1 Martensitic transformations

To provide a comprehensive survey of the state-of-the-art of martensitic phase transformations is beyond the scope of this thesis work. For a more detailed discussion I refer to the literature where the diffusionless, displacive nature of the structural transformation is discussed at length: The book of Z. Nishiyama is very often cited and is mainly based on a discussion of crystallographic data [1]. A. L. Roytburd applied the phase-field concept to develop a non-classical theory of nucleation in solids and a theory of martensitic transformations [2]. The comprehensive work of K. Otsuka and C. Wayman [3] highlights solid-solid transformation processes and associated aspects of pseudoelasticity. In addition, numerous articles and conference proceedings have appeared which cannot be cited here. Among some recent work I would like to cite the following publications: Phase diagrams and their stability, statistical thermodynamics and computational techniques and various aspects of kinetics of phase transitions are discussed in a series of overviews in [4, 5]. Regarding theory, the book of Yu. A. Izyumov and V. N. Syromyatnikov [6] provides an exhaustive account of Landau's theory of phase transitions with group theoretical arguments. The novel aspect of a strain glass in connection with premartensite and the onset of martensite was proposed by Krumhansl [7]. Various aspects of solid-solid transformations in ceramics, shape-memory and other intelligent materials are discussed by F. E. Fujita and R. W. Cahn [8] and microstructure aspects of martensite are outlined by K. Bhattacharya [9].

Here, I only list a few elementary characteristics of martensite. The martensitic transformation is diffusionless and generated by a cooperative movement of atoms. Diffusionless phase transformations are structural transformations in which the atoms change their positions only slightly (typically less than one interatomic distance). In this work the definition of Cohen, Olson and Clapp [10] is used: *Martensitic transformations are diffusionless structural transitions which are shear-dominant and lattice distortive. The morphology and the kinetics are mainly determined by the strain energy.* A martensitic transformation is a solid to solid phase transformation where the structure of the lattice changes abruptly at some composition, temperature, or pressure. This phenomenon is named after the german scientist Adolph Martens [11]. Martensitic phase transformations occur in almost all metallic alloys and pure metals of the group III-IV of the periodic table of the elements [12]. Martensite is usually a non-equilibrium phase which develops when a high-temperature phase is rapidly cooled so that the low-temperature phase cannot develop. The high-temperature symmetric phase is known as

the austenite phase, named after the metallurgist William C. Roberts-Austen, and transforms under cooling into the low-temperature martensite phase with lower symmetry. The martensitic transformation occurs by nucleation and growth, i.e. it is in general of first order (abrupt change of lattice parameters). Martensitic transformations often occur for some critical valence electron concentration (e/a) and accompanying phonon anomalies can be important. Since a martensitic material is produced by cooperative atomic movements, many lattice imperfections such as dislocations, stacking faults and twin faults are induced. The ability of a material to form microstructures and to change them gives martensitic materials their unique properties. One distinguishes thermoelastic (reversible) from athermal martensitic transformations. A thermoelastic martensitic transformation is achieved if martensite grows continuously if the temperature is lowered and vanishes continuously if the temperature is raised [13]. The thermoelastic transformation requires that the "chemical driving energy" and the stored elastic energy (resistive energy) proceed more or less in equilibrium. The transformation may change to a "burst" transformation whenever the chemical driving forces exceed the resistive forces. The athermal transformation (as in most steels) proceeds only if the temperature is changing and the reaction stops when the temperature is halted. The TTT (time-temperature-transformation) phase diagrams allow to discuss the amount of isothermal martensite as a function of the holding time and temperature [14, 15]. The so called shape memory materials (introduced in the next section) show a thermoelastic transformation mostly with little hysteresis and volume change from austenite to martensite [1, 3]. The historical example is Fe-C martensite employed for the oldest and most significant technological application: The strengthening of steel.

3.2 Shape memory effect

Shape memory alloys are based on martensitically transforming materials. A whole series of materials undergoes a martensitic transformation, however, only few display the shape-memory-effect (SME). The shape memory alloys (SMA) thus form a subgroup of all alloys undergoing a martensitic transformation. The shape-memory-effect is schematically illustrated in Fig. 3.1. At high temperature the SMA is in the austenitic phase (Austenite), see Fig. 3.1(a). Under cooling any square of the crystal lattice changes into a rectangle as in Fig. 3.1(b). The low-temperature phase has multiple symmetry-related variants (a variant is something a little different from others of the same type) of martensite, see Fig. 3.1(b), (c). In order to avoid strain and energy consuming volume deformations, the crystal makes a mixture of the different symmetry-related variants to form a complex and very specific pattern at a length-scale much smaller than the size of the specimen. This is the characteristic microstructure of martensite (twins), compare Fig. 3.1(d). In the martensite phase the material can be easily deformed (Martensite1 $\rightarrow$ Martensite 2) by converting one variant into another, see Fig. 3.1(e). If the solid is heated up again, at a critical temperature the crystal structure changes back to the symmetric high-temperature austenite phase. To give an example, I show in Figure 3.2(a) and (b) surface topography images of the martensitic twin structure of a $(Ni_{51}Mn_{28}Ga_{21})_{99.5}Dy_{0.5}$ single crystal

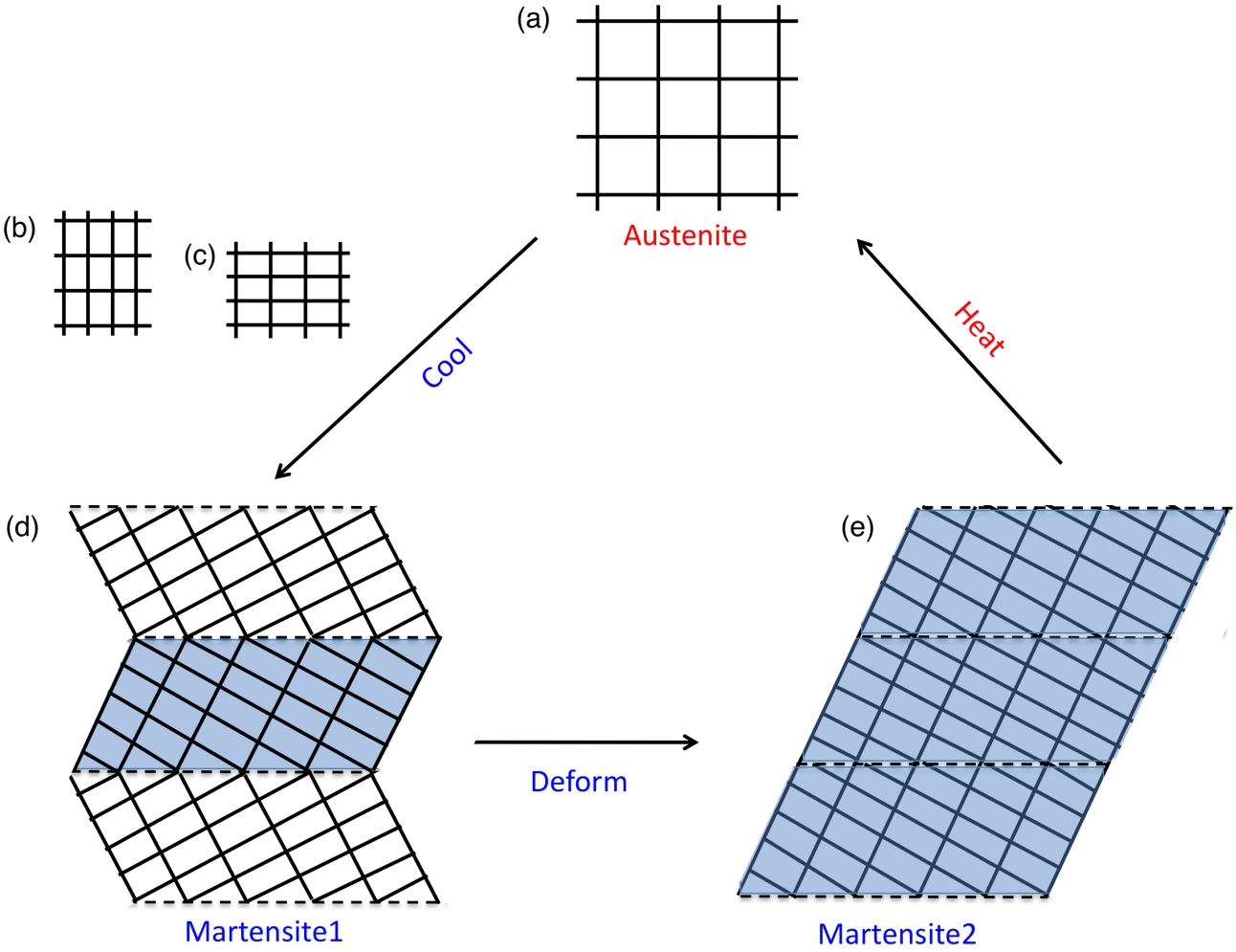

Figure 3.1: The shape-memory effect: Explained schematically involving the martensitic phase transformation. (a) The cubic lattice of the austenitic high temperature, high symmetry phase. Each square transforms under cooling into one of the three different rectangular variants of the low-temperature, lower symmetry martensitic phase (b), (c). During the transformation into a self-accommodated microstructure of martensite the overall shape of the specimen does not change. (d) The characteristic microstructure resulting from a coherent arrangement of alternating variants of martensite. (d) $\rightarrow$ (e) A shape memory material is deformed in the martensitic low-temperature phase by converting one variant (Martensite1) into another (Martensite2) leading to a different arrangement of variants. (e) $\rightarrow$ (a) Under heating it recovers the deformation (Austenite).

recorded with an atomic force microscope [16]. A hierarchical twin structure is displayed with twins formed on three length scales corresponding to three hierarchical levels (twins within twins). Across the boundaries of the large twins, the intermediate twins form a pattern such as given schematically in Fig. 3.2(c). Fig. 3.2(b) shows the three-dimensional representation of the surface relief where the height component is enlarged. The SME requires special changes in symmetry and delicate relations

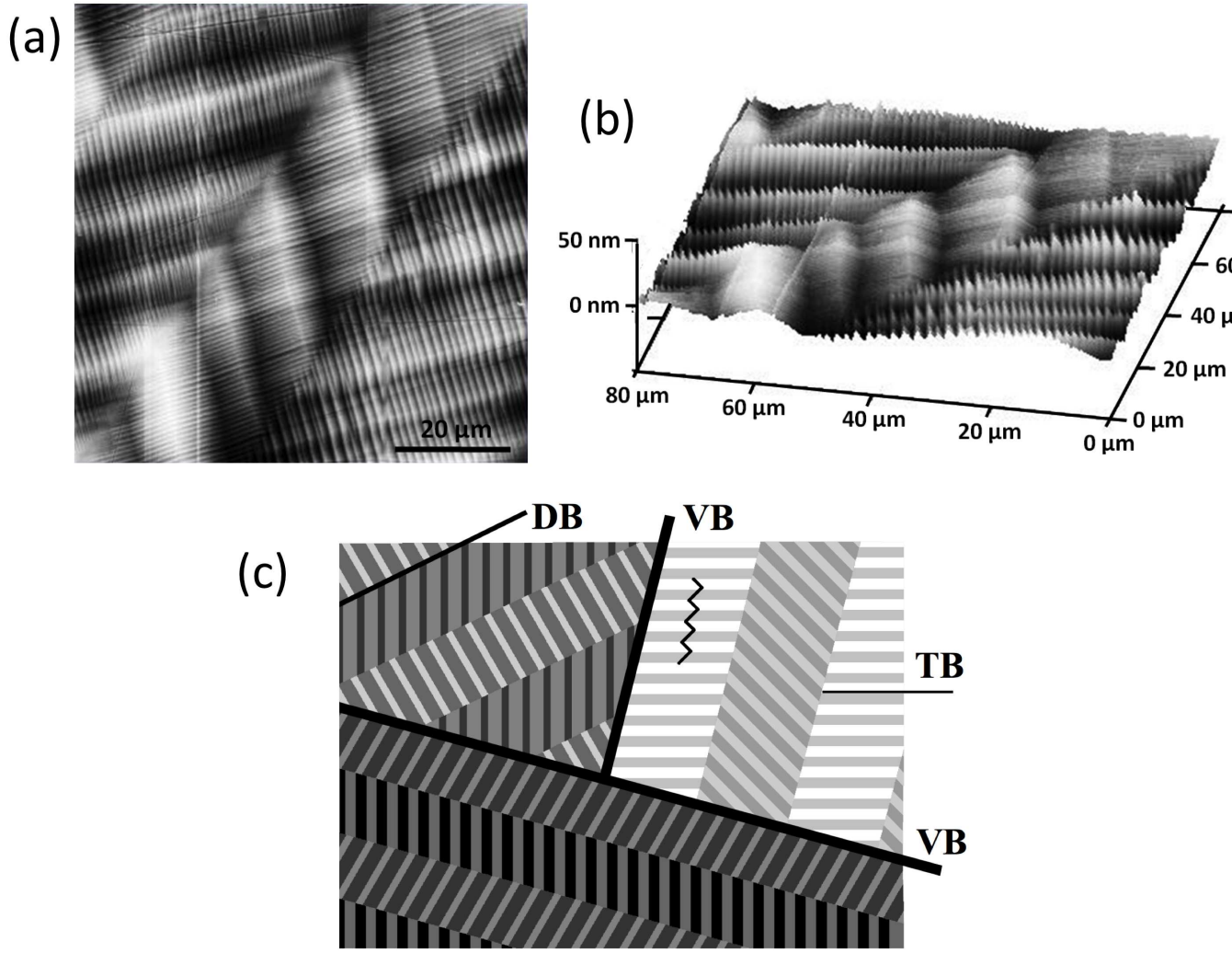

Figure 3.2: (a) Twin structure of a $(Ni_{51}Mn_{28}Ga_{21})_{99.5}Dy_{0.5}$ sample. (a) Top view, and (b) three dimensional view. Three different hierarchies of twins are present. There are four large twins with a thickness of 20 - 40 μm and twin boundaries extending from bottom left to top right. The large twins accommodate intermediate twins with thicknesses between 5 and 15 μm. The intermediate twins form a zigzag pattern across the boundaries of the large twins. Within the intermediate twins there are small twins with thicknesses of 1 to 2 μm. The angles between the twin slopes of the small twins indicate the 14M structure [16, 17], compare Fig. 3.6. (c) Schematic picture of the microstructure of $Ni_{51}Mn_{28}Ga_{21}$ martensite. The austenitic phase single crystal transforms into martensite variants which are separated by variant boundaries (VB). Each variant is composed of domains and domain boundaries (DB) whereas each domain contains twins and twin boundaries (TB). Within one domain, the *c* direction makes a zigzag pattern (indicated by the zigzag line) controlled by the twin structure.

between the lattice parameters. Shape memory alloys undergo a reversible martensitic transformation. Reversibility can be assured if (i) the transformation is of second order, e.g. order-disorder, magnetic or dielectric transformations, or (ii) the transformation is of first order under the condition that the lattice constants of the parent and product structures permit the martensite to grow in the austenite phase without creating long range stress.
The conditions on the lattice parameters that are associated with reversible SME are: Special lattice parameters that allow (i) the existence of martensitic microstructures that give great flexibility to change volume fractions of martensite, (ii) compatibility between austenite and martensite.
Applications are essentially limited to Ni-Ti for a variety of reasons. The high cost of NiTi as well as the narrow temperature range in which it can be used gives rise to the intense search for new materials with better properties applicable for future shape memory actuator devices such as Ni-Nb-Ti. At present, Ni-Ti alloys are the most used non-magnetic shape memory alloys. In order to complete this short discussion of SME one should note that Fig. 3.2 illustrates the so called one-way shape memory effect where the material is plastically deformed below T_M^F (martensite final temperature) and recovers its shape when heated above T_A^F (austenite final temperature). If subsequent cooling below T_M^S (martensite start temperature) shows an unchanged shape one defines this as the one-way shape memory effect. On the other hand, if it immediately deforms when cooling below T_M^S into the shape that it had after the initial plastic deformation, the effect is defined as two-way shape-memory effect [13].

3.3 Magnetic shape memory alloys

Ferromagnetic shape memory alloys (FSMA) form a subgroup of SMAs. They change shape under magnetic fields. These materials are of particular interest as the magnetic response tends to be faster and more efficient than temperature- or pressure-induced responses. Heusler alloys (the definition will be given in section 3.4) are a class of materials forming magnetic shape memory alloys (MSMAs). MSMAs should possess the following properties if suited for large-scale applications in devices:
(a) At room temperature they should be martensitic and ferromagnetic,
(b) the magnetic moment should be large in order to minimize the required external field.
In the following, two actuation mechanisms are distinguished. First, the so called magnetically induced reorientation (MIR) for which high magnetocrystalline anisotropy and highly mobile twin boundaries are required. In this actuation mechanism the direction of the magnetic field influences the orientation of the crystallographic axis. Under an external magnetic field the alignment of the magnetization parallel to the field is energetically favored. But the strong magnetocrystalline anisotropy energy hinders the rotation of the magnetization. Instead, variants with their easy axis aligned parallel to the field grow at the cost of variants with their easy axis oriented perpendicular to the field, cf. Fig. 3.3. This is achieved by twin boundary movement. Therefore, the MIR affects the microstructure of the sample but not its structure in the sense that no phase transformation is involved contrary to

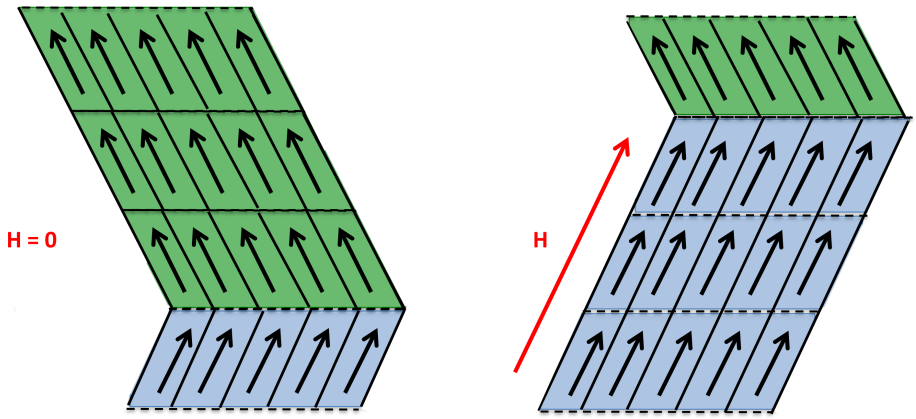

Figure 3.3: A schematic representation of the magnetic induced reorientation (MIR). Variants with their easy axis aligned parallel to the external field H grow at the cost of other variants with energetically unfavorable magnetization axis alignment with respect to the field.

thermally activated SMAs and to the second actuation mechanism (see below) which is called magnetically induced martensite (MIM).
In MIM a magnetic field is used to control the structure of the sample. In contrast to the MIR, in MIM only weak anisotropy is needed. The phase transformation can be induced because austenite and martensite have different spontaneous magnetizations, see Fig. 3.4. On cooling, the material starts to transform martensitically at a given start temperature T_M^S. When the whole specimen has transformed martensitically the martensite final temperature, T_M^F, is observed. Under an external field the phase with the higher magnetization is favored. For further details concerning the two different actuation mechanisms see [18].

3.4 Ferromagnetic Heusler alloys

In 1903 Heusler for the first time reported that the fabrication of ferromagnetic alloys was feasible by coalloying Mn-Cu with Sn, Al, As, Sb, Bi, or B [19]. This is especially remarkable as none of the constituent elements is itself ferromagnetic in its bulk equilibrium structure. The first prototype Heusler alloy was Cu-Mn-Al. Heusler alloys are characterized by a strong relationship between composition, (X_2YZ), and chemical order, ($L2_1$), and magnetic properties.

3.4.1 Crystal structure and symmetry relations

Heusler alloys are defined as ternary intermetallic compound where at stoichiometric composition X_2YZ the crystal symmetry $L2_1$, see Fig. 3.5(a).
The $L2_1$ unit cell is of space group $Fm\overline{3}m$ (O_5^h) while the whole crystal has only tetrahedral symmetry T_d. X and Y are transition metals and Z is usually a covalently bonding element of the main group

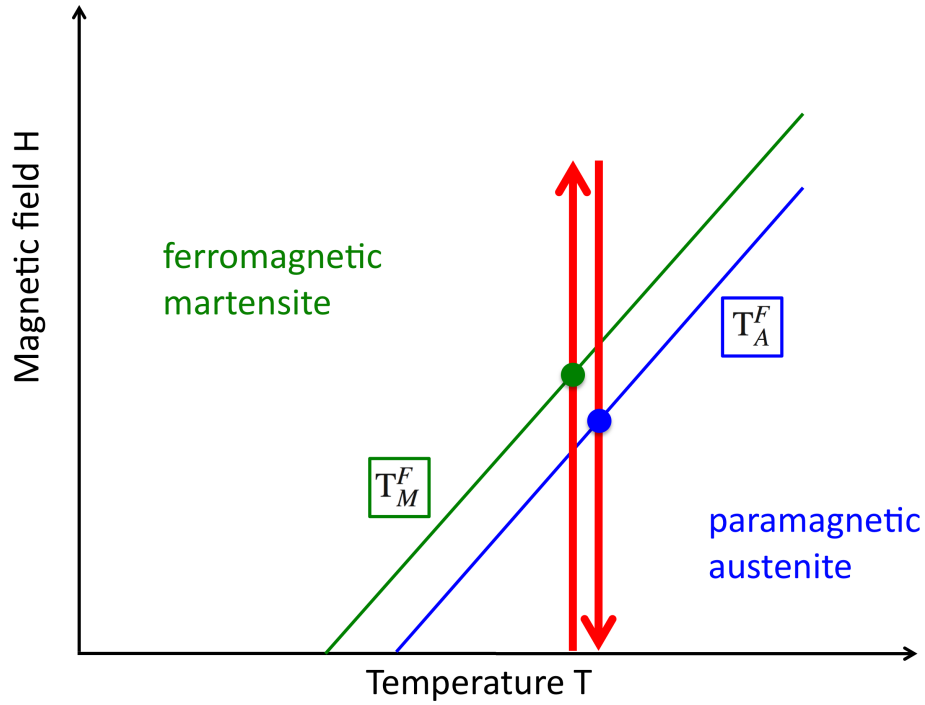

Figure 3.4: Schematic phase diagram separating the existence ranges of a ferromagnetic martensitic phase and a paramagnetic austenitic phase in dependence of temperature T and magnetic field H. T_M^F and T_A^F mark the martensitic and austenitic finish temperature, respectively. The arrows indicate a field cycle for Magnetically Induced Martensite (MIM) actuation at a constant temperature above T_M^F (at $H = 0$). The points mark the regions where the direct and reverse martensitic transformation occur. Figure adapted from [18]

III-V[20, 21]. In Fig. 3.5(a - c) the site occupancy of full (X_2YZ) and half (XYZ) Heusler alloys is shown. The unit cell of the $L2_1$ phase can be constructed by four interpenetrating fcc sublattices A, B, C, and D with origins at (0, 0, 0), (1/4, 1/4, 1/4), (1/2, 1/2, 1/2), and (3/4, 3/4, 3/4). Simultaneously, the Heusler structure is bcc-like as it can be formed from the ordered combination of two binary B2 compounds XY and XZ with CsCl structure. The B2 structure has 8-fold coordination and is the most common type of disorder as a function of temperature. During the experimental manufacturing process the specimen is cooled down from the completely disordered A2 phase at high temperatures. For Ni_2MnGa the Ni atoms order first and consequently build a B2 phase with the Y and Z atoms still randomly distributed on the other cubic sublattice. Depending on the rate of cooling it may happen that the diffusion of the atoms is hindered and the high temperature disordered phase is frozen (quenching). Thus, under rapid cooling the evolution of the ordered $L2_1$ Heusler structure may be kinetically blocked even if it is energetically favored at $T = 0$ K.

There are a lot of combination possibilities of distributing the four different sorts of atoms on the four sublattices. To give an impression here only the most preferential types of atomic order are shown in Fig. 3.5 (a - c). Apart from the common $L2_1$ Heusler structure shown in Fig. 3.5(a) the so called

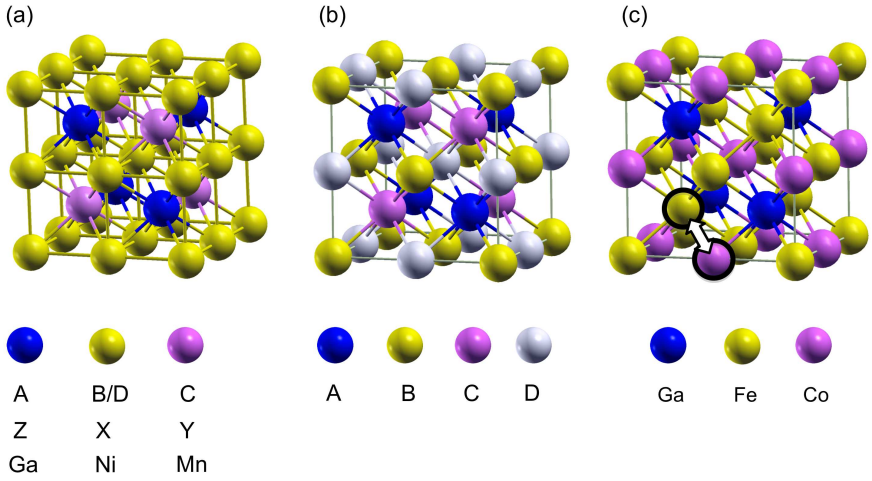

Figure 3.5: (a) The Heusler $L2_1$ structure with a unit cell of space group $Fm\overline{3}m$ (O_5^h) for Ni_2MnGa which consists of four interpenetrating fcc sublattices A, B, C, and D. Sites A and C have point symmetry $m\overline{3}m$ (octahedral site) and the B and D sites have point symmetry $\overline{4}3m$ (tetrahedral site). (b) Important possibilities of other ordered structures besides the Heusler phase formed from four interpenetrating fcc sublattices: A2: All lattices identically filled which corresponds to complete disorder, B2: A filled as C, B filled as D yielding a CsCl-like lattice, B32: A filled as B, C filled as D, $L2_1$: B filled as D DO_3: A, C, and D identically filled, C1: D filled as B, C void, $C1_b$: C void, Inverse Heusler structure (XY)XZ: B and C filled with X, D filled with Y, and A filled with Z, (X1X2)YZ: Quaternary Heusler structure with 2 distinct X sublattices. (c) Inverse Heusler structure (XY)XZ as in the case of (FeCo)FeGa.

inverse Heusler structure (XY)XZ is essential in which one of the X-sublattices is occupied with Y while the displaced X atoms consequently sit on the Y-sites, see Fig. 3.5(c). Thus, the brackets in (XY)XZ indicate that the atoms X and Y now occupy the X_2 lattice sites while X and Z occupy the Y- and Z-lattice sites of the conventional X_2YZ structure. Recent DFT calculations show that this inverse Heusler order is competitive to the conventional X_2YZ Heusler structure in some alloys [22–25]. Concerning site preference and structural ordering the Mössbauer study of Jaggi *et al.* revealed that transition metal atoms to the left of Fe in the periodic table preferentially occupy the Y site (as Mn in Ni_2MnGa) while those to the right of Fe prefer to sit on the X sublattice (as Ni in Ni_2MnGa). In this work, the attempt is made, to find the origin of this structural ordering trend.

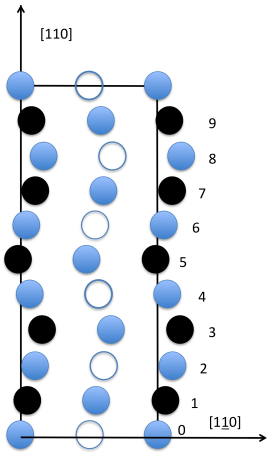

Figure 3.6: Schematic projection on the x/y plane of the 5M (10M) modulated structure for the case of Ni_2MnGa. Blue circles mark Ni atoms, white circles Mn and black circles Ga atoms. "M" refers to the monoclinicity resulting from the distortion associated with the modulation. The 7M (14M) modulated structure can be constructed accordingly.

3.4.2 Experimental and theoretical background

Relevant for the magnetic shape memory effect are the modulated 5M and orthorhombic-like 7M phases (cf. Fig. 3.6) for which the *c*-axis is shorter than the *a*-axis, i.e. the c/a ratio is smaller than one. Another experimentally observed structure is tetragonal (bct) without any modulation and a c/a larger than 1. In an recent attempt, these mircomodulated structures have been described by an adaptive martensitic phase. This means that the $c/a < 1$ modulated structure can be conceived from the non-modulated $c/a > 1$ structure, see Fig. 3.7. A short introduction to the concept of adaptive martensite is given in the Appendix 11.3. Materials which significantly change their mechanical properties (such as shape, stiffness, and viscosity) in response to their environment are called smart materials. These materials can be used in actuator and sensor devices, e.g., piezoelectric, electrostrictors, magnetostrictors, and shape-memory devices. The outstanding properties of these smart intermetallics are based on the interplay of structural and magnetic order. The large magnetomechanical coupling and the highly mobile twin boundaries in the modulated 5M and 7M martensites [26] allows the twin variants to be reoriented by an external magnetic field which yields large magnetic field induced strains.

Ferromagnetic Heusler alloys like Ni-Mn-Z with Z = Al, Ga, In, Sn, Sb undergo a martensitic phase transformation and are subject of intense research with respect to technological applications involving actuator and magnetocaloric devices since the mid 1990s [28, 29]. The magnetic shape memory effect and the magnetocaloric effect have been recently discussed by Acet *et al.* [30]. A variety of new FSMA's have recently been proposed, among them are Co-Ni-(Al, Ga) [31–38], Ni-Fe-Al [39, 40], and Cu-Mn-(Al, Ga) [41, 42]. The alternative family of ferromagnetic full Heusler alloys like Co-Mn-Z with Z = Al, Ga, In, Sn, Sb are half-metallic, do not exhibit a structural phase transformation, and

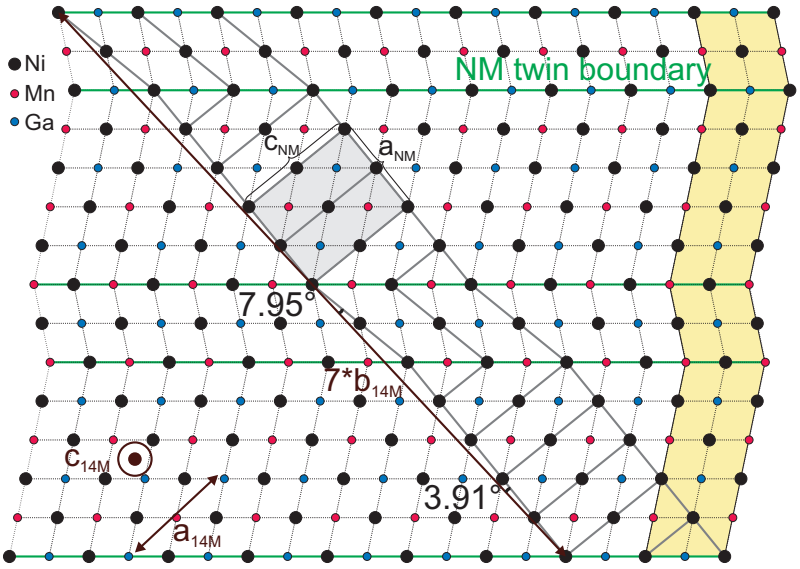

Figure 3.7: 14M structure constructed by periodic twinning of tetragonal non-modulated (NM) building blocks. One of the NM cells is marked with grey background. The angles of the NM unit cells subtended with the 14M supercell (thick lines) are given. The conventional unit cell used to describe the 14M within the bct reference system is marked with a yellow background at the right. Figure adapted from [27].

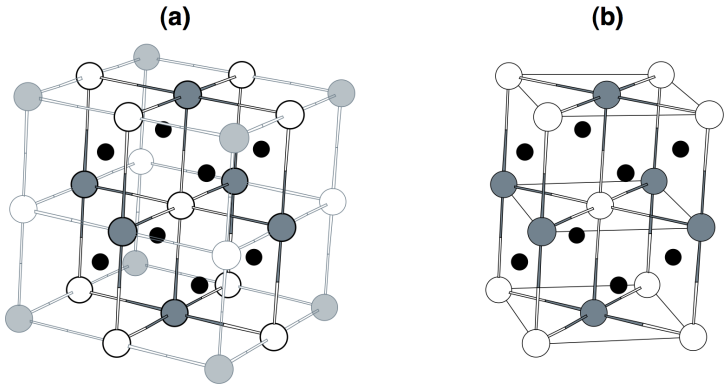

Figure 3.8: (a) Cubic $L2_1$ Heusler structure and (b) tetragonally distorted bct structure for Ni_2MnGa. White spheres denote Mn, gray spheres belong to Ga, and black spheres mark the Ni atoms.

are of more interest for future spintronic devices [43]. The prototype FSMA Ni_2MnGa undergoes a martensitic transformation from the cubic $L2_1$ to the tetragonal bct structure ($L1_0$), cf. Fig. 3.8. When bcc solids approach a martensitic transformation usually an anomalous temperature behavior of the elastic constants and the dynamical response of the lattice is observed [44, 45]. All bcc martensitic materials exhibit a low in energy lying TA_2 [110] phonon branch. A very short introduction to phonons is given in the Appendix 11.1. In Ni_2MnGa this phonon branch softens when approaching the marten-

Table 3.1: Experimental and theoretical data for the elastic stiffness constants at 300 K of near-stoichiometric Ni_2MnGa and orthorhombic Cu-Zn-Al in units of 10^{12} dyn/cm^2 (10^2 Gpa).

	Ni_2MnGa					Cu-Zn-Al
	Experiment		*Ab initio*			*Ab initio*
C_{ij}	Ref. [56]	Ref. [44]	Ref. [56]	Ref. [52]	Ref. [51]	Ref. [55]
C_{11}	1.52	1.36		1.63	1.73	1.76
C_{12}	1.43	0.92		1.51	1.41	1.12
C_{44}	1.03	1.02		1.11	0.99	0.53
C'	0.045	0.22	0.04	0.061	0.159	
C_L	2.50	2.22		2.68	2.566	
B	1.49	1.21		1.59	1.519	

sitic transition and is accompanied by developing a mircomodulated structure [46, 47]. If a particular lattice vibrational mode becomes small or even zero, then the crystal transforms. Phonon softening is often considered as a precursor phenomenon of the premartensitic or martensitic transformation, although, in general, it is not a mandatory precondition for the occurrence of a martensitic transformation, e.g. in $Co_{48}Ni_{22}Ga_{30}$ a martensitic transformation is observed without any sign of phonon softening [48]. Nevertheless, the phonon dispersion curves yield important additional informations concerning structural stability and are presented in this work for some representative cases. Many displacive solid-solid transformations show pronounced precursor effects, such as the mesoscopic, micron-scale, "tweed" pattern seen in shape-memory alloys. The spin-glass nature of this tweed precursors in martensitic transformations is discussed in [7, 49]. A further precursor phenomenon is the softening of the elastic constants as mentioned above. During the transition of prototype Ni_2MnGa an extraordinarily large softening of $C' = (C_{11} - C_{12})/2$ (around 60%) was observed [46]. In a simplified picture, C' can be seen as the resistance against shearing stress across the {110} plane in [110] direction in a cubic crystal [50]. For a better understanding of the structural transition, the elastic constants of importance can be calculated by straining the cubic $L2_1$ and the tetragonally distorted structures [51, 52]. In the context of elastic constants one has to mention the very famous paramagnetic shape memory alloy Cu_2ZnAl which shows rubber-like behavior [53] and has been subject to intensive experimental and theoretical work due to its very peculiar thermomechanical properties, the pseudoelasticity and the shape memory effect [54, 55]. In Table 3.1 a comparison between the experimental and theoretical elastic constants of near-stoichiometric Ni_2MnGa and orthorhombic Cu-Zn-Al at room temperature are given. For Ni_2MnGa also the longitudinal constant $C_L = (C_{11} + C_{12} + 2C_{44})/2$ and the bulk modulus $B = (2C_{11} + C_{12})/3$ are listed and good agreement is found between the experimental values and the results from *ab initio* calculations.

Although Ni_2MnGa shows a large strain up to 10% in a magnetic field less than 1 T [57] it is not perfectly suitable for technological applications since the operation temperatures are too low (the martensitic transition occurs at $M_S \approx 200$ K for the near-stoichiometric samples and $M_S \approx 350$ K for the technologically relevant $Ni_{50}Mn_{30}Ga_{20}$) and the material is rather brittle. Higher T_M can be

achieved when Ga is partially substituted by Mn, but this has the disadvantage of simultaneously lowering the Curie temperature T_C and is unfavorable for the MSME as the additional Mn-atoms induce antiferromagnetic correlations [58, 59]. In addition, single crystals are needed for actuator devices. Thus, a technological breakthrough is still missing and new material combinations with improved elastic properties and higher Curie and martensite transformation temperatures are required.

3.4.3 In search for new FSMA

At present, ferromagnetic shape memory alloys are subject of intense research due to their potential use for actuator and sensor applications. In this work the attempt is made to find new systems while simultaneously avoiding manganese due its disadvantageous antiferromagnetic tendencies. The proposal is to start from well known binary cubic alloy systems which already show martensitic tendencies. Promising binary systems are, e.g., Fe_3Ga [60–62], Co_3Fe [63], CoGa [64], CoZn [65, 66], FeZn [65–67], and FeGa [68, 69].
Information about systematic trends of the electronic properties of Heusler alloys can be gained by considering the dependence on the valence electron concentration per atom e/a. In off-stoichiometric Ni-Mn-Ga alloys the martensitic transformation temperature T_M shows a linear dependence on e/a and can be considerably enhanced by increasing the e/a ratio [59]. Thus, the e/a ratio can be considered as an important parameter which controls T_M and the magnetic correlations, although, in detail, the change of the magnetic properties and the chemical bonding is more sophisticated. Systems with a different e/a ratio than stoichiometric Ni_2MnGa ($e/a = 7.5$) are therefore a first step towards future FSMA with higher T_M. The obstacle when searching for new material combinations avoiding Mn is the occurrence of new phases with different atomic ordering on the four interpenetrating fcc sublattices which can lead to lower energies than the conventional $L2_1$ Heusler structure as in the case for the inverse Heusler phase of Fe_2CoGa, cf. Fig. 3.5(c). But at the same time these new phases are an opening for unexpected and exciting physics. A detailed first-principles combinatorial study was recently performed by Gilleßen *et al.* in which the thermochemical stability of 810 conventional and inverse Heusler alloys is compared [22, 70]. 27 material combinations are found to be more stable in the inverse Heusler structure. But what is missing in this remarkable study with enormous computational effort is the calculation of the Curie temperature, the martensite transformation temperature, and the mixing energy which are important properties determining the applicability of a new material as future FSMA devices. Furthermore, their study does not provide any suggestions for new promising material combinations. This thesis tries to partially fill this gap.

3.4.4 Computational approach to martensitic transformations

For the characterization of the groundstate properties of the alloys under investigation I have performed as a first step total energy calculations as a function of the volume, in order to determine the equilibrium lattice constant and the magnetic configuration at $T = 0$ K. Under the assumption that

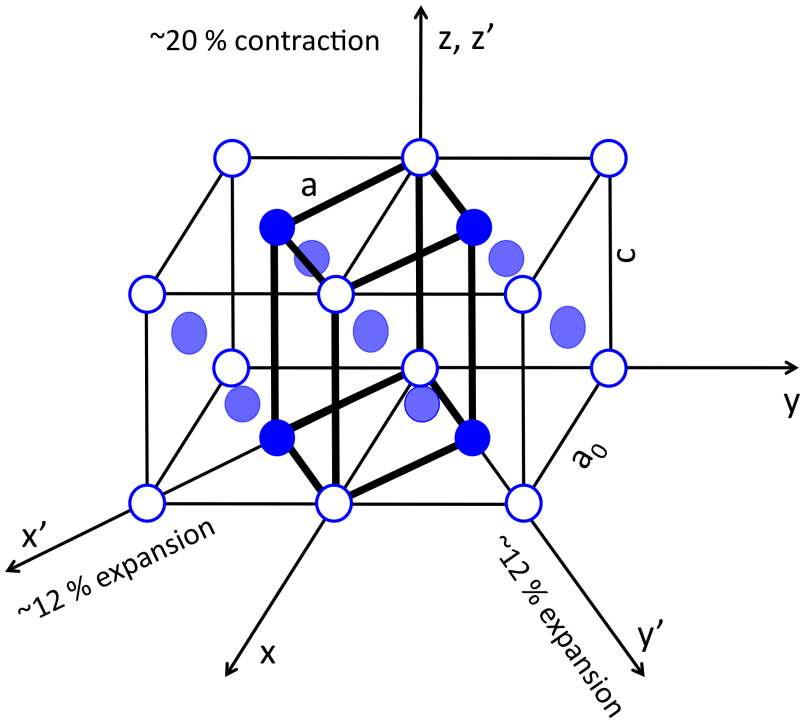

Figure 3.9: Schematic representation of the lattice distortion observed along the Bain path [71] for the fcc $\rightarrow$ bcc transformation. The equilibrium lattice constant of the fcc austenitic phase is labeled with a_0. The unit cell of the martensitic phase ("Bain cell") is emphasized by thick lines. The corresponding lattice constants are labeled with a and c.

the volume of the cubic phase remains constant, which is valid in most case studies i.e. the volume changes along c/a by less than 0.3 %, I have monitored the variation of the total energy as a function of the tetragonal distortion. The shape of the energy curve yields information about the tendency of the material to show a martensitic instability and allows a first estimation if the new materials may be appropriate for future smart material applications. During the continuous change of the c/a-ratio along the Bain path [71, 72], the crystalline lattice transforms from the ideal $L2_1$ lattice ($c/a = 1$) to the fcc-type closed-packed structure ($c/a = \sqrt{2}$), compare Fig.3.9. All first-principles results presented in this thesis have been obtained by using the simulation program VASP (Vienna Ab-initio Simulation Package)(http://cms.mpi.univie.ac.at/VASP/) and the SPR-KKR package [73, 74] which yield very good results compared to full-potential all electron calculations (computational details are given in the chapter 5.4).

For the case that the material shows a tendency to undergo a martensitic transformation, two energy minima are found in the $E(c/a)$ curves, one near or at $c/a = 1$ and a second one at $c/a > 1$. Since the martensitic phase is the low-temperature phase, it may be associated with the absolute energy minimum observed in the *ab initio* calculations. The energy difference between the two energy minima is roughly proportional to the martensitic transformation temperature. Plotting the total magnetic

moments as a function of the c/a ratio yields information about the correlation between magnetism and structural stability.
In order to gain information about the structural stability and segregation tendencies the mixing energy is calculated. The mixing energy can be easily obtained by subtracting the total sum of the bulk energy of material component i weighted by its concentration c_i from the ground state energy of the alloy system :

$$E_{mix} = E_{alloy} - \sum_i c_i E_i. \tag{3.1}$$

Negative mixing energies indicate that the alloys are stable against spinodal decomposition. This does not imply stability against compounds arising from various combinations of the constituents (which are too numerous to consider systematically in the framework of this thesis) but provides meaningful trends with respect to changes in composition.
Information about systematic trends concerning the magnetic properties of the alloys are obtained by the inspection of the magnetic coupling parameters J_{ij} (cf. chapter 5), which are calculated by means of green function based SPR-KKR calculations. Inserting the magnetic exchange parameters J_{ij} into a Monte-Carlo routine allows to determine the Curie temperatures.
Concerning structural ordering I often encountered a competition between the conventional X_2YZ and the inverse (XY)XZ Heusler structure. The question of the potential occurrence of disorder has been addressed for the two most promising alloys, Co_2NiGa and (NiCo)FeGa, by means of a 128 atom supercell calculation with random distribution of atoms on the crystal lattice. For the completely disordered structures a carefully carried out relaxation procedure was especially important. With this, the basic informations for a first characterization of the new materials with respect to their applicability for magnetic shape memory purposes is available.

3.5 Computer simulations based on *ab initio* and Monte Carlo methods

In the last two decades, computer simulations based on a quantum-mechanical description of the interactions between electrons and between atomic nuclei and electrons have attained an enormous impact on solid-state physics, chemistry, and on material science. *Ab initio* calculations at $T = 0$ K allow a deeper understanding of the processes in materials and also permit to design materials for future technologies. A benchmark in the development of *ab initio* methods was the derivation of density-functional theory (DFT) which reduces the complexity of the description in terms of many-electron wavefunctions to an effective one-electron potential which only depends on the electron density. In the pioneering work of Hohenberg and Kohn in 1964 [75] and in a subsequent work of Kohn and Sham in 1965 [76] the many-electron Schrödinger equation was reformulated to the Kohn-Sham equations. The Kohn-Sham equations are the Schrödinger equation for a fictitious system of non-interacting electrons that generate the same density as the given system of interacting particles. With this, the

foundation of computational material research was given. DFT allows not only the determination of bulk properties but also captures investigations of processes on surfaces, molecules and layered systems. The growing request for new concepts in information technology and faster information processing translate in a strong demand on modeling and simulating the electronic structure of the materials under investigation in order to gain a better understanding of the underlying physical properties. This is only possible due the increasing computational capabilities in the last decades. Current state-of-the-art of *ab initio* simulations permits the calculation of hundreds up to 1000 atoms [77].
One of the other common method in the field of computational material research is related to Monte Carlo-based methods which is a statistical approach to solve deterministic many-particle problems. One of the first pioneers in this area and one of the researchers who developed the Monte Carlo method in the 1950s was Metropolis [78]. In chapter 4 an introduction to the basic concepts of density functional theory and a short survey about the main characteristics of the Monte Carlo method are given.

4 Density Functional Theory

Due to the remarkable success for the description of the ground-state properties of large material classes, e.g., simple metals, half-metals, transition-metals, semi metals, semiconductors in different forms like bulk, surfaces and nanostructures, the density functional theory (DFT) has become the computational tool of modern electronic structure theory. In principle, the knowledge of the atomic numbers of the constituent atoms of a system is sufficient for calculating all other groundstate properties by means of the DFT equations. DFT cuts down the intractable problem of the solution of a many-electron Schrödinger equation to a single-electron problem. Instead of the complicated many-electron wavefunction the electron density distribution $n(\underline{r})$ is used as the elementary quantity. Already in 1927 Thomas [79] and Fermi laid the conceptual root of density functional theory with their description of the many-electron system in terms of the electronic density. In 1964, about 40 years later, Hohenberg and Kohn established their famous theorem, which states that all ground-state properties of the many-particle system are uniquely defined by the ground-state particle density $n(\underline{r})$. In this chapter the basic concepts of DFT are introduced following a survey of Zeller [80]. The equations are given with respect to atomic units:

$$e = m_e = \hbar = 4\pi\varepsilon_0 = 1. \tag{4.1}$$

The consideration is restricted to a non-relativistic, non-spin-polarized, time-independent many-electron system at zero temperature which is entirely defined by the wave function ψ. A further simplification can be obtained by neglecting the kinetic energy of the nuclei. This is possible owing to the fundamental differences in the masses of the nuclei and the electrons. The kinetic energy of the heavy nuclei is negligibly small compared to the kinetic energy of the much lighter electrons. This is the so called Born-Oppenheimer approximation in which the non-degenerate ground state ψ is given by the Schrödinger equation

$$\hat{H}\psi = [\hat{T} + \hat{U} + \hat{V}_{\text{ext}}]\psi = [-\frac{\hbar^2}{2m}\sum_{i=1}^{N} \bigtriangledown_i^2 + \sum_{i<j}^{N}\sum U(\underline{r}_i, \underline{r}_j) + \sum_{i=1}^{N} v_{\text{ext}}(\underline{r}_i, \underline{R}^{\mu})]\psi = E\psi, \tag{4.2}$$

where the electron-electron and electron-ion interactions are given by

$$U(\underline{r}_i, \underline{r}_j) = e^2 \left|\underline{r}_i - \underline{r}_j\right|^{-1} \tag{4.3}$$

and

$$v_{\text{ext}}(\underline{r}_i, \underline{R}^\mu) = \sum_\mu \frac{e^2 Z^\mu}{[\underline{r}_i - \underline{R}^\mu]}. \tag{4.4}$$

Here, the static external potential is resulting from the interaction of the electrons with the atomic nuclei μ. Thus, the external potential $v_{\text{ext}}(\underline{r}, \underline{R})$ explicitly depends on the atomic positions {R}. The kinetic energy operator $\hat{T}$ and the interaction operator $\hat{U}$ are universal, i.e. they are the same for any system, while v_{ext} depends on the system and is therefore non-universal.

4.1 The Hohenberg-Kohn Theorems

The external potential v_{ext} completely determines the Hamiltonian of the many-electron system because the electron-electron interaction (Coulomb potential) is known. Consequently, the ground-state wavefunction and the ground-state density of the many-electron system are also completely determined by the external potential. This implies that the ground-state density is a uniquely determined functional of the external potential: $n_0[v_{\text{ext}}(\underline{r}, \underline{R})]$. The first Hohenberg-Kohn theorem [75] states that the mapping from the external potential to the ground state density is reversible up to an additive constant in the potential. This means that the external potential is a functional of the ground-state density $v_{\text{ext}}[n_0(\underline{r}, \underline{R})]$. Since every wavefunction ψ is a functional $\psi[v_{\text{ext}}(\underline{r}, \underline{R})]$ of the external potential, the wavefunction is also a functional of the ground-state density $\psi[v_{\text{ext}}[n_0(\underline{r}, \underline{R})]]$. Thus, every quantum mechanical observable is a functional of the ground-state density. The second Hohenberg-Kohn theorem comprises that for any external potential v_{ext} a unique functional $E[n(\underline{r}, \underline{R})]$ of a trial electron density $n(\underline{r}, \underline{R})$ can be defined which obtains its minimum for the exact ground-state density $n_0(\underline{r}, \underline{R})$ and gives the ground-state energy as $E_0 = E[n_0(\underline{r}, \underline{R})]$. The functional $E[n(\underline{r}, \underline{R})]$ is given by the minimum over all wavefunctions which deliver the density $n(\underline{r}, \underline{R})$.

$$E[n(\underline{r}, \underline{R})] = \min_{\psi \to n} \langle \psi \left| \hat{T} + \hat{U} + \hat{V_{\text{ext}}} \right| \psi \rangle. \tag{4.5}$$

Introducing the functional $F[n(\underline{r}, \underline{R})]$ Eq. 4.5 can be rewritten as

$$E[n(\underline{r}, \underline{R})] = F[n(\underline{r}, \underline{R})] + \int n(\underline{r}, \underline{R}) v_{\text{ext}}(\underline{r}, \underline{R}) d\underline{r} \tag{4.6}$$

in which the functional

$$F[n(\underline{r}, \underline{R})] = \min_{\psi \to n} \langle \psi \left| \hat{T} + \hat{U} \right| \psi \rangle \geq E_0 \tag{4.7}$$

is universal. The ground state energy E_0 is then simply obtained from the variational principle

$$E_0 = \min_n \left(F[n] + \int n(\underline{r}, \underline{R}) v_{\text{ext}}(\underline{r}, \underline{R}) d\underline{r} \right) \tag{4.8}$$

where the search is over all densities which can be constructed from antisymmetric wavefunctions for N electrons. If the exact form of the functional $F[n(\underline{r},\underline{R})]$ would be known, this variational principle would deliver the exact ground-state density $n_0(\underline{r},\underline{R})$ and ground-state energy E_0. However, as the explicit form of the functional is unknown, approximations for $F[n(\underline{r},\underline{R})]$ are required.
Since the external potential explicitly depends on the atomic positions and the electron density, the total energy $E[\{\underline{R}\},\{\psi\}]$ is also a functional of the atomic positions {R} and the electron density $n(\underline{r})$. Minimization of the total energy functional $E[\{\underline{R}\},\{\psi_i\}]$ with respect to the electronic degrees of freedom $\{\psi\}$ leads to the Born-Oppenheimer surface $\Psi[\{R\}]$:

$$\Psi[\{R\}] = \min_{\{\psi_i\}} E[\{\underline{R}\},\{\psi_i\}]. \tag{4.9}$$

On this Born-Oppenheimer surface the atoms move and the resulting changes in the atomic positions lead to forces exerted on the nuclei. These forces become especially important in case of structural optimization proceedures. The force F^μ is given by the derivative of $\Psi[\{R\}]$ with respect to the atomic position $\underline{R}^\mu$:

$$F^\mu = -\bigtriangledown_{\underline{R}^\mu} \Psi[\{\underline{R}\}] \tag{4.10}$$

4.2 Kohn-Sham equations

As the functional $F[n(\underline{r})]$ is not known the Hohenberg-Kohn theorems first appeared not to be very helpful for practical applications. But one year later, Kohn and Sham [76] could transform with their pioneering work the rather abstract Hohenberg-Kohn theorems into a practical scheme. The basic idea of Kohn and Sham is the introduction of a fictitious auxiliary non-interacting electron system in which the electrons are affected by an effective external potential $v_{\text{eff}}(\underline{r},\underline{R})$. The constraint for this effective potential is that the resulting density of the non-interacting system equals the density of the true interacting system. The functional $F[n(\underline{r})]$ depends on the electron-electron interaction U. If the electron-electron interaction is set to zero, the total-energy functional can be written as

$$E_s[n(\underline{r})] = T_s[n(\underline{r})] + \int n(\underline{r}) v_{\text{eff}}(\underline{r},\underline{R}) d\underline{r} \tag{4.11}$$

since the functional $F[n(\underline{r})]$ reduces to the kinetic energy functional $T_s[n(\underline{r})]$ of non-interacting electrons. The Euler-Lagrange equation can be derived from the Hohenberg-Kohn variational principle (4.8)

$$\frac{\delta}{\delta n(\underline{r})}\left\{E_S[n(\underline{r})] + \mu\left[N - \int n(\underline{r}) d\underline{r}\right]\right\} = \frac{\delta T_S[n(\underline{r})]}{\delta n(\underline{r}))} + v_{\text{eff}}(\underline{r}) - \mu = 0. \tag{4.12}$$

Here a Lagrange parameter μ ensures that the total charge is conserved, $N = \int n(\underline{r}) d\underline{r}$. If the external potential v_{eff} is known the exact ground-state density $n(\underline{r})$ can be calculated from equation 4.12. This is possible since for non-interacting electrons, $T_S[n(\underline{r})]$ can be constructed by using single-electron

wavefunctions $\varphi_i(\underline{r})$. Then the electron density and the kinetic energy functional T_s read

$$n(\underline{r}) = \sum_i^{\text{occ}} |\varphi_i(\underline{r})|^2 \ , \tag{4.13}$$

and

$$T_s[n(\underline{r})] = \sum_i^{\text{occ}} \int \varphi_i^*(\underline{r}) \Big(-\frac{\hbar^2}{2m} \nabla_{\underline{r}}^2 \Big) \varphi_i(\underline{r}) d\underline{r}. \tag{4.14}$$

In Eq. 4.14 the spatial as well as the spin quantum numbers are represented by i. The summation is done over the lowest N occupied eigenstates with respect to the Pauli principle. The Kohn-Sham equations are obtained by variation of $E[n(\underline{r})]$ with respect to the single-electron wavefunctions (orbitals)

$$\Big[-\frac{\hbar^2}{2m} \nabla_{\underline{r}}^2 + v_{\text{eff}}(\underline{r}, \underline{R}) - \mu \Big] \varphi_i(\underline{r}) = \varepsilon_i \varphi_i(\underline{r}). \tag{4.15}$$

In order to ensure the normalization of the orbitals as $(\varphi_i, \varphi_i) = 1$ the Lagrange parameters ε_i are introduced. The success of the application of the Kohn-Sham equations relies on the quality of the approximation for the effective potential $v_{\text{eff}}(\underline{r}, \underline{R})$. The outstanding idea of Kohn and Sham was to write Eq. 4.6 as

$$E[n(\underline{r})] = T_s[n(\underline{r})] + \int n(\underline{r}) v_{\text{ext}}(\underline{r}, \underline{R}) d\underline{r} + \frac{e^2}{2} \int \frac{n(\underline{r}) n(\underline{r}')}{|\underline{r} - \underline{r}'|} d\underline{r} d\underline{r}' + E_{\text{xc}}[n(\underline{r})] \tag{4.16}$$

in which the last term is the exchange-correlation energy functional $E_{\text{xc}}[n(\underline{r})]$ defined as

$$E_{\text{xc}}[n(\underline{r})] = F_s[n(\underline{r})] - T_s[n(\underline{r})] - \frac{e^2}{2} \int \frac{n(\underline{r}) n(\underline{r}')}{|\underline{r} - \underline{r}'|} d\underline{r} d\underline{r}'. \tag{4.17}$$

Application of the variation principle to 4.16 yields

$$\frac{\delta T_S[n(\underline{r})]}{\delta n(\underline{r})} + v_{\text{ext}}(\underline{r}, \underline{R}) + e^2 \int \frac{n(\underline{r}')}{|\underline{r} - \underline{r}'|} d\underline{r}' + \frac{\delta E_{\text{xc}}[n(\underline{r})]}{\delta n(\underline{r})} - \mu = 0. \tag{4.18}$$

Equation 4.18 is formally equal to the Euler-Lagrange equation 4.12 of the non-interacting electron system when the effective potential is defined by

$$v_{\text{eff}}(\underline{r}, \underline{R}) = v_{\text{ext}}(\underline{r}, \underline{R}) + e^2 \int \frac{n(\underline{r}')}{|\underline{r} - \underline{r}'|} d\underline{r}' + v_{\text{xc}}[n(\underline{r})](\underline{r}). \tag{4.19}$$

Here, the exchange-correlation potential is given as

$$v_{\text{xc}}[n(\underline{r})](\underline{r}) = \frac{\delta E_{\text{xc}}[n(\underline{r})]}{\delta n(\underline{r})}. \tag{4.20}$$

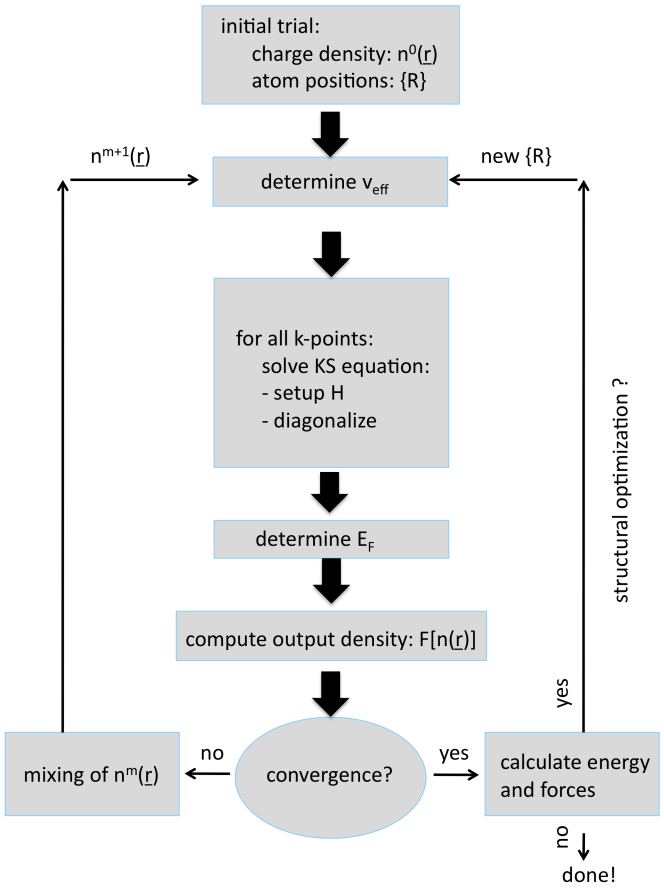

Figure 4.1: Schematic representation of a typical loop structure in density functional codes with self-consistent electronic and structural optimization steps. Figure adapted from [81].

From Eq. 4.19 one derives that the effective potential depends on the density. Vice versa the density depends on the effective potential via Eqs. 4.13 and 4.14. Thus, the famous Kohn-Sham equations have to be solved self-consistently: In a first step the effective potential is determined from a start-trial-density via Eq. 4.19. Then the Eqs. 4.13, 4.14, and 4.15 which are the characteristic Kohn-Sham equations of density-functional theory are solved to construct a new density. This process is repeated over and over again until self-consistency is achieved, implying that the new density does not differ any longer from the old density. If self-consistency for the electron density $n(\underline{r})$ has been observed after N_{iter} number of iterations, the atomic positions are moved in a molecular static or molecular dynamic step, $\{\underline{R}(t)\} \rightarrow \{\underline{R}(t+\Delta t)\}$ in order to optimize the atomic structure. With N_{relax} the number of molecular relaxation steps the eigenvalue problem has to be solved $N_{\text{iter}}N_{\text{relax}}$ times. This procedure is implemented in first-principles codes via a particular loop structure and a particular calculation sequence for the different elements as schematically represented in Fig. 4.1.

4.3 Magnetism

Originally density functional theory has been formulated for the non spin polarized case. But an implementation of magnetism is not too complicated provided that collinear magnetism, i.e. ferro-, ferri, or antiferromagnetism, can be assumed. The ground state has a broken symmetry if magnetism occurs and the functionals depend not only on the ordinary charge density $n(\underline{r})$ but also on the vector-magnetization density $\underline{m}(\underline{r})$. An additional term $\mu_B \underline{\sigma} \cdot B_{xc}(r)$ has to be included in the Kohn-Sham Eqs. 4.16 where μ_B is the Bohr magneton, $B_{xc}(r)$ is the magnetic xc-field acting on the electrons, and $\underline{\sigma}$ are the Pauli spinors. In case of collinear magnetism $\underline{\sigma} \cdot B_{xc}$ reduces to $\underline{\sigma_z} \cdot B_{xc}$ and the magnetization density m_z is given by the spin-up and spin-down densities, $m_z(\underline{r}) = n_\uparrow(\underline{r}) + n_\downarrow(\underline{r})$. The Hamiltonian of this two-dimensional spin-space is a 2×2 matrix and the wavefunctions $\psi_{i\sigma}$ are labeled with an additional spin indices $\sigma = \pm 1$. The calculation of a system bearing collinear magnetism is twice as expensive as the calculation of the corresponding non-magnetic system.

4.4 Approximations for the exchange-correlation energy functional

The challenge of the solution of the Kohn-Sham equations lies in the exchange-correlation functionals $E_{xc}[n(\underline{r})]$ and $v_{exc}[n(\underline{r})]$ in which all of the complicated many-particle problems are hidden. They are not known exactly and have to be approximated. Apart from that, the density-functional theory is exact.

4.4.1 The local (spin) density approximation L(S)DA

A simple approximation, the so-called local (spin) density approximation L(S)DA, has already been proposed in 1965 by Kohn and Sham [76]. This approximation is based upon a fictitious homogeneous electron gas with electron density $n(\underline{r}) = n_\uparrow(\underline{r}) + n_\downarrow(\underline{r})$ in which the charge of the nuclei is described as a positive continuous background charge resulting in an overall neutral system. The exact functional is replaced by

$$E_{xc}^{LSDA}[n(\underline{r})] = \int n(\underline{r}) \varepsilon_{xc}^{LSDA}(n_\uparrow(\underline{r}), n_\downarrow(\underline{r})) d\underline{r}. \tag{4.21}$$

where one assumes that the system acts in any volume element like a homogeneous electron gas with the spin densities $n_\uparrow(\underline{r})$ and $n_\downarrow(\underline{r})$. The origin of the importance of the LSDA relies on the fact that for the homogeneous interacting electron gas with constant density, E_{xc} can be calculated exactly by quantum-mechanical many-body calculations. The function ε_{xc}^{LSDA} is a function of the density and can be divided into two parts, one exchange part and one correlation part

$$\varepsilon_{xc}^{LSDA}(n_\uparrow(\underline{r}), n_\downarrow(\underline{r})) = \varepsilon_x(n_\uparrow(\underline{r})) + \varepsilon_c(n_\downarrow(\underline{r})). \tag{4.22}$$

The exchange part can be given for a system without spin polarization (LDA) by

$$\varepsilon_x(n(\underline{r})) = -\frac{3}{4}\frac{e^2}{\pi}k_F = -\frac{3}{4}e^2\left(\frac{3}{\pi}\right)^{1/3}n^{1/3}. \tag{4.23}$$

If one explicitly considers the spin of the electron, the exchange energy reads

$$\varepsilon_x(n(\underline{r})) = -\frac{3}{4}e^2\left(\frac{6}{\pi}\right)^{1/3}\frac{[n_\uparrow(\underline{r})]^{4/3}+[n_\downarrow(\underline{r})]^{4/3}}{n(\underline{r})}. \tag{4.24}$$

The correlation part is more difficult to calculate but accurate quantum-Monte-Carlo simulations are available from the work of Ceperly and Alder [82].
In case the density is inhomogeneous the so-called generalized-gradient-approximation (GGA) can be applied in which also the gradients of the electron density are taken into account

$$E_{\mathrm{xc}}^{\mathrm{GGA}}[n(\underline{r})] = \int f(n_\uparrow(\underline{r}), n_\downarrow(\underline{r}), \triangle n_\uparrow(\underline{r}), \triangle n_\downarrow(\underline{r}))d\underline{r}. \tag{4.25}$$

The GGA improves for instance the results of the LDA for the cohesive energies and the lattice constants of the 3*d* transition metals. In literature a variety of GGA-functionals exist, among them the functional of Perdew-Wang (PW91) [83] and the functional of Perdew, Burke and Ernzerhof (PBE) [84] which is used throughout this work.

4.5 Pseudopotentials

If the full potential v_{eff} of Eq. 4.19 is used density-functional calculations become numerically expensive and require an enormous computational effort and lead to restrictions, for instance, concerning the size of the unit cell. The invention of pseudopotential-methods was able to partially cure this problem. Here, only the valence electrons which are responsible for the physical properties of the material are taken into account. In the vicinity of the atomic cores the electron wavefunctions show rapid oscillations which cause problems in planewave calculations. A very large number of plane waves are required in order to describe this fluctuations properly. In pseudopotential-methods the Coulomb-potential of the atom is replaced by an artificial auxiliary potential, the pseudopotential. In the pseudopotential-method the atom is regarded as a perturbation of the homogeneous electron gas and the Coulomb repulsion of the nuclear electrons are described via an effective potential which repulses the valence electrons from the nucleus. The resulting wave functions are smooth and plane waves are an appropriate basis set. The pseudopotential must fulfill the constraint that the scattering properties of the ionic nuclei are maintained. The main drawback of the pseudopotential approach is the fact that all information about the charge density and the electron wave function in the vicinity of the nucleus is lost. A solution for this problem could be delivered by the development of the projector augmented wave (PAW) method by Peter Blöchl in 1994 [85]. The interaction between ionic nuclei

and electrons is recovered in the all-electron PAW method which combines the advantages of the augmented wave method with the benefit of the pseudopotential approach. The basis set is a combination of expansions into atomic orbitals at each atom and the so called envelope functions which consist of plane waves, the pseudo wave functions, for the description of the bonding and the tail region. The expansions into atomic orbitals properly describe the nodal structure of the wave functions near the nuclei while the pseudo-wave functions are well suited for the correct description of the bonding and tail regions. This partial solutions are combined at the interface and only valence electrons are included in the calculation. The PAW method provides access to the electron density.

4.6 DFT in practice

As already has been addressed above, in practice, there are always some limitations to some set of model systems. These limitations include the approximations of the unknown $E_{\mathrm{xc}}[n(\underline{r})]$ functional but also include restrictions of system size, neglect of disorder, zero temperature, or the time-scale. But the aim of the numerical investigations is not only to obtain accurate numbers, but rather to gain insight into the underlying physics. The consideration of well-defined, but restricted models, and the investigation of systems in an auxiliary idealized environment which may not be realized in experiments, allows to gain information and understanding of the systems and of the underlying physical questions.

In technologically relevant macroscopic systems as, for examples, a sensor or a central processing unit (CPU), the functionality depends not only on the electronic density but also on the specific crystalline structure on a mesoscopic scale, the formation of defects, clusters, interfaces, textures, and other details of the microstructure. First-principles-calculations as total energy calculations, electronic structure and molecular dynamics simulations deal with length scales of a few to 10^2 chemical bonds between atoms and with time scales defined by interatomic force constants and the resulting atomic vibrations. Thus, an accurate description of material properties requires a multiscale model approach which combines different atomic scale processes, their interdependence and must be capable to involve a very large number of atoms. Figure 4.2 gives a rough overview of the different time and length scales which are of importance for material science modeling including the quantum regime of the electrons, the mesoscopic, and the macroscopic regime. The fundamental elemental processes which determine the basic physical properties of materials take place in the so-called "quantum-regime" and develop over meso- and macroscopic length and time scales.

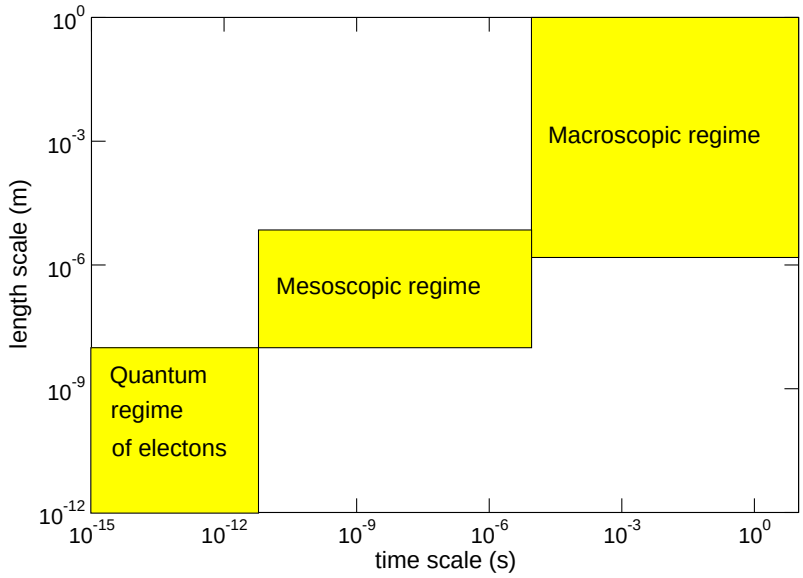

Figure 4.2: Schematic representation of the length and time scales relevant for most material science applications [86]. In the "quantum-regime" the dynamics of the electrons evolve which are decisive for the functionality of the material. Figure adapted from [81].

5 Monte Carlo simulations

Monte Carlo methods are stochastic computer algorithms based on the use of random numbers and probability statistics to investigate problems. They are widely used in statistical physics where systems with many degrees of freedom are handled and rely on random sampling to compute their results. In this chapter the basic concepts of Monte Carlo sampling are introduced. For a more sophisticated review the readers are referred to literature, e.g., the work of Binder *et al.* [87]. In statistical physics mean values of macroscopic observables have to be determined. The Hamiltonian of the system is mostly approximated by a theoretical model description. In the following, two representative examples for model Hamiltonians of magnetic systems are considered. First, a ferromagnet with a very strong uniaxial anisotropy is assumed which can be described by the Ising model, where N spins S_i interact as

$$\hat{H}_{Ising} = -J\sum_{\langle i,j\rangle} S_i S_j - H\sum_{i=1} S_i\,, \quad S_i = \pm 1 \tag{5.1}$$

where the spin S_i at lattice site i can point up or down along the "easy axis", the exchange coupling J accounts only for nearest neighbor interactions and H is the external magnetic field. In case the spins of the ferromagnet are fully isotropic one has to invoke the Heisenberg model (still keeping the length of the spins to "one"):

$$\hat{H}_{Heisenberg} = -J\sum_{\langle i,j\rangle} S_i \cdot S_j - H_z\sum_i S_i^z\,, \quad (S_i^x)^2 + (S_i^y)^2 + (S_i^z)^2 = 1. \tag{5.2}$$

Among the most important average properties which have to be computed from the model Hamiltonian H are the average energy E and the average magnetization M per degree of freedom at a given temperature T:

$$E = \langle H\rangle_T / N\,, \tag{5.3}$$

$$M = \langle \sum_i S_i\rangle_T / N\,. \tag{5.4}$$

The thermal average of any observable $A(\mathbf{x})$ is defined in the canonical ensemble:

$$\langle A(\mathbf{x})\rangle_T = \frac{1}{Z}\int d\mathbf{x}\, \exp[-H(\mathbf{x})/k_B T]\, A(\mathbf{x})\,, \tag{5.5}$$

$$Z = \int d\mathbf{x}\, \exp[-H(\mathbf{x})/k_B T\,. \tag{5.6}$$

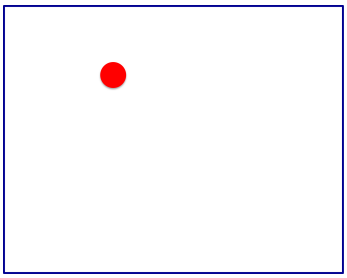

Figure 5.1: Schematic representation of the phase space (blue frame). The red circle represents the states in which the system resides mostly at low temperature. It becomes obvious that a random selection of points is not very useful for an efficient description of the phase space.

The vector $\mathbf{x}$ in phase space represents the set of variables describing the considered degree of freedom, e.g. $\mathbf{x} = (S_1, S_2, S_3, ..., S_N)$ for the Ising Hamiltonian 5.1. A central property of statistical physics is the probability density ρ which describes the statistical weight with which the configuration $\mathbf{x}$ occurs in thermal equilibrium:

$$\rho(\mathbf{x}) = \frac{1}{Z} \exp[-H(\mathbf{x})/k_B T] \tag{5.7}$$

The probability density ρ is the normalized Boltzmann factor. Now, the problem arises that the exact description in 5.7 contains an overwhelming amount of information ($\mathbf{x}$ stands for a set of N spin degrees of freedom) which is impossible to compute. Thus, an approximation for the exact equation 5.5 is required. The idea of the Monte Carlo simple sampling method is to substitute the exact equation, where one integrates over all states $\{\mathbf{x}\}$ with their proper weights $\rho(\mathbf{x})$, by an integration using only a characteristic subset of phase space points $\{\mathbf{x}_1, \mathbf{x}_2, ..., \mathbf{x}_M\}$ which are used as a statistical sample. In numerical integration routines integrals are replaced by sums. Thus, in the limit $M \to \infty$ the discrete sum

$$\overline{A(\mathbf{x})} = \frac{\sum_{l=1}^{M} \exp[-H(\mathbf{x}_l)/k_B T]\, A(\mathbf{x}_l)}{\sum_{l=1}^{M} \exp[-H(\mathbf{x}_l)/k_B T]} \tag{5.8}$$

approximates 5.5. There are two common routines how to choose the points $\mathbf{x}_l$. In the simple sampling technique the points $\mathbf{x}_l$ are set up with equal probability. Either according to a regular grid or they are chosen randomly. But this procedure has severe disadvantages especially at low temperatures where only few states dominate the sum 5.8 while the main part of the phase space points are irrelevant, cf. Fig. 5.1. In order to cure this problem the method of importance sampling has been introduced in which the points $\mathbf{x}_l$ are chosen with a certain probability $P(\mathbf{x}_l)$. This ensures that only the points

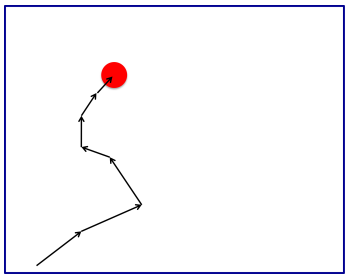

Figure 5.2: The arrows indicate the so called Markov chain eventually reaching the region of phase space where states occur with very high probability (red circle).

which matter are selected. Equation 5.8 then reads:

$$\overline{A^{is}(\mathbf{x})} = \frac{\sum_{l=1}^{M} \exp[-H(\mathbf{x}_l)/k_BT]\, P^{-1}(\mathbf{x}_l)\, A(\mathbf{x}_l)}{\sum_{l=1}^{M} \exp[-H(\mathbf{x}_l)/k_BT]\, P^{-1}(\mathbf{x}_l)}. \tag{5.9}$$

The most natural choice for $P(\mathbf{x}_l)$ would be $P(\mathbf{x}_l) \propto \exp[-H(\mathbf{x}_l)/k_BT]$. Then the Boltzmann factor cancels out and 5.8 reduces to a simple arithmetic average:

$$\overline{A(\mathbf{x})} = \frac{1}{M}\sum_{l=1}^{M} A(\mathbf{x}_l) \tag{5.10}$$

For the construction of the points according to the Boltzmann distribution the so called Markov process is used.

5.1 Markov process

The Metropolis algorithm which will be introduced in the following section is based on the Markov process. Following the Markov process a new state $\mathbf{x}_{l'}$ is constructed from a given state $\mathbf{x}_l$ with respect to a given transition probability $P(\mathbf{x}_l \to \mathbf{x}_{l'})$. Based on a given starting state a chain of states is built, known as Markov chain, finally resulting in the states with Boltzmann distribution $P_{eq}(\mathbf{x}_l) = \frac{1}{Z}\exp[-H(\mathbf{x}_l)/k_BT]$ (cf. Fig. 5.2). A sufficient condition to achieve this is to impose the principle of detailed balance

$$P_{eq}(\mathbf{x}_l)\, W(\mathbf{x}_l \to \mathbf{x}_{l'}) = P_{eq}(\mathbf{x}_{l'})\, W(\mathbf{x}_{l'} \to \mathbf{x}_l). \tag{5.11}$$

Equation 5.11 implies that only the energy change $\delta H = H(\mathbf{x}_{l'}) - H(\mathbf{x}_l)$ defines the ratio of the transition probabilities for a "move" $\mathbf{x}_{l'} \to \mathbf{x}_l$ and the inverse move $\mathbf{x}_l \to \mathbf{x}_{l'}$,

$$\frac{W(\mathbf{x}_l \to \mathbf{x}_{l'})}{W(\mathbf{x}_{l'} \to \mathbf{x}_l)} = \frac{P_{eq}(\mathbf{x}_{l'})}{P_{eq}(\mathbf{x}_{l'})} = \exp(\frac{-\delta H}{k_BT}). \tag{5.12}$$

As Eq. 5.12 is ambiguous, several options for the choice of W exist. One of them is given by the Metropolis algorithm [78, 88].

5.2 Metropolis algorithm

In the Metropolis algorithm the transition probabilities are given as

$$P(\mathbf{x}_l \rightarrow \mathbf{x}_{l'}) = \begin{cases} \exp(\frac{-\delta H}{k_B T}) \, , & \text{if } \delta H > 0 \\ 1 & \text{otherwise.} \end{cases} \tag{5.13}$$

The transition to the new state will be realized in case the new state is lower in energy, if this is not the case the transition will only occur with the probability given by the exponent. The algorithm proceeds as follows: First an appropriate starting state $\mathbf{x}_l$ is set up. Then a new state $\mathbf{x}_{l'}$ is chosen randomly. As a next step the energy difference $\delta H = H(\mathbf{x}_{l'}) - H(\mathbf{x}_l)$ is calculated and the transition is carried out if $\delta H < 0$, i.e. if the energy of the new state is lower than the energy of the old state. Otherwise, the exponent $\varepsilon = \exp(\frac{-\delta H}{k_B T})$ has to be calculated which defines the transition probability. This is implemented in the simulation by choosing randomly a number $0 \leq r \leq 1$. If $r \leq \varepsilon$, the system will adopt the new state, otherwise it remains in the old state and the random selection of a new state is carried out again and the whole proceedure is repeated. One important aspect within this routine is that the new states are not selected by chance, rather only states with little energy difference are chosen. This is of importance because in thermodynamic equilibrium the energy variations are small.

5.3 Determination of T_C

The Monte Carlo simulation provides the magnetization as a function of the temperature. The total magnetization M is propotional to $M \propto (\frac{T - T_C}{T_C})^{\beta}$ with the critical exponent β. In the 3 dimensional Heisenberg model the critical exponent is $\beta = 0.3646$. Plotting $m = M^{1/\beta}$ as a function of the temperature yields a linear decreasing function with increasing temperature. At the intersection of m with the x-axis the Curie temperature is reached. Thus, the Curie temperature can be determined by the linear regression of the function $m = M^{1/\beta}$. As a representative example the total magnetization and the linear regression for the case of Ni_2MnGa at $c/a = 1.25$ is given in Figure 5.3.

5.4 Computational details

The self-consistent calculations at $T = 0$ K of crystalline structure, magnetism as well as the evaluation of force constants were carried out by using the density functional theory method as implemented in the Vienna *Ab-initio* Simulation Package, VASP (http://cms.mpi.univie.ac.at/VASP/), using a plane wave basis set and the projector augmented wave (PAW) method [89, 90]. The solution of the Kohn-

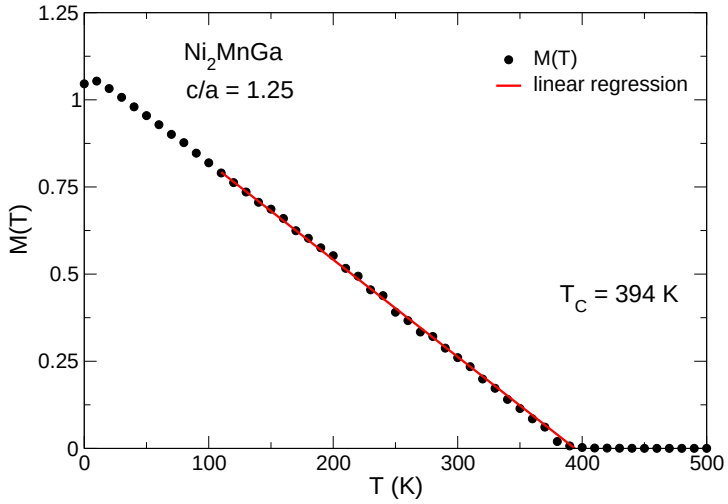

Figure 5.3: Determination of the Curie temperature from linear regression of the function $m = M^{1/\beta}$ for the representative Ni_2MnGa system at $c/a = 1.25$.

Sham equations is obtained using an efficient matrix-diagonalisation scheme (blocked davidson). The exchange-correlation potential is used in the functional form of Perdew, Burke and Ernzerhof (PBE) [84, 91]. The PAW potentials include the following valence electrons: Fe: $3p^6 3d^7 4s^1$, Co: $3d^8 4s^1$, Ni: $3d^9 4s^1$, Ga:$3d^{10} 4s^2 4p^1$ and Zn: $3d^{10} 4s^2$. All plane waves with energies below the cut-off energy of 460 eV are included in the basis set. For the evaluation of the ground state energies the integration over the Brillouin zone was carried out by means of the tetrahedron method (ISMEAR = -5) with Blöchl corrections and a Γ-centered 13^3 grid. The parameter ISMEAR determines how the partial occupancies are set for each orbital corresponding to a finite temperature situation. For the calculation of mixing energies an increased k-point mesh of 19^3 has been used. The electronic self-consistency iteration cycle is aborted when the energy difference between two subsequent energies is less than 10^{-7} eV (EDIFF = 10^{-7} eV).

The calculation of disorder is especially difficult with a plane-wave basis code as VASP in which preferentially small unit cells are used in order to speed up the calculation. If one aims to model ideally disordered structures within this approach large supercells with randomly distributed atoms are required. For substitutional disordered alloys or off-stoichiometric compositions the coherent potential approximation (CPA) can be applied (as done for the magnetic exchange correlation parameters, J_{ij}, discussed later in this section). But when using two different approaches for the evaluation of the total energy the compatibility of the results gets lost. Thus, for monitoring structural disorder (A2) within VASP for the Co_2NiGa and the (NiCo)FeGa systems, a 128 atom supercell calculation with random distribution of the four different elements has been performed. In order to keep the numerical effort for the 128 atom supercell calculation feasible the energy convergence criterium was reduced to 10^{-5} eV. Also the number of k-points was adapted to the large size of the unit cell: a 2^3 k-point mesh was used which corresponds to 8 k-points in the irreducible Brillouin zone. In order to optimize

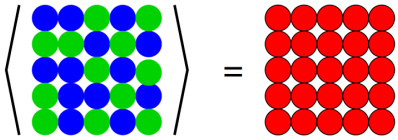

Figure 5.4: Schematic illustration of the substitutionally random alloy on the left and the corresponding effective CPA medium on the right.

the atomic positions, the structures are fully relaxed by means of the conjugent gradient algorithm. For the structural optimization the method of Methfessel and Paxton is well suited (ISMEAR = 1). The relaxation procedure for the large supercells was carried out in three subsequent steps. First, a comparatively crude relaxation step with low precision and a reduced energy cut-off criterion (EDIFF = 10^{-3} eV) was made with the goal to achieve a start charge density for the second relaxation step with higher precision. This first relaxation step is stopped when the energy difference between two subsequent ionic relaxation steps is smaller than $2*10^{-2}$ eV (EDIFFG = $2*10^{-2}$ eV). The second relaxation step then starts from the charge density of the first step which accelerates the total relaxation procedure. This second relaxation is performed with higher precision (EDIFF = 10^{-4} eV) and a very accurate force cut-off criterium: The structural optimization is stopped when the forces are less than 0.02 eV/Å. In order to obtain appropriate converged total energies a final electronic self-consistency run is set up with the tetrahedron method (ISMEAR = -5) and EDIFF = 10^{-7} eV as discussed above. The magnetic exchange interaction parameters, J_{ij}, are determined by using the spin polarized relativistic Korringa-Kohn-Rostoker (SPR-KKR) package, version 3.6 with 250 k-points and 30 energy-points [73, 74]. Thereby, long-range oscillations of the J_{ij} up to 4.5 a_0 are taken into account. For the off-stoichiometric compounds the coherent potential approximation (CPA) can be invoked. In general, the effective CPA medium represents the electronic structure of a configurational averaged substitutionally random alloy A_xB_{1-x} (cf. Fig. 5.4). For the off-stoichiometric and especially Mn-excess Ni_2Mn_{1+x}(Ga, In, Sn, Sb)$_{1-x}$ alloys, the long-range oscillations can cause problems due to appearance of competing ferromagnetic and antiferromagnetic correlations. Here, the number of k-points was enhanced to 500 and the number of energy points to 60. Usually, the *ab initio* J_{ij} are determined using a 4 atom unit cell in which off-stoichiometry is implemented by CPA. From these J_{ij} the Curie temperature is determined by means of Monte Carlo simulations of a classical Heisenberg model using the Metropolis algorithm, cf. section 5. Periodic boundary conditions were used for system sizes up to 24^3 unit cells for a representative case. It turned out that a temperature step of 10 K, 100 Monte Carlo measurements per temperature step, and 10 Monte Carlo sweeps in between two measurements were in most cases enough to obtain sufficiently smooth magnetization curves. But it turns out that sometimes the magnetic structures resulting from the Monte Carlo simulation differ from the assumed spin configuration in the small unit cell used for the SPR-KKR evaluation of the J_{ij}. Hence, the J_{ij} have to be recalculated in a larger unit cell which allows to map the Monte Carlo results

for the spin configuration. With these new J_{ij} the Monte Carlo simulation has to be repeated. This self-consistent cycle has to be preformed until both calculations result in the same spin configuration. But this is a very time-consuming process which has been carried out only for some selected cases, e.g., for Ni_8Mn_7In (cf. chapter 6). On the other hand, this implies that the existence of non-collinear spin configurations cannot be excluded for the disordered non-stoichiometric compounds. This problem can partly be cured by a reducing the cutoff to 3 a_0 for the J_{ij} in real space (thus, neglecting part of the long-range oscillatory exchange interactions).

The phonon dispersion curves were calculated by my colleague Dipl.-Phys. M. Siewert using the PHON code of Dario Alfè which makes use of the so-called direct approach [92], where the force constants needed to construct the dynamical matrix were obtained from supercell calculations using 108 atoms (3^3 primitive cells with 4 atoms). According to the symmetry of the primitive cell, atoms were individually displaced from their ideal positions by 0.02Å and the resulting forces were calculated using a 2^3 Monkhorst grid as k-mesh.

6 Prototype series Ni_2MnZ with Z = Ga, In, Sn, and Sb

6.1 Introduction

Before discussing my results in search of future FSMA it is worthwhile to reconsider the structural and magnetic trends of the prototypical series Ni-Mn-Z (Z = Ga, In, Sn, Sb) which are on the edge of being used in technological applications involving actuator and magnetocaloric devices [58].This is done by reconstructing the experimental phase diagram by means of *ab initio* calculations. In this process, the martensite temperatures have been determined by my colleague M. Siewert while I have calculated the Curie temperatures. The results of the calculations presented in this chapter are partly published in [93, 94] and will serve as a foundation for the later discussion which is devoted to the proposal of new ferromagnetic Heusler alloys. This section also shows the predictive power of *ab initio* calculations when determining phase diagrams over a wide range of compositions of the alloys.

6.2 Results and discussion

In Fig. 6.1 the experimental phase diagram of the $Ni_{50}Mn_{50-x}$(Ga, In, Sn, Sb)$_x$ series is given which shows the dependence of the martensite temperature (T_M) and the critical magnetic temperature in the austenite (T_C^A) and martensite (T_C^M) phases as a function of the composition, i.e. valence electron concentration e/a. The corresponding theoretical phase diagram is given in Fig. 6.2 which shows good agreement with the experimental results. The experimental phase diagram has been adapted from published work [30, 59, 95]. For the off-stoichiometric Ni-Mn-Z alloys the phase diagram has been investigated in detail by several groups [30, 96–100]. e/a is calculated as the concentration-weighted sum of the number of 3d and 4s electrons in Ni and Mn, 4s and 4p in Ga, and 5s and 5p in In, Sn, and Sb. With decreasing temperature, Ni_2MnGa and off-stoichiometric Ni-Mn-Z Heusler alloys transform martensitically to the $L1_0$ tetragonal structure at low-enough Z concentrations or to the modulated structures especially for higher Z concentrations. Ni_2MnGa is the only Heusler system which transforms at the stoichiometric composition. The most common modulated structures are the 5M (10M) and the 7M (14M) modulated structures (cf. Fig. 3.6 in chapter 3.4). The different structural orderings (10M, 14M, $L1_0$) appear in different regions of the phase diagram.

At room temperature the structure evolves from the cubic paramagnetic phase (PM) to the 10M, 14M

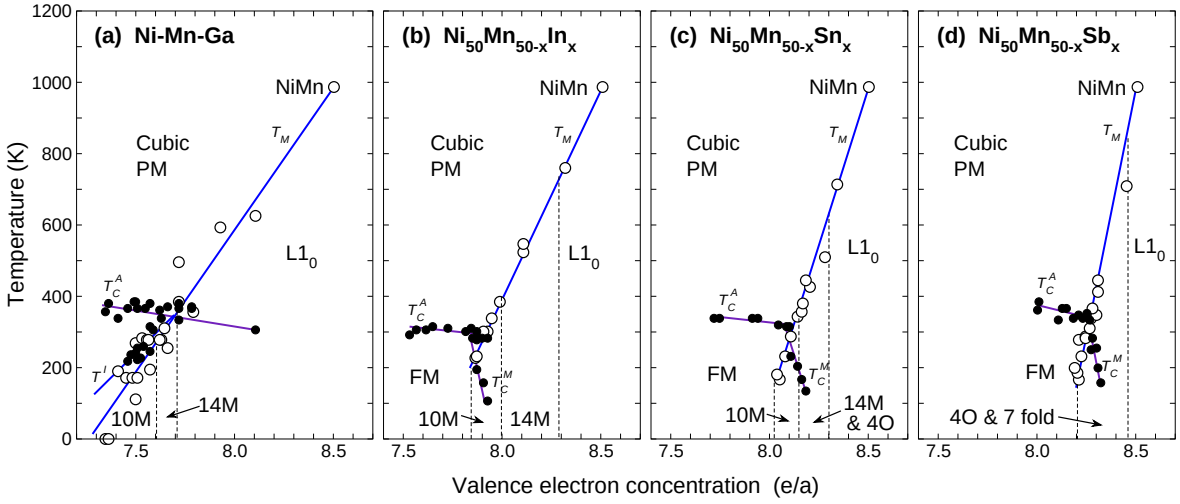

Figure 6.1: The magnetic and structural phase diagram of Ni-Mn-Z Heusler alloys with Z = (a) Ga, (b) In, (c) Sn, and (d) Sb as a function of the valence electron concentration e/a. The filled and open circles correspond to the magnetic and martensitic transformation temperatures respectively. e/a = 7.5 corresponds to Ni_2MnGa and e/a = 8.5 to NiMn. The regions corresponding to the different structures ($L2_1$, 10M, 14M, $L1_0$) are separated by dashed lines. Figure adapted from [30].

and eventually to the $L1_0$ phase with increasing e/a. While the experimental data for Z = In, Sn, and Sb [29, 101–109] refer to alloys with a constant Ni composition of 50%, the results for Ni-Mn-Ga are collected from different sources with varying composition of each of the three elemental constituents which results in the comparatively large scattering of data, cf. Fig. 6.1(a). The slopes of T_M (e/a) are different for different Z-elements. T_M increases rapidly with increasing valence electron concentration. The slope amounts to 80 K per 0.1 e/a for Z = Ga and nearly 270 K per 0.1 e/a for Z = Sb. The variation in e/a of 0.1 corresponds to a compositional variation of about 5 % for Ga and about 2 % for Sb. Thus, it is difficult to prepare samples yielding exactly reproducible T_M which is a further contribution to the large scattering of data, e.g., for Ni-Mn-Ga. The martensitic transformation temperatures in the theoretical phase diagram (cf. Fig. 6.2) are evaluated by my colleague M. Siewert using two different approaches. On the one hand the energy difference between the austenite and the martensite phase, $\Delta E_{c/a}$, as obtained from the total energy calculations is used to estimate T_M and denoted as $T_M(\Delta E)$. On the other hand, the martensite temperature is approximated by using the results from free energy calculations including only the phonon dispersions (not shown here) and marked as $T_M(\Delta F_{ph})$. The values of the two theoretical approximation for T_M slightly deviate from the experimental data points. $T_M(\Delta E)$ is found to yield a lower bound for T_M while $T_M(\Delta F_{ph})$ gives an upper bound as can be seen in Fig. 6.2. Thus, the experimental results are nicely encircled by the theoretical approximations. The rather rough approximations when calculating the martensite temperature presented here can be justified by extending the first-principles calculations to finite temperatures. Including the mag-

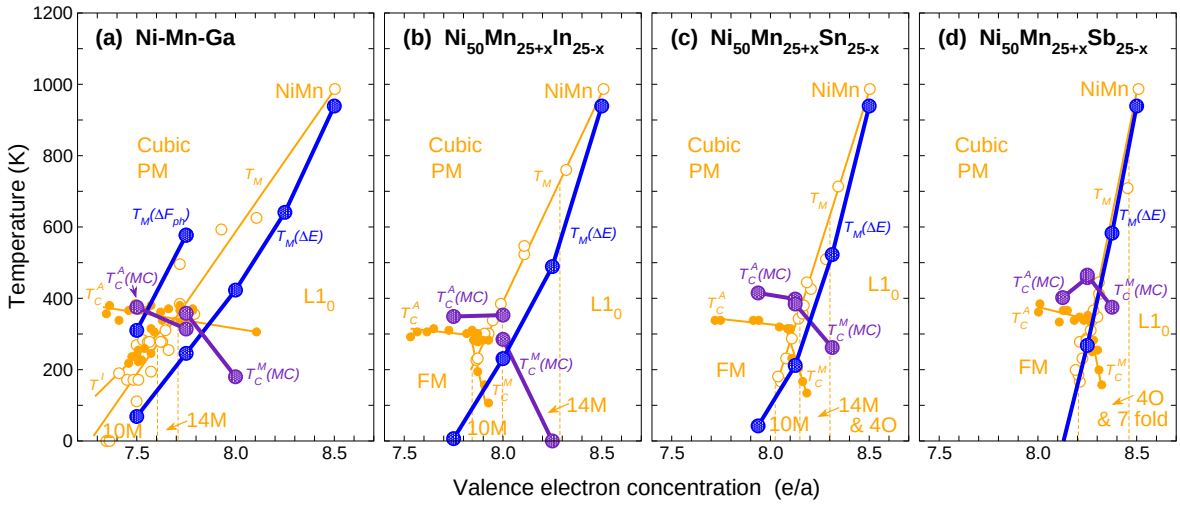

Figure 6.2: The corresponding theoretical phase diagrams of (a) Ni-Mn-Ga, (b) $Ni_{50}Mn_{25+x}In_{25-x}$, (c) $Ni_{50}Mn_{25+x}Sn_{25-x}$, and (d) $Ni_{50}Mn_{25+x}Sb_{25-x}$. T_M as obtained from total energy calculations of $E_{c/a}$ curves is denoted as $T_M(\Delta E)$, and T_M from phonon dispersion is marked as $T_M(\Delta F_{ph})$ (both from Siewert *et al.* [110]). The experimental data points are given in the background (colored in orange). The linear behavior of T_M of the experimental curves is reproduced. While the $\Delta E_{c/a}$ approximation appears at slightly lower temperatures compared to the experimental results, the approximation of T_M obtained by free energy calculations including only the phonon dispersions yields an upper bound. Thus, the experimental results are nicely encircled by the two different theoretical approximations. The critical magnetic temperatures (violet) are both denoted with T_C(MC) and show good agreement with the experimental results. Part (a) and (b) of the figure as published in [94].

netic free energy contribution in addittion to the phonon free energy and electron free energy yields a reliable phase diagram of Ni_2MnGa, as has been recently shown [111]. Remarkable is the linear behavior of T_M although all alloys show a crossover from the ferromagnetic phase at low-temperature to antiferromagnetic order at high temperatures with increasing e/a, finally resulting in an enlarged antiferromagnetic binary NiMn alloy which possesses a high Néel temperature well above 600 K and a high martensite temperature of the order of 10^3 K. The $Ni_2Mn_{1+x}Z_{1-x}$ systems develop antiferromagnetic tendencies already for small Z-concentrations which lead to the decrease of T_M with decreasing e/a. The linearity of the slope is correlated to the dilution of the antiferromagnetically coupled Mn sublattice. In the layered antiferromagnet NiMn a maximum number of antiferromagnetic coupled Mn atoms is observed. Simultaneously, the highest martensite temperature is found. The replacement of Mn with Ga (In, Sn, Sb) dilutes the Mn sublattice and reduces e/a. With decreasing number of Mn atoms with spin-down the antiferromagnetic correlations are reduced and the total magnetic moment increases linearly [94]. This linearity is reflected by the linear behavior of the slope of T_M. Thus, one can tentatively conclude that the antiferromagnetic sublattice of Mn stabilizes the martensitic phase

and that the linearity of the slope of T_M is supported by the linear variation of Mn-atoms with spin-up minus Mn-atoms with spin-down [93]. Compare also the very recent publication of P. Entel *et al.* [94] who discusses the mutual influence of phase transformation, magnetism and electronic properties.
In order to monitor the magnetic trends in the $Ni_2Mn_{1+x}Z_{1-x}$ alloys and to reproduce the experimental Curie temperatures, I first evaluated the magnetic exchange parameters J_{ij} given in Fig. 6.3 and Fig. 6.4. Thereby, the accuracy is rather high with a dense k-point mesh of 500 k-points and 60 energy points for the integration path in the complex plane in the spin polarized relativistic Korringa-Kohn-Rostoker (SPR-KKR) code. A 4 atom unit cell was used (within the coherent potential approximation for the off-stoichiometric alloys), compare chapter 5.4. In Fig. 6.3 the modification of the magnetic exchange coupling constants for the stoichiometric $L2_1$ Ni_2MnZ systems and for the off-stoichiometric $Ni_8Mn_6Z_2$ (Z = Ga, In, Sn, Sb) alloy series is shown. The concentration of the off-stoichiometric systems is chosen in such a way that each of the systems in (e-h) is very close to the martensitic transformation, compare the experimental phase diagram in Fig. 6.1. For the stoichiometric Ni_2MnZ systems the magnitude of the ferromagnetic (FM) Mn-Ni interactions is reduced while simultaneously the FM Mn-Mn coupling grows with increasing e/a (going from Ga, over In and Sn to Sb). For the off-stoichiometric alloys the evaluation of the J_{ij} establishes the observation that the antiferromagnetic (AF) correlations increase with increasing e/a. The ferromagnetic Mn_1-Ni interaction decreases while strong AF interactions evolve between nearest neighbor Mn atoms (denoted as Mn_1 and Mn_2 in Fig. 6.3). Also the deviation from stoichiometric to off-stoichiometric compositions leads to pronounced AF interactions which result from the significant reduction of the nearest neighbor Mn-Mn distance when comparing, e.g., Ni_2MnGa with $Ni_8Mn_6Ga_2$. Thus, one can conclude that antiferromagnetism in disordered Ni-Mn-Z alloys is caused by direct Mn-Mn interactions [93]. However, not only disorder but also tetragonal distortions induce oscillations in the J_{ij} between AF and FM coupling as can be seen in Fig. 6.4. Only for the cubic Ni_2MnGa the coupling is purely FM. For the two tetragonal distortions $c/a < 1$ and $c/a > 1$ AF interactions appear. Reasons for this observation may be slight charge transfer effects and a shortened nearest neighbor Mn-Mn distance in case of $c/a > 1$. The main contribution is the FM Mn-Ni interaction. After the evaluation of the J_{ij} I could set up the Monte Carlo simulations which require the magnetic exchange parameters as input parameters. For all systems apart from Ni_8Mn_7In the use of a 4 atom simulation cell was sufficient. For the Ni_8Mn_7In system I encountered (resulting from the Monte Carlo simulation) a rather complicated spin structure for which the application of the self-consistent cycle as described in chapter 5.4 was required. Here, the Monte Carlo simulations also include long-range oscillations in the J_{ij} up to distances of 4.5 lattice constants and a subsequent 16 atom supercell VASP calculation with the spin structure of the diluted Mn-sublattice as represented in Fig. 6.5 was necessary. In Fig. 6.4 on the right some of the magnetization curves resulting from the Monte Carlo simulations are shown. The corresponding critical magnetic temperatures are given as an inset and reside in the range of 330 - 390 K. These values agree well with experimental results. A summary of the equilibrium parameters and the critical magnetic temperatures is given in Table 6.1. In contrast to the steep slope of T_M, the critical temperature

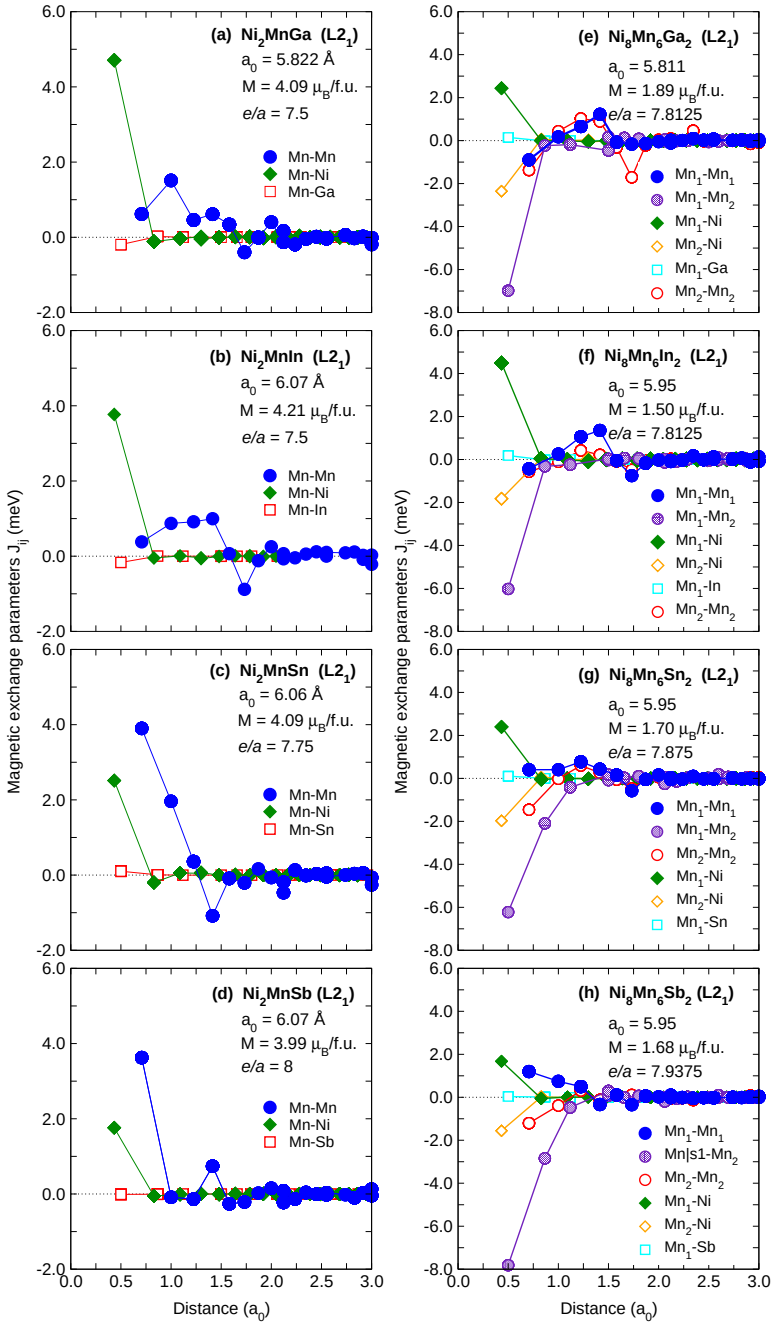

Figure 6.3: Magnetic exchange coupling constants J_{ij} for the stoichiometric Ni_2MnZ on the left (a-d) and for the Ni_8Mn_6(Ga, In, Sn, Sb)$_2$ systems on the right (e-h). The distance is measured from the Mn at the origin in each plot. For the stoichiometric systems the magnitude of the ferromagnetic Mn-Ni interaction decreases while the FM interaction between Mn atoms increases with increasing e/a, i.e. with the sequence Ga–>In–>Sn–>Sb. The off-stoichiometric systems reveal growing antiferromagnetic Mn_1-Mn_2 and a reduction of ferromagnetic Mn_1-Ni interactions with e/a. Mn_1 denotes manganese on the regular Mn-sublattice while Mn_2 has replaced Ga, In, Sn, or Sb. Part (a)-(d) is published in [93]

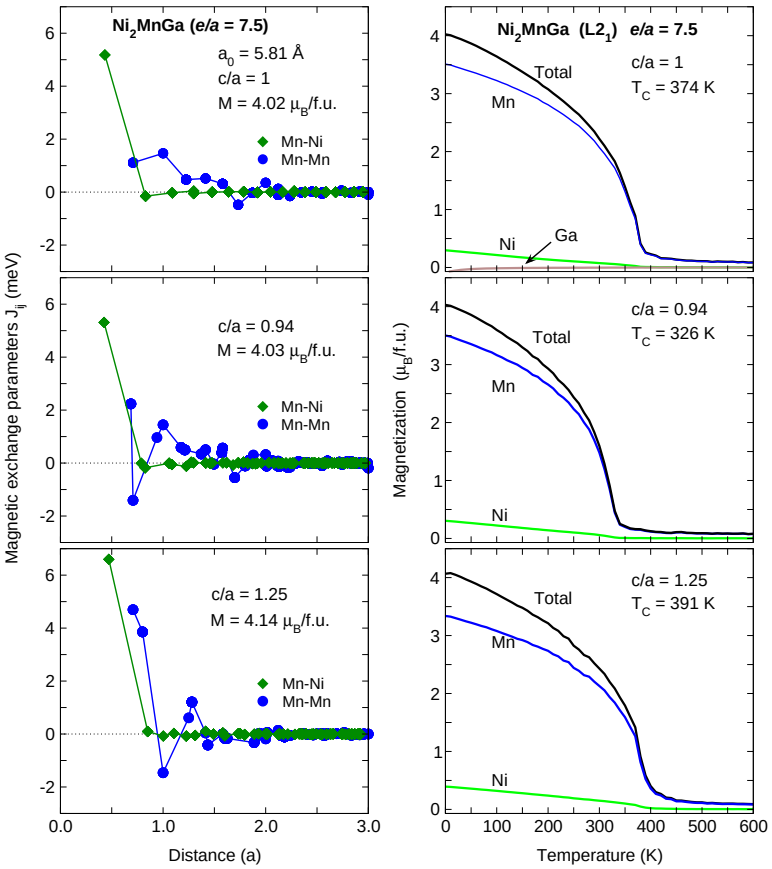

Figure 6.4: Left: Magnetic exchange coupling constants J_{ij} for the stoichiometric Ni_2MnGa at cubic $L2_1$ in the top panel, tetragonal $c/a = 0.94$, and at $c/a = 1.25$ in the lower panels. Right: Corresponding magnetization curves of total and element specific magnetic moments per formula unit. The respective Curie temperatures are also given in the plot. For tetragonal distortions antiferromagnetic interactions occur which reduce T_C for $c/a < 1$. However, for $c/a > 1$ T_C increases owing to an enhancement of the nearest neighbor Mn-Ni and Mn-Mn exchange parameters. Figure taken from [94]

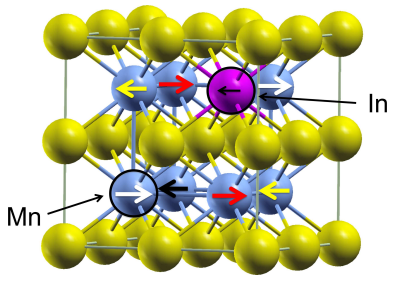

Figure 6.5: The complicated antiferromagnetic spin structure of the Ni_8Mn_7In Heusler unit cell with 8 Ni atoms (yellow spheres), 7 Mn atoms (light blue spheres), and 1 In atom (magenta sphere). The arrows indicate the orientation of the individual spins resulting in a linear ferromagnetic alignment along [111].

Table 6.1: *Ab initio* results for the Ni-Mn-Z systems. Valence electron concentration, e/a, equilibrium lattice parameter a for $c/a = 1$ in Å, c/a-ratio of the austenite and martensite phase, and critical magnetic temperatures for the austenite, T_C^A, and for the martensite phase, T_C^M in K.

System	e/a	$a(c/a=1)$	c/a		T_C^A	T_C^M
Ni_2MnGa	7.5	5.71	1.0	/	375	/
$Ni_8Mn_5Ga_3$	7.75	5.815	1.0	1.3	314	358
$Ni_8Mn_6Ga_2$	8	5.81		1.35	/	180
$Ni_8Mn_5In_3$	7.75	6.0125	1.0	/	349	/
$Ni_8Mn_6In_2$	8	5.95	1.0	0.95	353	285
Ni_8Mn_7In	8.25	6.07	/	0.91	/	0
$Ni_8Mn_5Sn_3$	7.9375	6.01	1.0	/	415	/
$Ni_8Mn_6Sn_2$	8.125	5.95	1.0	0.94	398	384
Ni_8Mn_7Sn	8.3125	5.885	/	0.91	/	262
$Ni_8Mn_5Sb_3$	8.125	5.815	1.0	/	402	/
$Ni_8Mn_6Sb_2$	8.25	5.81	1.0	1.30	458	465
Ni_8Mn_7Sb	8.375	5.71	/	0.91	/	375

of the austenite phase, T_C^A, varies only slowly independent of the Z-element. However, T_C^M shows a steep decrease with increasing e/a. In the austenite phase the ferromagnetic coupling is strong which explains that the critical temperatures, T_C^A, do not vary rapidly with e/a. In the martensitic phase the steep decrease of T_C^M with e/a is caused by the increased number of nearest neighbors Mn atoms with antiferromagnetic correlations which become very strong at the magnetostructural transition. In the Ni-Mn-(In, Sn, Sb) systems this leads to an unusual run of the magnetization curve. As an example, the $M(T)$ curve of the $Ni_{50}Mn_{32}Sb_{18}$ alloy is compared to the $M(T)$ curve of the $Ni_{50}Mn_{35}Sb_{15}$ system in Fig. 6.6. The abrupt decrease of the magnetization for $Ni_{50}Mn_{35}Sb_{15}$ indicates the onset of the martensitic transformation. For the In- and Sn-based alloys similar magnetization curves are found. With respect to the magnetic transition the experimental results are nicely reproduced by my theoretical calculations. For Ni-Mn-Ga an excellent agreement is found. For the Ni-Mn-In, -Sn, and -Sb systems a slight overestimation of the experimental T_C is observed. For the Sb-based system a deviation from the linear character of T_C is found. The deviation may be caused by the competition of different magnetic structures, especially in the case of Ni-Mn-Sb [108, 112]. As mentioned above, these complicated and perhaps non-collinear structures are demanding to map exactly within a restricted size of the unit cell.

6.3 Conclusion

In this chapter the power of the theoretical tools for the prediction of martensite and magnetic transition temperatures by means of *ab initio* calculations and Monte Carlo simulations based on *ab initio* results could be emphasized. The experimental temperature versus composition phase diagrams of the

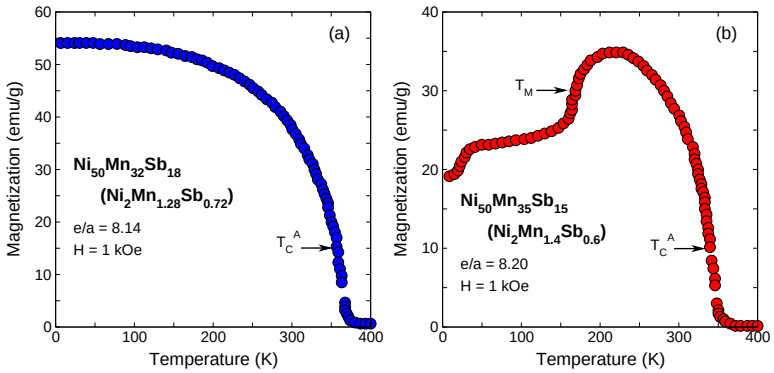

Figure 6.6: Experimental magnetization curves for (a) $Ni_{50}Mn_{32}Sb_{18}$ and (b) $Ni_{50}Mn_{35}Sb_{15}$ in an applied field of 1T. The abrupt reduction of the magnetization at T_M in (b) compared to (a) results from the strong short-range antiferromagnetic correlations when entering the martensitic phase. Similar $M(T)$ curves are found for the In- and Sn-based systems. Figure as published in [108].

prototypical Ni-Mn-(Ga, In, Sn, Sb) alloy series compare well with our theoretical approximations. In the prototype FSMA series Ni-Mn-(Ga, In, Sn, Sb) the martensitic transition temperature crucially depends on the valence electron concentration e/a and can be enhanced when Ga is replaced with Mn, however, under the introduction of disadvantageously antiferromagnetic tendencies. The two different theoretical approximations of the martensite temperature obtained by total energy calculations or by using free energy calculations including only the phonon dispersions nicely encircle the experimental results. The critical magnetic temperatures can be determined with high accuracy and agree well with the experiment. The evaluated magnetic exchange parameters for the stoichiometric systems show that the ferromagnetic Mn-Ni interaction decreases while the antiferromagnetic Mn-Mn interaction increases going from Ga to In, Sn, and Sb. The J_{ij} of the off-stoichiometric or tetragonally distorted systems reveal the development of strong antiferromagnetic nearest neighbor Mn-Mn couplings with increasing e/a which originate from a significant reduction of the nearest neighbor Mn-Mn distances. Therefore, one can conclude that direct Mn-Mn interactions cause antiferromagnetism in disordered Ni-Mn-Z alloys with Z = Ga, In, Sn, and Sb.

7 Martensitic $Ni_2CoGa(Zn)$ and $Co_2NiGa(Zn)$

7.1 Introduction

In the previous chapter strong antiferromagnetic interactions was encountered between nearest neighbor Mn atoms in the prototypical series Ni-Mn-(Ga, In, Sn, Sb). For FSMA these antiferromagnetic correlations are not desirable as they hinder the increase of both, T_M and T_C, simultaneously. They are also not favorable for a large magnetocristalline anisotropy energy. The addition of a fourth element (Ga) to the Ni-Mn-In alloy had led to an increase of T_M [113] but it was not possible so far to push the operation temperatures from 100 or 200 K to temperatures well above room temperature. Thereby, I have anticipated that ferromagnetic Co with its large magnetic moment is a reasonable candidate to replace Mn. A martensitic transformation has in fact been observed experimentally for off-stoichiometric $Co_{48}Ni_{22}Ga_{30}$ ($e/a = 7.42$) [33, 114] which provoked my systematic investigation of a series of corresponding stoichiometric Co-Ni-based alloys with similar composition and valence electron concentrations: Co_2NiZn ($e/a = 7.5$), Ni_2CoZn ($e/a = 7.75$), and Ni_2CoGa ($e/a = 8$). Apart from very few investigations concerning Ni_2CoGa [22, 115, 116] only little is known about these alloys. The Co-Ni-Ga system has also been investigated by my colleague M. Siewert *et al.* [48].Therefore, I here only present my most important results for this system. Material combinations including the element Zn has not been considered very often up to now because of the high vapor pressure of Zn. But Zn is known to be beneficial for alloying in ternary, non-magnetic Cu- or Ni-based shape memory alloys like Cu-Zn-Al [117, 118]. In my study Zn, occupies the Z-site and thus substitutes Sn, Al, or Ga in the regular X_2YZ Heusler compounds. I here discuss the results of my first-principles investigation of the ferromagnetic and nonmagnetic Ni_2CoGa and Ni_2CoZn systems, and the ferromagnetic Co_2NiGa and Co_2NiZn alloys in the conventional X_2YZ and the inverse (XY)XZ Heusler structure. The results for the $Ni_2CoGa(Zn)$ systems are published in [24].

7.2 Results and discussion

7.2.1 Ni_2CoGa and Ni_2CoZn

I have performed total energy calculations for the determination of the groundstate of the alloys under consideration. All alloys show a ferromagnetic equilibrium state, cf. Fig. 7.1. The volume of the cubic phase does not change significantly when approaching the lower energy state for the tetragonally distorted case with $c/a > 1$. Thus, the calculation of the total energy with respect to tetragonal distor-

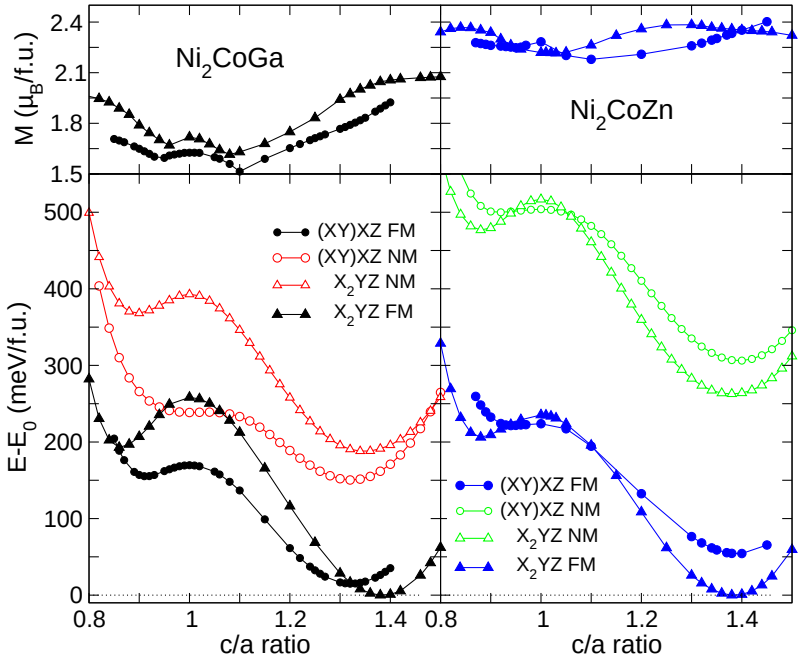

Figure 7.1: Variation of the total energy with respect to the absolute energy minimum and variation of the total magnetic moment M under an isochoric tetragonal distortion c/a for Ni_2CoGa on the left and Ni_2CoZn on the right. Circles denote the conventional and triangles the inverse Heusler structure. Filled symbols mark the ferromagnetic (FM) and open symbols the nonmagnetic (NM) case. The ferromagnetic phase is energetically preferred. The occurrence of two energy minima reveals the tendency of the system to undergo a martensitic transition.

tion ($c/a \neq 1$) is performed under maintenance of the groundstate equilibrium volume for the cubic case. I have calculated the binding curves for the non-magnetic and the ferromagnetic cases (the latter has lower energy in each case). I found two energy minima, one at a $c/a \leq 1$ and the other at $c/a > 1$. This indicates the tendency of each system for a martensitic instability. The tetragonally distorted structures with $c/a > 1$ are clearly energetically favored for both structural and magnetic ordering types. The energy difference between the cubic phase and the absolute energy minimum at $c/a > 1$, $\Delta E_{c/a}$, is for both alloys and both ordering types 4-9 times larger than in Ni_2MnGa (6 meV/atom) [119] and thus suggests higher martensite temperatures, cf. Table 7.1. On the other hand such large energy differences require a too large activation energy to induce the martensitic transformation. For ferromagnetic Ni_2CoGa the conventional and the inverse Heusler structures are very close in energy in the vicinity of the tetragonally distorted absolute energy minimum ($c/a \simeq 1.35$). Here, the (XY)XZ structure is only 16 meV/f.u. (4 meV/atom) higher in energy. In the cubic case the hierarchy of the two ordering types has even reversed. This shows the competition of the inverse and the conventional Heusler structures and may even imply that a disordered alloy is stabilized during the experimental production process of the sample depending on the rate of the cooling procedure. The energy differ-

Table 7.1: Calculated equilibrium parameters of the tetragonally distorted ferro- (FM) and nonmagnetic (NM) Ni-Co-Ga(Zn) systems in the conventional X_2YZ and in the inverse (XY)XZ Heusler structure (see Fig. 3.5): Equilibrium lattice constant a_0 in (Å) for the cubic $(c/a = 1)$ phase, tetragonal distortion c/a of the absolute energy minimum, total magnetic moment M per formula unit in μ_B/f.u. and mixing energy E_{mix} at the absolute energy minimum ($c/a > 1$), and Curie temperature T_C in K of the $c/a > 1$ phases, energy difference between the cubic phase at $c/a = 1$ and the absolute energy minimum at $c/a > 1$, $\Delta E_{c/a}$, energy difference between the conventional X_2YZ and inverse (XY)XZ ordered structure, ΔE_{order}, and the energy difference between the absolute energy minima of the ferro- and the nonmagnetic phase, ΔE_{FM-NM}. All energies in meV/atom. The calculation shows that the equilibrium volume of the cubic phase, $V_0 = a_0^3$, does practically not change when the system undergoes a tetragonal distortion $(c/a \neq 1)$, i.e. $a^2c \simeq a_0^3$.

	Ni_2CoGa $(e/a = 8)$				Ni_2CoZn $(e/a = 7.75)$			
	FM		NM		FM		NM	
	X_2YZ	(XY)XZ	X_2YZ	(XY)XZ	X_2YZ	(XY)XZ	X_2YZ	(XY)XZ
a	5.720	5.704	5.691	5.684	5.710	5.703	5.680	5.677
c/a	1.38	1.32	1.34	1.32	1.38	1.4	1.38	1.4
M	2.05	1.81			2.37	2.37		
E_{mix}	-825	-810	-636	-673	-212	-157	50	90
T_C	213	175			273	312		
$\Delta E_{c/a}$	66	39	51	22	59	42	64	48
ΔE_{order}	-4		9		-14		-11	
ΔE_{FM-NM}	-47				-65			

ence between the ferro- and the nonmagnetic phase gives a first information about the stability of the ferromagnetic solution which is of interest for this study. The nonmagnetic solutions of the Ni-Co-Ga system lie about 47 meV/atom higher in energy at $c/a \simeq 1.4$ but at $c/a = 1$ the binding curves of the ferromagnetic X_2YZ and the nonmagnetic (XY)XZ structures overlap.

The variation of the total magnetic moment with tetragonal distortion reveals comparatively low changes of the magnetization. At the groundstate X_2YZ structure at $c/a = 1.38$ the total moment amounts to $M = 2.05\ \mu_B$ which is clearly smaller than $M = 3.84\ \mu_B$ found for $L1_0$ Ni_2MnGa.

For Ni_2CoZn qualitatively similar results are found. The tetragonally distorted ferromagnetic X_2YZ structure at $c/a = 1.38$ is the groundstate. Here, the inverse Heusler structure lies about 9 meV/atom higher in energy compared to the conventional structure. At $c/a = 1$ the two different ordering types are energetically almost degenerate which indicates an even more pronounced competition of the two different structural orderings. The nonmagnetic solution lies about 300 meV/f.u. higher in energy and is energetically unfavorable. This finding hints towards a stabilization of the ferromagnetic phase when Ga is replaced by Zn.

The total magnetic moments of the Zn-based compound are enhanced by approximately 15% compared to the Ga-based alloy, cf. Table 7.1, which goes hand in hand with the enlarged energy differ-

ence between the nonmagnetic and the ferromagnetic solution as is obvious from the binding energy curves. At the equilibrium phase of the X_2YZ structure at $c/a = 1.38$ the total moment amounts to $M = 2.37\ \mu_B$ and the variation of the magnetic moments under tetragonal distortion is less pronounced as for the Ga-based alloy.

The mixing energies reveal that, with exception of nonmagnetic Ni_2CoZn, all alloys are stable with respect to decomposition into their elemental constituents, cf. Table 7.1. A general trend can be formulated: the mixing energies are lowest for the Ga-based compounds in the ferromagnetic conventional Heusler structure and increase for the ferromagnetic inverse Heusler structure. The even higher mixing energies of the corresponding nonmagnetic Ga-based solutions emphasize their reduced stability. The replacement of Ga by Zn leads to higher mixing energies which approach zero or are even positive values for the nonmagnetic Ni-Co-Zn compounds implying that these alloys are not stable.

In order to gain information about the applicability of the alloys for ferromagnetic shape memory purposes, the exchange coupling constants are calculated (not shown here) and afterwards inserted into the Monte Carlo routine for the evaluation of the Curie temperatures. The Curie temperatures are below room temperature: T_C = 213 K for Ni_2CoGa and T_C = 273 K for Ni_2CoZn. The substitution of Ga by Zn leads to an enhancement of T_C which is consistent with the enlarged energy difference between ferro- and non- magnetic phases ($\Delta E_{\mathrm{FM-NM}}$) in Ni-Co-Zn compared to Ni-Co-Ga. The origin of the beneficial influence of Zn on the magnetic properties will be discussed in Section 8.3.1.4.

In summary, the alloy systems $Ni_2Mn(Ga,Zn)$ may not be adequate materials for magnetic shape memory devices because martensitic transformation will occur in the paramagnetic phase since T_M^S estimated from the $\Delta E_{\mathrm{c/a}}$ will be higher than T_C.

7.2.2 Co_2NiGa and Co_2NiZn

In the preceding section I found that the Curie temperatures of the Ni-rich Ni-Co-based systems are below room temperature which significantly confines their applicability for future FSMA. As Co provides a higher magnetic moment than Ni I considered instead of Ni-rich Ni-Co-systems now Co-rich Co-Ni-systems in order to guarantee higher Curie temperatures. The Co-Ni-Ga system is one of the rather novel materials which has been suggested first by M. Wuttig [37] as promising candidate for future FSMAs. Very recently, its structural, electronic, magnetic and dynamical properties have been investigated by M. Siewert *et al.* [48] and also by Garay *et al.* both using a combined experimental and theoretical approach. In addition to a higher Curie temperature also a better ductility can be expected owing to the introduction of a small amount of a secondary γ-phase [35, 120]. For the composition $Co_{48}Ni_{22}Ga_{30}$ a martensite start temperature T_M = 284 K was observed in experiment. In analogy to the approach used in the section above for the characterization of Ni_2CoGa and Ni_2CoZn, I have also investigated the corresponding Co_2NiGa and Co_2NiZn Heusler alloys. As the mixing energies turn out to be positive for the Zn-based alloy the main attention is focussed on to Co-Ni-Ga while the most important results for Co-Ni-Zn are summarized for comparison only.

In Fig. 7.2 the total energy curves as a function of tetragonal distortion are shown. The inverse Heusler

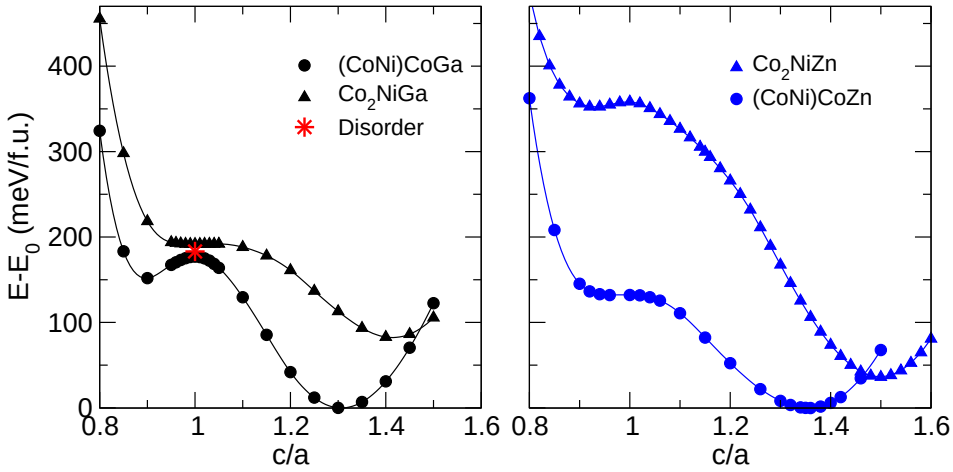

Figure 7.2: Variation of the total energy with respect to the absolute energy minimum under the isochoric tetragonal distortion c/a for the ordered conventional Co_2NiGa (triangles) and inverse (CoNi)CoGa Heusler compound (circles) [48] on the left and the corresponding Zn-based compounds on the right. For the Ga-based system the inverse and conventional Heusler structure are energetically nearly degenerated at $c/a = 1$ which shows competing structural ordering tendencies. This is underlined by the simulation of a completely disordered structure (red star) which is found to lie in the same energy range. In contrast, for the Zn-based systems the inverse and the conventional Heusler structure are energetically clearly separated.

Table 7.2: Calculated results of ferromagnetic Co-Ni-Ga(Zn) in the conventional and the inverse Heusler structure. Parameter labeling as in Table 7.1. For the novel FSMA Co-Ni-Ga a completely disordered bcc structure (A2) has been calculated for comparison (Disorder). Disorder, conventional and inverse order are energetically almost degenerated indicating that a mixture of different ordering mechanisms or complete disorder has to be expected at finite temperatures which is in agreement with experimental findings [121].

	Co_2NiGa ($e/a = 7.75$)			Co_2NiZn ($e/a = 7.5$)	
	X_2YZ	(XY)XZ	Disorder	X_2YZ	(XY)XZ
a	5.695	5.710	5.735	5.688	5.706
c/a	1.41	1.31	1.0	1.5	1.35
M	2.95	2.76	3.09	3.56	3.42
E_{mix}	-569	-650	/	30	0
T_C	377	452	/	556	574
$\Delta E_{c/a}$	27	44	/	81	33
ΔE_{order}	21			9	

structure is the lower energy phase for large tetragonal distortions around $c/a = 1.3$ for the Ga- as well as the Zn-based system. However, at $c/a = 1$ the conventional and the inverse Heusler structure are energetically almost degenerated for the Co-Ni-Ga alloy which points to a coexistence of different

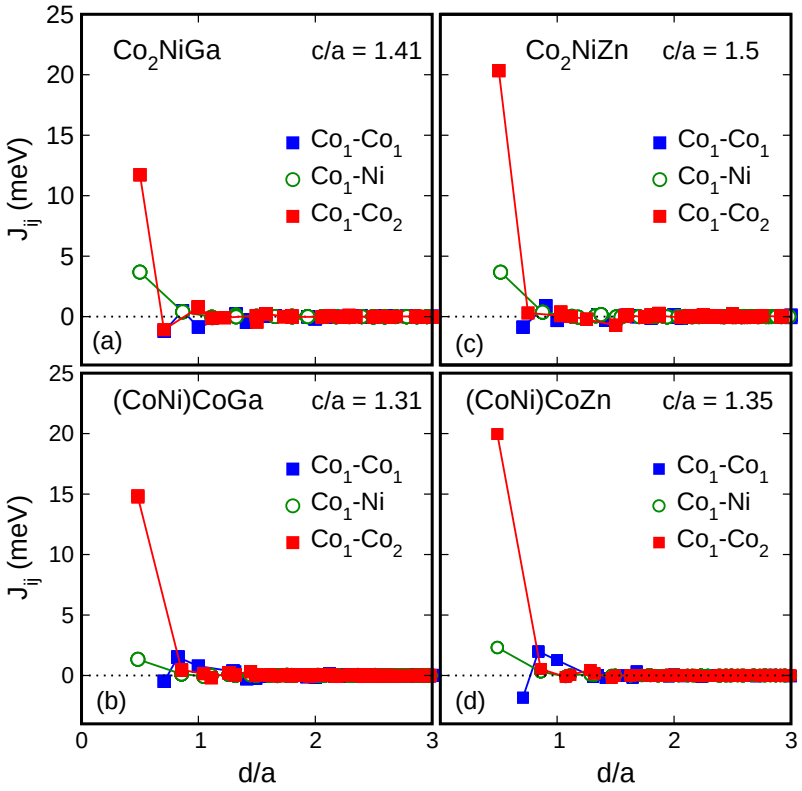

Figure 7.3: Magnetic exchange coupling constants, J_{ij}, of conventional and inverse Co-Ni-Ga Heusler alloys on the left and Co-Ni-Zn on the right as a function of the distance d in units of the lattice constant a of the tetragonal phase (a is determined by $V_0 = a_0^3 = a^2c$, a_0 = lattice constant of the cubic structure). The distance is given with respect to the first atom (which is at the origin) in the figure legend. (a) Conventional Co_2NiGa at $c/a = 1.41$, (b) inverse (CoNi)CoGa at $c/a = 1.31$, (c) Co_2NiZn at $c/a = 1.5$, and (d) (CoNi)CoZn at $c/a = 1.35$. Blue squares denote the Co_1-Co_1 coupling, green open circles belong to the Co_1-Ni coupling, and red squares mark the Co_1-Co_2 interaction.

structural orderings at finite temperatures. This would be in line with experimental findings which report a disordered B2 structure [38]. The B2 structure consists of two interpenetrating cubic sublattices with random distribution of Ni and Ga on the one sublattice and complete Co occupation on the other. In order to verify the assumption of a disordered phase a random substitutional Co-Ni-Ga alloy has been modeled in a large supercell with random occupation of 128 atoms (64 Co, 32 Ni, and 32 Ga atoms) on the crystal lattice. The simulation is computationally rather expensive and time consuming. In principle, a 100% correct simulation of a completely disordered phase would require to invoke the concept of special quasirandom structures (SQS's). which was proposed by Zunger *et al.* [122–124] in order avoid the high computational cost associated with the construction of the large supercells with random occupancy of atoms. SQS's are small-unit-cell periodic structures which contain only a few (2-16) atoms per unit cell. They mimic the most important, near-neighbor pair and multisite cor-

relation functions of the random substitutional alloys. For a perfectly random alloy no correlation in the occupation between various sites exists. It is possible to construct SQS's which exactly reproduce the correlation functions of the corresponding random alloy but this is beyond the scope of this thesis. For the case of the Co-Ni-Ga system, I have restricted myself to one 128 atom supercell calculation for which I carefully checked the distribution of the atoms in order to exclude local ordering. To minimize the numerical effort, the total energy of the relaxed structure has only been determined at $c/a = 1$. And indeed, the first-principles calculations emphasize the initial guess of competing inverse and conventional Heusler structure because the disordered alloy lies in the same energy range as the ordered structures (2 meV/atom lower than the conventional Heusler structure). The binding curve of a disordered structure can thus be seen as a superposition of the ordered structures which both show a martensitic instability. (CoNi)CoGa has a local energy maximum for the cubic structure while the corresponding conventional Co_2NiGa structure develops an energy saddle point at $c/a = 1$. The energy difference between the cubic phase and the absolute energy minima amounts to $\Delta E_{c/a}$ = 28 meV/atom for the X_2YZ and $\Delta E_{c/a}$ = 44 meV/atom for the (XY)XZ structure, see Table 7.2. For the stoichiometric Ni_2MnGa system I find $\Delta E_{c/a}$ = 6 meV/atom and $T_M \simeq 200$ K. As $\Delta E_{c/a}$ is propotional to the martensite temperature one should expect an enhancement of T_M for the Co-Ni-Ga system. This is in agreement with the experimental value of T_M = 284 K.

For the Zn-based alloys a clear preference of the inverse structure is observed over the whole c/a range, cf. Fig. 7.2. The conventional Co_2NiZn alloy shows an extraordinarily large tetragonal distortion, $c/a = 1.5$. While the energy difference between the local and the absolute minimum does not change significantly when comparing (CoNi)CoZn with (CoNi)CoGa, $\Delta E_{c/a}$ is considerably enlarged ($\Delta E_{c/a}$ = 79 meV/atom) for the conventional Co_2NiZn alloy. This indicates that the activation energy needed for the martensitic transformation may be too large. The mixing energy of the Zn-based alloys is zero or has a positive value which implies that these alloys are not stable against decomposition and segregation tendencies. A result which has already been observed for the Ni_2CoZn systems emphasizing the destabilizing effect of Zn.

As already found for the NiCoGa(Zn) systems, the total magnetic moments increase when Ga is substituted by Zn (cf. Tab. 7.2). The beneficial impact of Zn on the magnetic properties is also reflected in the calculated magnetic exchange coupling constants, J_{ij}, see Fig. 7.3. All Co-Ni-Ga(Zn) alloys show ferromagnetic coupling mainly between Co_1 and Co_2 atoms. This interaction significantly increases for the Co-Ni-Zn systems which yields an enhancement of the Curie temperatures from T_C = 452 K for (CoNi)CoGa to T_C = 574 K for (CoNi)CoZn, cf. Tab. 7.2.

7.3 Conclusion

To summarize, Ni_2CoGa and Ni_2CoZn have martensitic energy profiles but the T_C's are below room temperature. Thus, they are at least in case of stoichiometric composition not perfectly suited for future FSMA's. In order to enhance the Curie temperature addition of Fe might be beneficial and a

quaternary Ni-Co-Fe-Ga(Zn) alloy might result in a promising new FSMA. This will be discussed in chapter 9. The Co-rich systems provide Curie temperatures slightly above room temperature. For the Co-Ni-Ga system which has already been proposed as new FSMA by Wuttig *et al.*, a competition between inverse and conventional Heusler structure is found indicating an inherently disordered phase. This could be established by the calculation of a completely disordered phase by means of a 128 atom supercell simulation with random distribution of the atoms on the crystal lattice. The *ab initio* calculations of the Co-Ni-Ga system are in good agreement with experimental findings which report a B2 phase. The energy difference between the austenite and martensite phases, $\Delta E_{\mathrm{c/a}}$, is considerably larger compared to the prototype FSMA Ni_2MnGa which hints towards a higher martensitic transformation temperature. This is in good agreement with experiments which find T_M = 284 K. The results for the Co-Ni-Zn systems establishes the beneficial impact of Zn on the magnetic properties as already found for the Ni-Co-Ga(Zn) alloys of the previous chapter. However, also the mixing energy increases when replacing Ga by Zn which reduces the miscibility of the compound. This suggest that the addition of small amounts of Zn to Co-Ni-Ga could enhance the Curie temperature of this rather novel FSMA which would significantly improve its applicability for future smart material technologies. If by further alloying T_M can be forced to lie below T_C^A, these alloys will be suited for magnetic shape-memory applications.

8 Fe-Co-Ga-Zn with high Curie temperatures

8.1 Introduction

In order to avoid low Curie temperatures as observed for the Ni-Co-Ga(Zn) alloys (discussed in the previous section), Ni is replaced by ferromagnetic Fe and the ternary $Fe_2CoGa(Zn)$ systems as well as the quaternary $Fe_2CoGa_{1-x}Zn_x$ systems are investigated. FeZn alloys with a Zn concentration of 20 - 40% are highly magnetostrictive materials [67] showing a huge magnetostriction similar to Fe_3Ga [61]. In Fe-Co-Zn, the magnetic phase transition induces various interesting anomalies: The equilibrium between the bcc and fcc phases in the Fe-Co-Zn system exhibits an unusual feature, and a miscibility gap between the ferromagnetic and the paramagnetic bcc α-phase [65] occurs, see the ternary isothermal high temperature phase diagram in Fig. 8.1. Early Mössbauer studies of Co_2FeGa and Fe_2CoGa revealed atomic-site preferences showing that Co_2FeGa has a well ordered, conventional Heusler structure ($L2_1$), while in Fe_2CoGa the Co atoms occupy one of the two fcc Fe-sublattices [125] leading to the so called inverse (FeCo)FeGa Heusler structure which confirms the structural ordering trend that transition metal atoms to the left of Fe prefer to occupy the Y-site while those on the right of Fe preferentially go to the X-sublattice [125]. One of the goals of the subsection 8.3 of this chapter will be to find the origin for the strong preference of the inverse Heusler phase for the Fe-rich

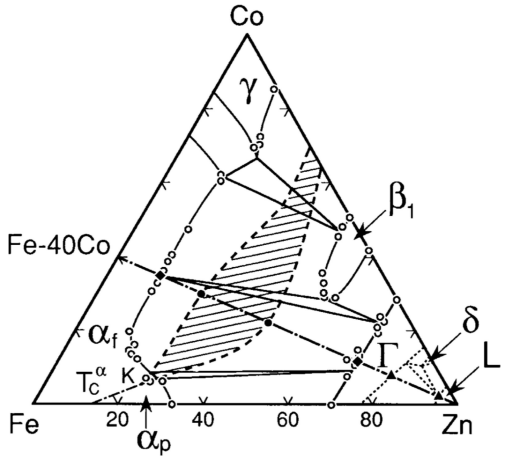

Figure 8.1: Isothermal section of the Fe-Co-Zn phase diagram at 700 °C. Open circles indicate the experimental results.The miscibility gap between the ferromagnetic bcc phase α_f and the paramagnetic bcc phase α_p is indicated by hatching. Figure adapted from [65].

Fe-Co-based systems. Also the corresponding conventional and inverse $Co_2FeGa(Zn)$ compounds are calculated in order to confirm the predicted preferential occupation of Co on the X-sublattice. The half-metallic Heusler compound Co_2FeGa has been investigated, amongst others, by Bushow *et al.* [126]. They establish the $L2_1$ structure already found by Jaggi *et al.* and find a lattice parameter of a = 5.737 Å. The total magnetic moment was reported to be 5.13 μ_B at 5 K. The Curie temperature has been experimentally determined by Umetsu *et al.* to be T_C = 1093 K [127]. Recently, also a detailed study on Co_2FeGa nanoparticles has been published [128].
In section 8.3 results of a systematic investigation of the influence of Zn on the physical properties of quaternary $Fe_2CoGa_{1-x}Zn_x$ are presented.

8.2 Fe-Co-Ga(Zn) and Co-Fe-Ga(Zn)

8.2.1 Results and discussion

An overview of the calculated equilibrium parameters, e.g., the valence-electron concentration e/a, the structurally stable phase, the lattice constant a_0, the energy minima, magnetic moments M, and Curie temperature T_C, are given for the Co-Fe-Ga(Zn) compounds in Table 8.1 in this section and for the Fe-Co-Ga(Zn) alloys in Table 8.2 in the next section 8.3. The investigations of the Fe-Co-Ga-Zn alloys have been published in [23]. For the $Fe_2CoGa(Zn)$ compounds the conventional Heusler structure is martensitic in contrast to the inverse Heusler structure, see Fig. 8.2. The energy difference between austenite and martensite phases is $\Delta E_{c/a} = 56$ meV/atom (cf. Table 8.2 and Table 8.2 in the next section) for Fe_2CoGa, which is almost four times larger than the energy difference of the prototypical compound Ni_2MnGa where $\Delta E_{c/a} \simeq 6$ meV/atom is found. Therefore, one may tentatively associate a higher martensitic transformation temperature with the ternary compounds Fe_2CoGa and Fe_2CoZn ($\Delta E_{c/a} = 48$ meV/atom). But at $c/a = 1$ the energetically preferred phase is the inverse Heusler structure which is not martensitic, in consistency with the experimental findings of Jaggi *et al.* The compound Fe_2CoZn has one valence electron less than Fe_2CoGa. Interestingly, for Fe_2CoZn, the hierarchy of the two ordering types (conventional and inverse) is reversed (cf. Fig. 8.2 and Fig. 8.7). The tetragonally distorted the conventional Heusler structure (at $c/a = 1.40$) is now lowest in energy. However, for the cubic phase ($c/a = 1$) the inverse Heusler structure is still energetically preferred as for Fe-Co-Ga. Due to the competition in the energetics of the structures and due to the fact that during the experimental preparation procedure the specimens are cooled down from a disordered, cubic bcc structure (A2), it is not clear which of these two structures will evolve or whether eventually a completely disordered alloy may result. Also decomposition into a mixture of conventional and inverse structures is conceivable and the resulting energy landscape may still bear signatures of martensitic instabilities. This is especially interesting in the case of Fe_2CoZn, for which the absolute energy minimum at $c/a = 1$ of the inverse Heusler structure lies only 9 meV/atom (36 meV/f.u) higher in energy than the absolute energy minimum of the conventional Heusler structure at $c/a = 1.40$. This energy is of the order of $\Delta E_{c/a} = 6$ meV/atom of prototypical Ni_2MnGa. Therefore, any compositional changes

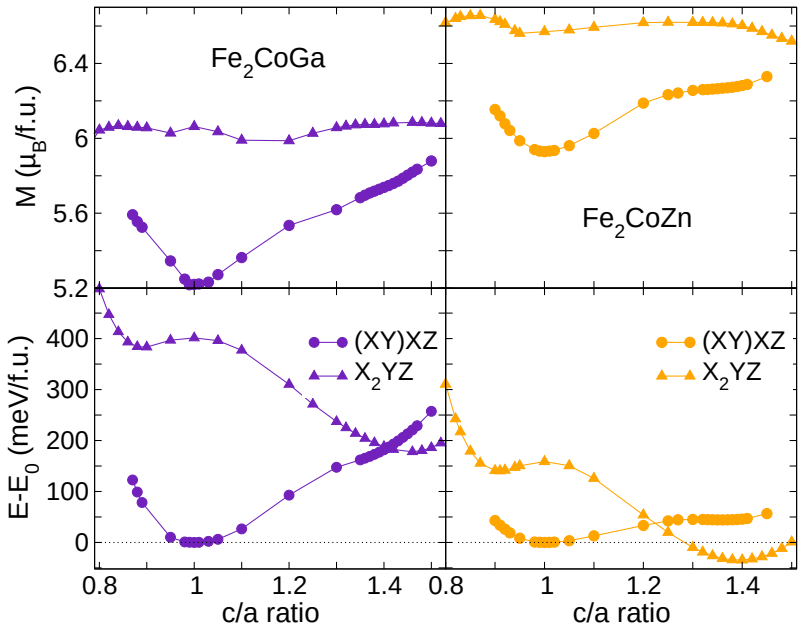

Figure 8.2: Variation of the total energy as a function of the tetragonal distortion c/a and the corresponding magnetic moments M (in μ_B/f.u.) for Co-Fe-Ga (left) and Co-Fe-Zn (right). Circles mark ordering type (XY)XZ while triangles mark the conventional Heusler ordering X_2YZ ($L2_1$) where Co and Ga(Zn) share one simple cubic sublattice (cf. Fig. 3.5). For $L2_1$ ordering, two energy minima are found while for the (XY)XZ order with Co on one of the two Fe sublattices (X site), the cubic phase is clearly favoured.

including the influence of disorder may be important for the Fe-Co-Ga-Zn alloys and may drive the inverse alloys towards martensitically unstable systems, a prerequisite to observe the MSME. In addition, one can expect that a disordered alloy may be more ductile. The *ab initio* calculations of the corresponding $Co_2FeGa(Zn)$ systems reveal that here the structural ordering tendency is opposite compared to the $Fe_2CoGa(Zn)$ systems, cf. Fig. 8.3. The conventional Co_2FeGa compound is lowest in energy but not martensitic, contrary to the inverse (CoFe)CoGa alloy which possesses a martensitic energy profile but lies higher in energy. For the Zn-based alloys a similar situation is encountered. The conventional Co_2FeZn alloy is lowest in energy but does not show a tendency for a martensitic instability, while the energy profile of the (CoFe)CoZn system is martensitic but energetically unfavorable.

Concerning magnetism, it is found that in the inverse Fe-Co-Ga(Zn) structures the magnetic moments roughly follow the variation of the energy curve (cf. Fig. 8.2). However, in the X_2YZ order they do not change significantly under tetragonal distortion. Comparing the cubic inverse Fe-Co-Zn compound with the cubic inverse Fe-Co-Ga system the magnitude of the total moment per formula unit is enhanced by about 12%. When discussing magnetism for the corresponding Co-rich systems one always has to bear in mind that Co_2FeGa is a half-metal, compare Fig. 8.4 which shows the DOS of $L2_1$ Co_2FeGa, cubic (CoFe)CoGa, and $L2_1$ Co_2FeZn. The semiconducting gap of the half-metallic

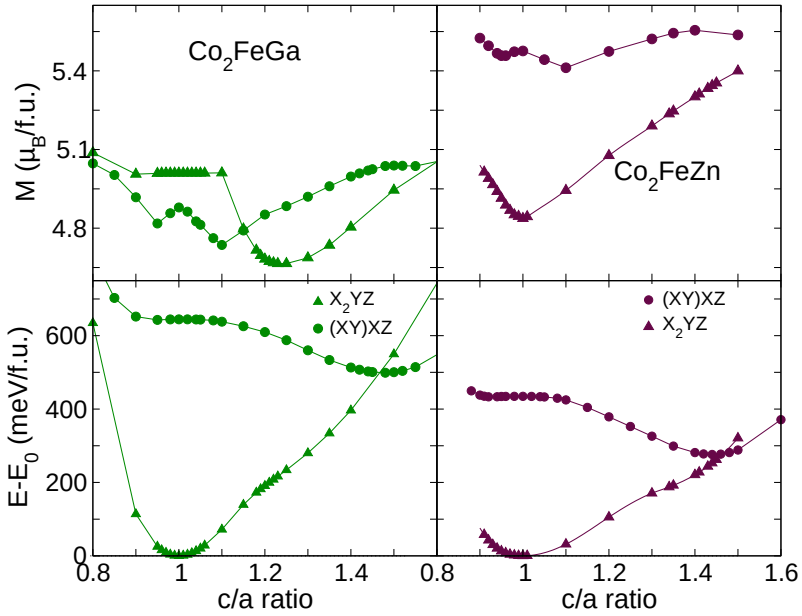

Figure 8.3: Variation of the total energy as a function of the tetragonal distortion c/a and the corresponding magnetic moments M (in μ_B/f.u.) for Fe-Co-Ga (left) and Fe-Co-Zn (right). Labeling as in Fig. 8.2. The X_2YZ order is energetically favored but not martensitic while for the (XY)XZ order two energy minima are found.

full Heusler alloys can be explained by a detailed inspection of the crystal fields acting on the different atoms in the Heusler structure. While the X atoms are affected by an octahedral crystal field, the Y and the Z atoms are subject to a tetrahedral crystal field. As a result part of the antibonding d-electronic states of the X atom (e_u and t_1u) are orthogonal to the d-electronic states of the Y atom are thus cannot hybridize. This leads for appropriate e/a ratios to an energy gap in the minority spin channel. For further details I refer to the Appendix in which a short excursion to crystal fields and the resulting hybridization is given (section 11.1). Due to the semiconducting gap at the Fermi energy in the minority spin channel the cubic half-metallic Heusler systems do not undergo a martensitic transformation [93] which is reflected in the binding curve of Co_2FeGa which does not show a tendency for a martensitic instability. The half-metallic gap in the minority spin channel of Co_2FeGa explains the integer total magnetic moment of $M = 5\mu_B$ at $c/a = 1$ and is also responsible for the plateau in the binding curve in the vicinity of the cubic phase. Due to the semiconducting gap a rearrangement of the electrons under tetragonal distortion is not possible. Very interesting is the comparison of the cubic conventional Co_2FeGa system with the cubic inverse (CoFe)CoGa system. The exchange of one of the two X atoms with the Y atom in the inverse structure can be seen as a first step towards disorder causing the semiconducting gap to disappear for cubic (CoFe)CoGa because it is partially filled with one-electron states, cf. Fig. 8.4(c). This is also reflected in the total magnetization curves because the integer total magnetic moment is lost for cubic (CoFe)CoGa. The loss of the half-metallic character due to atomic disorder has recently been investigated by means of *ab initio* methods for ordered and

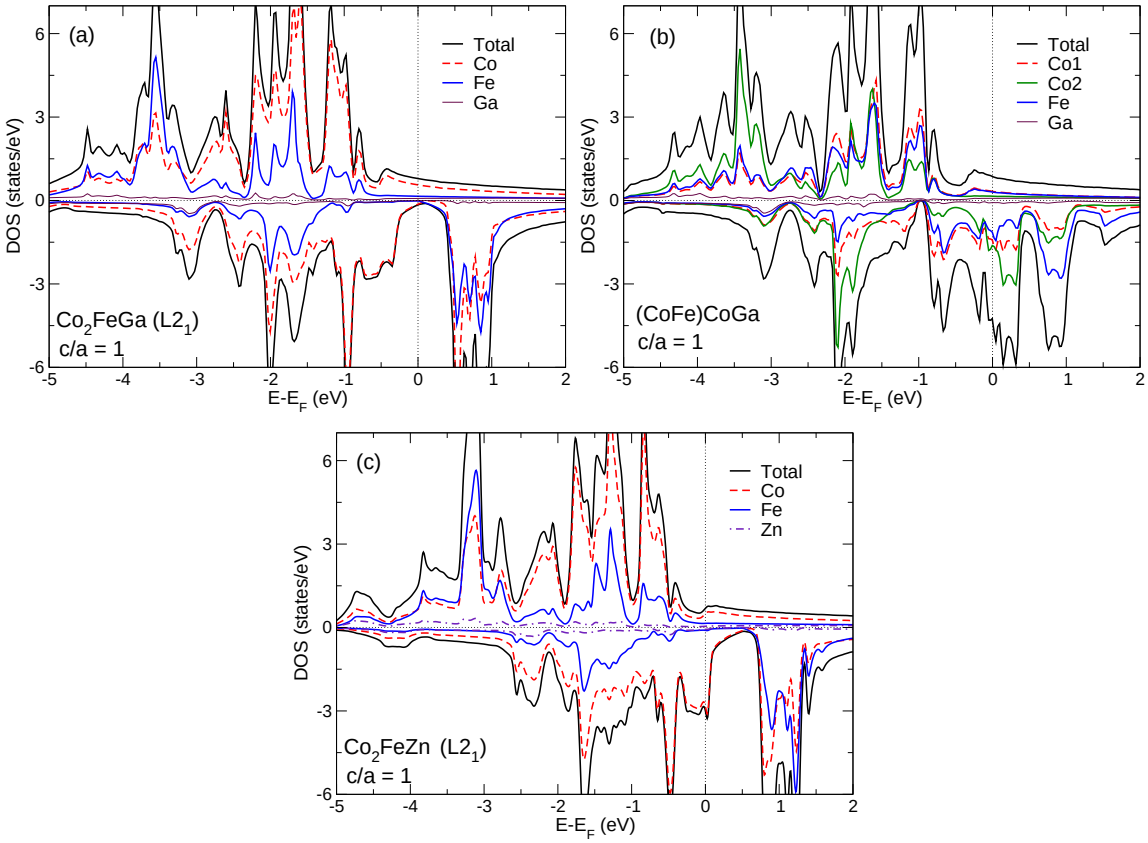

Figure 8.4: Total and atom-resolved DOS of (a) $L2_1$ Co_2FeGa, (b) cubic (CoFe)CoGa, and (c) $L2_1$ Co_2FeZn. (a) The half-metallic gap in the minority-spin channel of $L2_1$ Co_2FeGa is clearly visible. (b) As a result of incipient disorder the semiconducting gap has disappeared in the inverse (CoFe)CoGa system. (c) With decreasing e/a in Co_2FeZn E_F is shifted to lower energies as in a rigid-band fashion.

disordered Co_2FeSi [93].

In the corresponding Co-Fe-Zn compounds which have one electron less than the Co-Fe-Ga alloys the half-metallic character has vanished due to the reduced e/a resulting in a reduced filling of the minority spin channel as in a rigid band-like model, cf. Fig. 8.4(c). A significant enhancement of the magnetic moment is found for the inverse (CoFe)CoZn compared to the conventional Co_2FeZn system. Taking the cubic conventional structure as a reference, the increase in the total magnetic moments amounts to about 12%. This deviates from my results obtained so far for the Ni-Co-Ga(Zn) and Co-Ni-Ga(Zn) compounds (previous section) in which Zn substitution always had a beneficial impact on the magnetic properties of the alloy. However, Co_2FeGa is an exception because it is a half-metal and thus possesses 100% spin polarization at the Fermi level. Due to the large half-metallic gap the changes in the minority spin DOS induced when Ga is replaced by Zn does not affect the total magnetic moment in such a sensitive manner as for the metallic Heusler systems. The calculated total

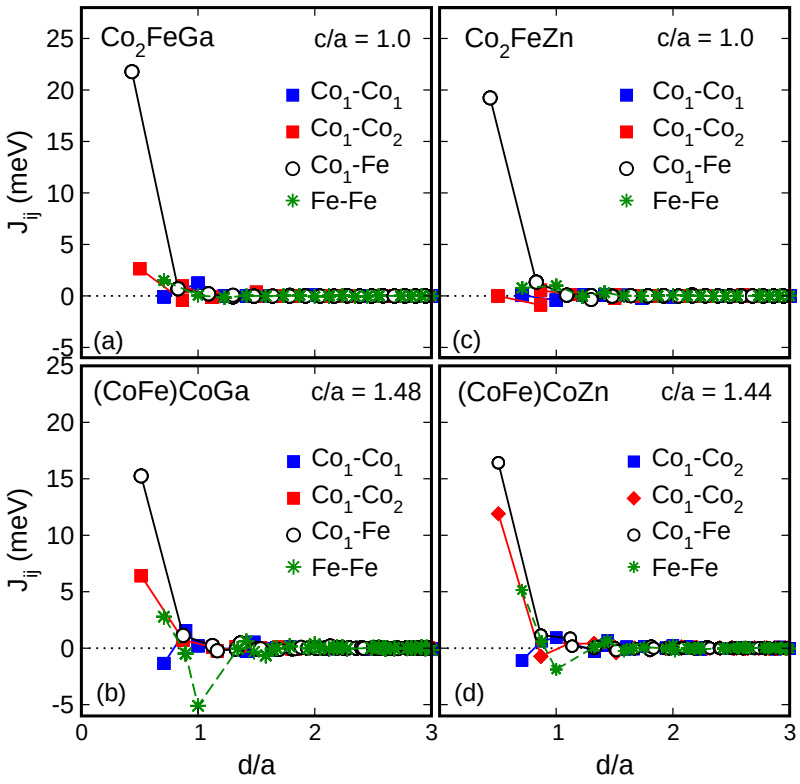

Figure 8.5: Magnetic exchange coupling constants, J_{ij}, of conventional and inverse Co-Fe-Ga Heusler alloys on the left and Co-Fe-Zn on the right. (a) Conventional Co_2FeGa at $c/a = 1.0$, (b) inverse (CoFe)CoGa at $c/a = 1.48$, (c) Co_2FeZn at $c/a = 1.0$, and (d) (CoFe)CoZn at $c/a = 1.44$. Color coding and symbols as in Fig. 7.3 for the Co_1-Co_1 and the Co_1-Co_2 interactions. The Co_1-Fe coupling is marked by black open circles and the Fe-Fe interaction is indicated by green stars.

magnetic moment of 5.0 μ_B for Co_2FeGa is in line with the experimental value of 5.13 μ_B at 5 K [126].

For the c/a ratios of the energy minima the magnetic exchange coupling constants have been calculated which are shown in Fig. 8.5 for the Co-Fe-Ga(Zn) alloys and in Fig. 8.8 for the Fe-Co-Ga(Zn) systems. The most significant interaction is ferromagnetic and occurs between nearest neighbor Co and Fe atoms. For the inverse structures this strong Co_1-Fe interaction is reduced while simultaneously ferromagnetic nearest neighbor Co_1-Co_2 coupling evolves. Also slight antiferromagnetic correlations between Fe atoms of neighboring unit cells emerge. But the overall coupling is predominantly ferromagnetic which results in high Curie temperatures between T_C = 770 K (Fe_2CoGa), T_C = 925 K (Fe2CoZn), T_C = 1000 K (Co_2FeGa), and T_C = 913 K (Co2FeZn). For the half-metal Co_2FeGa good agreement is observed with the experimental results which reports a Curie temperature of T_C= 1093 K [127]. In order to evaluate the structural stability, the mixing energies are calculated, cf. Table 8.1 and Table 8.2. The Fe-Co-Ga compounds have negative mixing energies and are therefore stable.

Table 8.1: Calculated equilibrium parameters of tetragonally distorted Co-Fe-Ga and Co-Fe-Zn. Parameter labeling as in Table 7.1.

	Co_2FeGa ($e/a = 7.25$)		Co_2FeZn ($e/a = 7$)	
	X_2YZ	(XY)XZ	X_2YZ	(XY)XZ
a	5.725	5.732	5.708	5.739
c/a	1.0	1.48	1.0	1.44
M	5.00	5.02	4.86	5.57
E_{mix}	-958	-459	-167	105
T_C^A	1000	672	913	832
$\Delta E_{c/a}$	/	36	/	39
ΔE_{order}		-125		-69

However, the Zn-based Fe-Co-Zn alloys possess positive mixing energies which implies that these alloys will show segregation tendencies during experimental making. For the Co-rich compounds negative mixing energies are found for both ordering types in the Ga-based alloys. For the Zn-based systems the mixing energy increases and finally reverses its sign from negative to positive values for (CoFe)CoZn. This is in good agreement with the results for E_{mix} under Zn substitution discussed in the previous chapters. The structural stability is reduced when Zn is substituted for Ga. Within one fixed composition the mixing energy reflects the hierarchy of the total energy curves.

8.2.2 Conclusion

In summary, despite the high Curie temperatures obtained for all systems under investigation in this chapter, neither the $Fe_2CoGa(Zn)$ nor the $Co_2FeGa(Zn)$ systems are appropriate for future FSMA applications owing to the fact that for the Fe-rich systems the inverse Heusler structure is energetically preferred which is not martensitic while for the Co-rich systems the conventional Heusler structure is energetically favored which does not show a second energy minimum. The first-principles calculation are in perfect agreement with the experimentally observed trend that transition metal atoms to the right of Fe in the periodic table (in the case here, Co and Ni) preferentially occupy the X-sites while Fe and elements to the left of Fe favor the Y-sublattice (as Mn in Ni_2MnGa). Also for the Curie temperature and the total spin moment of the half-metal Co_2FeGa the theoretical and the experimental results match very well. One may judge from the T_C and $\Delta E_{c/a}$ values listed in Table 8.1 that in case of atomic disorder the resulting alloys show magnetic shape-memory effects.

8.3 $Fe_2CoGa_{1-x}Zn_x$

For all X_2YZ Heusler systems investigated so far (apart from the half-metallic Co_2FeGa systems) a clear trend could be found concerning influence of the Z element when replacing Ga by Zn. In general, Z is the element which introduces (s,p)-valence electrons and helps to stabilize the Heusler

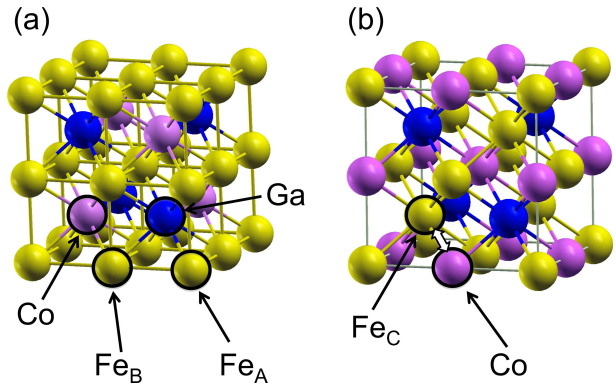

Figure 8.6: (a) The conventional Heusler structure for the case of Fe_2CoGa. (b) The inverse Heusler ordering for (FeCo)FeGa in which the Co and one Fe atom have exchanged their site. As a consequence, the two inequivalent Fe atoms (Fe_A and Fe_C) in the inverse Heusler cell are affected by different crystal fields.

structure. Independent of the site occupancy of the transition metal atoms Ni, Co, and Fe on the X- and Y-sublattices, the addition of Zn is beneficial for the magnetic properties of the Heusler alloys by increasing the total magnetic moment and the Curie temperature. At the same time the miscibility is reduced which renders the experimental fabrication of alloys with higher Zn content a challenging task. In order to gain further insight into the influence of Zn on the structural, magnetic, electronic properties, and lattice vibrations, the successive addition of Zn in the quaternary $Fe_2CoGa_{1-x}Zn_x$ compound will be considered in this section. In order to deal with aspects of structural stability of the conventional versus the inverse structure, also mixing energies and phonon dispersion relations of both types of structures of Fe_2CoGa, Fe_2CoZn, and $Fe_2CoGa_{1-x}Zn_x$ alloys are investigated. Part of this chapter has been published in [129]. In total, these systems may be of interest for future shape-memory devices. See also the following discussion.

8.3.1 Results and discussion

In this chapter the nearest neighbor environment and the coordination of the single atoms in the conventional and in the inverse Heusler structure will be discussed in detail. Therefore, the unit cells of the two Heusler orderings are shown again in Fig. 8.6 for the case of Fe_2CoGa. The in-equivalent Fe atoms are labeled by $Fe_{A,B,C}$.

8.3.1.1 Structural and magnetic properties

By means of total-energy calculations as a function of the lattice constant the equilibrium lattice constants and magnetic moments are determined for all systems and listed in Table 8.2.
The effect of the addition of zinc on the energy landscape and on the total magnetic moment when passing from Fe_2CoGa and $Fe_2CoGa_{1-x}Zn_x$ to Fe_2CoZn can be discussed on the basis of Fig. 8.7.

Table 8.2: Calculated equilibrium parameters of cubic and tetragonal ternary Fe_2CoGa and Fe_2CoZn and quaternary $Fe_2CoGa_{1-x}Zn_x$ systems in the conventional X_2YZ and in the inverse (XY)XZ Heusler structure. Parameters as in Tab. 7.1. In addition, the valence electron concentration e/a and the stable structure (St) at $T = 0$ K (absolute energy minimum) are given. 'unst' refers to an unstable structure.

System	e/a	St	a_0 (Å)	c/a		M (μ_B/f.u.)	T_C	$\Delta E_{c/a}$	ΔE_{order}	E_{mix}
Conventional										
Fe_2CoGa	7	$L1_0$	5.774	0.88	1.46	6.08	770	56	44	-463
$Fe_2CoGa_{0.75}Zn_{0.25}$	6.9375	$L1_0$	5.779	0.91	1.44	6.22	802	54	31	-333
$Fe_2CoGa_{0.25}Zn_{0.75}$	6.8125	$L1_0$	5.780	0.9	1.42	6.51	896	49	6	-721
Fe_2CoZn	6.75	unst	5.782	0.92	1.40	6.64	925	48	-9	51
Inverse										
(FeCo)FeGa	7	cubic	5.736	1.0	/	5.29	780	/		-642
(FeCo)$FeGa_{0.75}Zn_{0.25}$	6.9375	cubic	5.744	1.0	/	5.58	768	/		-458
(FeCo)$FeGa_{0.75}Zn_{0.75}$	6.8125	cubic	5.748	1.0	/	5.58	830	/		-328
(FeCo)FeZn	6.75	unst	5.750	1.0	1.36	5.95	850	-11		135

Two remarkable modifications are observed. First, Zn reduces considerably the energetic preference of the inverse cubic structure in favor of the tetragonally distorted conventional structure. In the ternary compound Fe_2CoGa the energy difference between the absolute energy minima of inverse and conventional structures, ΔE_{order}, amounts to 44 meV/atom. This difference reduces to 31 meV/atom for $Fe_2CoGa_{0.75}Zn_{0.25}$ and to 6 meV/atom in $Fe_2CoZn_{0.75}Ga_{0.25}$. Finally, for Fe_2CoZn this energy difference reverses its sign yielding -9 meV/atom. This trend emphasizes the discussion in the previous section that in ternary Fe_2CoZn in contrast to Fe_2CoGa the tetragonal conventional Heusler structure is the energetically preferred phase (cf. also Table 8.2 and Fig. 8.2). The substitution of Zn for Ga does not significantly modify the energy profile of $E(c/a)$ of the conventional Heusler systems, contrary to the inverse structures for which the tendency of a second energy minimum at $c/a > 1$ becomes significantly more pronounced the more Zn is added. A hint towards this trend has also already been observed in the previous section for (FeCo)FeZn. The enhanced tendency for a second energy minimum implies that the inverse structures become elastically softer, which influences the magnetostrictive coefficient $\lambda_{[001]}$ of the cubic phase of the Heusler alloys. (The magnetostrictive coefficient is the fractional change in length as the magnetization of the material increases from zero to the saturation value.) Regarding the effect of softer elastic behavior when substituting Zn for Ga in Fe_2CoGa, good agreement with results of Wu *et al.* is obtained who found that the magnetostrictive coefficient $\lambda_{[001]}$ of $Fe_{87.5}Ga_{12.5}$ can be further enhanced by the substitution of Zn for Ga [130]. The softening of the inverse structure with increasing amount of zinc is also reflected in the phonon dispersions, see Fig. 8.10. The frequencies of the lowest acoustical branch of (FeCo)FeZn are significantly lower compared with (FeCo)FeGa along the [110] direction.

The upper panel in Fig. 8.7 shows that the conventional Fe_2CoGa and Fe_2CoZn compounds and corresponding substitutional alloys have larger or similar magnetic moments compared with the inverse

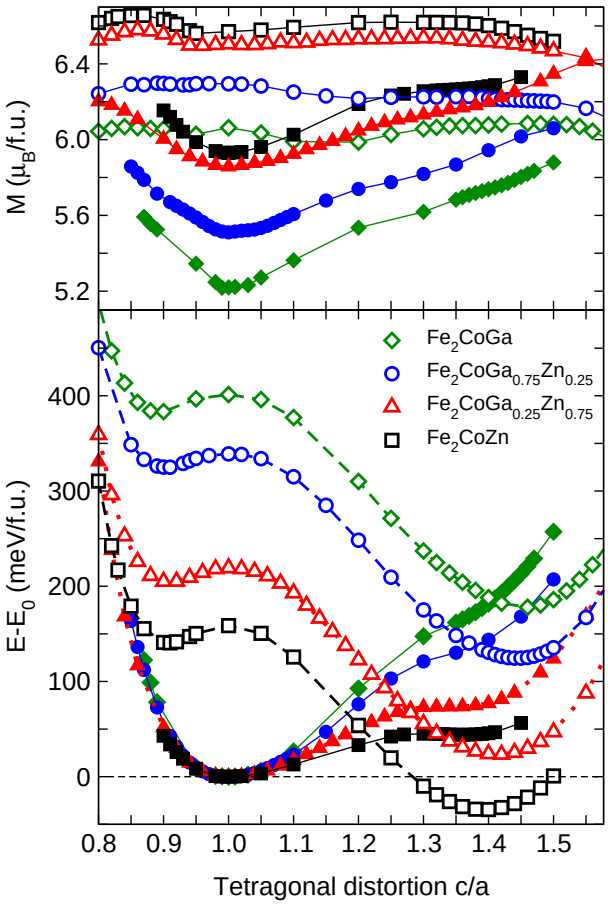

Figure 8.7: Total energy E-E_0 (lower panel) with respect to the energy of the cubic inverse structure for each alloy system and magnetic moment M per formula unit (f.u.) (upper panel) of Fe_2CoGa (green diamonds), $Fe_2CoGa_{0.75}Zn_{0.25}$ (blue circles), $Fe_2CoZn_{0.75}Ga_{0.25}$ (red triangles), and Fe_2CoZn (black squares) for both crystal structure types as a function of the tetragonal distortion c/a. Open and filled symbols distinguish between the conventional and inverse Heusler structures, respectively. The conventional Heusler structures are characterized by two energy minima while the inverse structures show only one energy minimum in the cubic state ($c/a = 1$). With increasing Zn concentration the energy of the conventional Heusler structure is considerably lowered approaching the energy curve of the corresponding inverse structure while the magnetic moments increase.

systems, see Table 8.2 and 8.3. In conventional Fe_2CoGa each Fe has four Co *nn* (nearest neighbors) and four Ga *nn* while each Co has 8 Fe nn, compare Fig. 8.6. This yields 2.24 μ_B for Fe and 1.76 μ_B for Co. Zinc instead of Ga leads to a slightly enhanced Fe-moment (2.50 μ_B) whereas Co remains unaffected (1.74 μ_B). For the inverse structure two inequivalent Fe-atoms exist. Fe_A has four Fe and four Ga *nn* whereas Fe_C has four Fe and four Co nn. This particular environment of Fe_C at the bcc-sublattice cube center and four Fe and four Co *nn* at the cube edges corresponds to the same environment as one of the Fe atoms in Fe_3Co [63] and seems to favor the inverse over the conventional

Table 8.3: Element-specific (in μ_B/atom) and total magnetic moment (in μ_B/f.u.) of the conventional and inverse Fe-Co-Ga-Zn Heusler structures for $c/a = 1$. The magnetic moments do not change much when the cell is tetragonally distorted ($c/a \neq 1$). For comparison, the corresponding magnetic moments for the inverse cubic structures are added.

System	M(Fe$_A$)	M(Fe$_C$)	M(Co)	M(Ga)	M(Zn)	M
Conventional						
Fe_2CoGa	2.24	/	1.76	-0.08	/	6.15
$Fe_2CoGa_{0.75}Zn_{0.25}$	2.33	/	1.77	-0.08	-0.05	6.36
$Fe_2CoGa_{0.25}Zn_{0.75}$	2.45	/	1.76	-0.08	-0.05	6.60
Fe_2CoZn	2.50	/	1.74	/	-0.05	6.68
Inverse						
(FeCo)FeGa	1.79	2.59	1.08	-0.09	/	5.36
(FeCo)$FeGa_{0.75}Zn_{0.25}$	2.0	2.57	1.18	-0.10	-0.07	5.65
(FeCo)$FeGa_{0.75}Zn_{0.75}$	2.23	2.54	1.29	-0.11	-0.072	5.98
(FeCo)FeZn	2.30	2.52	1.32	/	-0.08	6.06

Heusler structure. For (FeCo)FeZn this leads to 2.30 μ_B for Fe$_A$ and 2.52 μ_B for Fe$_C$ and 1.32 μ_B for Co (Co has four Fe *nn* and four Zn *nn* which explains the rather low moment of Co in the inverse structure). The enhanced magnetic moments of Fe$_A$ and Fe$_C$ compared with the bulk value, is similar to the behavior of the spin moments of both Fe in Fe_3Co [63]. Since for the inverse structure the covalent interaction between Fe and Co *nn* is strong in each spin channel, it bears features of covalent magnetism as in FeCo [63], which finally lowers the total energy of the inverse structure compared with the conventional one. This is explained in detail below in the discussion of the electronic structure.

Figure 8.7 also shows that in the inverse (XY)XZ structure the total moments follow the overall trend found in the energy profile and show a well-defined minimum for the cubic state. Comparing conventional Fe_2CoGa and Fe_2CoZn one may tentatively conclude that the reduced occupation of the minority-spin channel of Fe_2CoZn (Zn has one valence electron less than Ga) gives rise to the enhanced total moment of the Zn-based compounds. It is clear from the present investigation that Fe favors a bcc-like environment in Fe_2CoGa and Fe_2CoZn as it is the case for other magnetic Heusler alloys with two inequivalent Fe as in Fe_3Co [63] and Fe_3Si [131]. However, only in the inverse structures the strong ferromagnetic nearest neighbor Fe$_C$-Fe$_A$ and Fe$_C$-Co interactions can evolve which are plotted in Fig. 8.8.

8.3.1.2 Curie temperatures

The resulting Curie temperatures are given in Table 8.2. In the upper panels of Fig. 8.8 the magnetic coupling constants are given for the conventional and in the lower panel for the inverse structures. The magnetic exchange coupling constants show strong ferromagnetic coupling of Fe$_A$-Co and Fe$_A$-Fe$_B$ pairs of atoms in the conventional and between Fe$_C$ and Co atoms and Fe$_C$ and Fe$_A$ atoms in

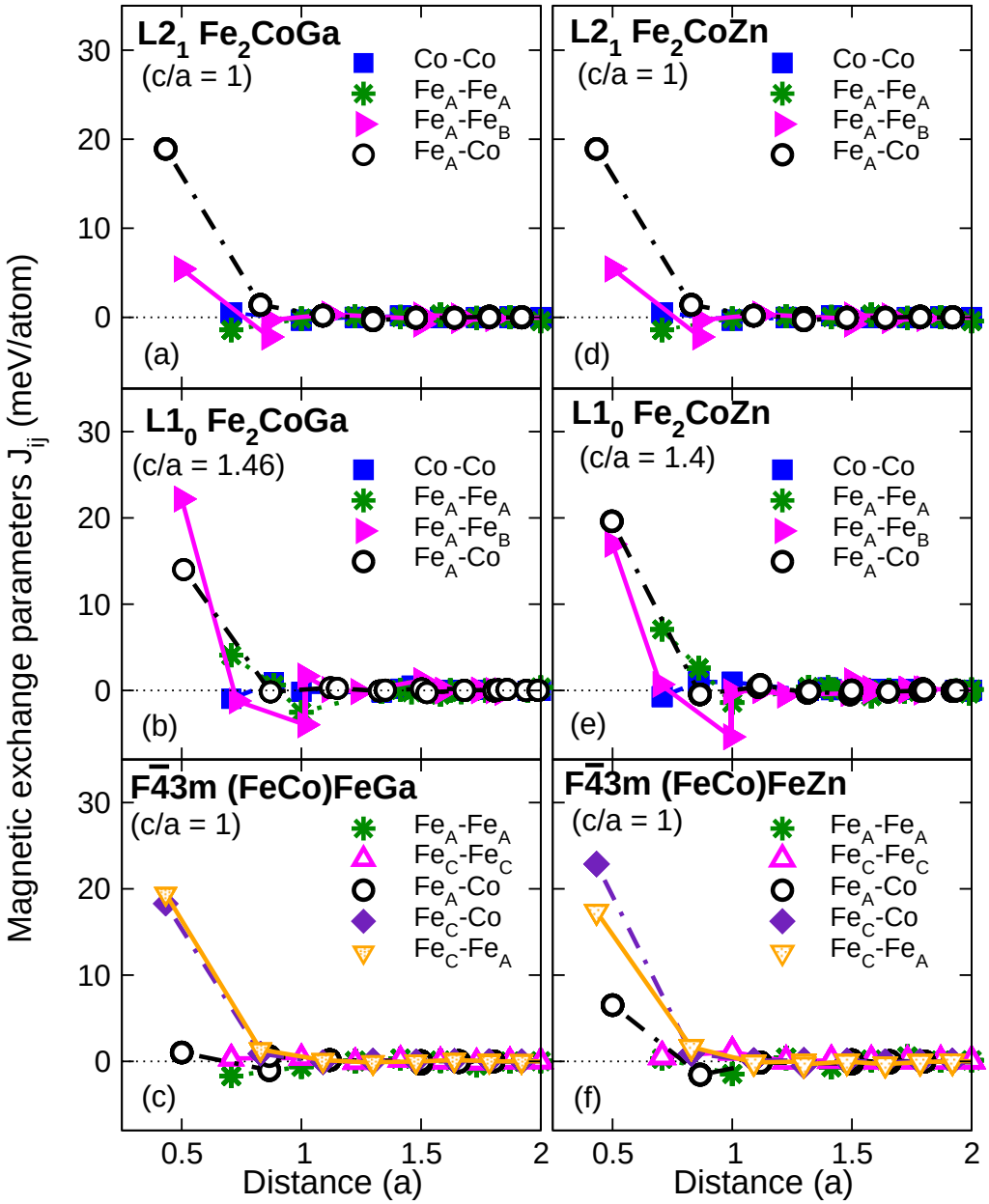

Figure 8.8: Magnetic exchange parameters J_{ij} as a function of the distance d between the atoms in units of the equilibrium lattice constant a_0 for the cubic cases ($c/a = 1$) and in units of a for the tetragonal structures for (a) $L2_1$ Fe_2CoGa ($c/a = 1$), (b) $L1_0$ Fe_2CoGa ($c/a = 1.46$), (c) inverse $F\bar{4}3m$ (FeCo)FeGa ($c/a = 1$), (d) $L2_1$ Fe_2CoZn ($c/a = 1$), (e) $L1_0$ Fe_2CoZn ($c/a = 1.40$), and (f) inverse $F\bar{4}3m$ (FeCo)FeZn ($c/a = 1$). For the Fe_x-Fe_y interaction (x,y = A, B, C) there is always an Fe_x-atom at the origin, for the Co-Co interactions a Co-atom occupies the origin. Parameter labeling as in Fig. 7.3. The stars (green) define here the Fe_A-Fe_A interactions, filled rightwards triangles (magenta) belong to the Fe_A-Fe_B interactions, and open circles (black) mark the interactions between Fe_A and Co. Open upwards triangles (magenta) indicate the Fe_C-Fe_C interaction, filled diamonds (indigo) show the Fe_C-Co interactions, and downwards triangles (orange) the the Fe_C-Fe_A interactions. The strongest interactions are ferromagnetic and appear between Fe atoms and Fe and Co atoms. Labeling A, B, and C can be taken from Fig. 8.6.

the inverse structure. This results in rather high Curie temperatures between 770 K and 925 K (cf. Table 8.2). In the tetragonally distorted conventional Heusler structure also slight antiferromagnetic tendencies appear between Fe_A-Fe_B atoms which show up at distances of one lattice constant. The highest Curie temperature of 925 K is found for the conventional Fe_2CoZn compound. This enhancement of about 150 K compared to $T_C = 770$ K of the conventional Fe_2CoGa compound is caused by the increased Fe_A-Fe_A coupling and goes hand in hand with the enhancement of the total magnetic moment of Fe_2CoZn. As for the ternary compounds Fe_2CoGa and Fe_2CoZn, strong ferromagnetic coupling in the $Fe_2CoGa_{1-x}Zn_x$ alloys is found and the Curie temperatures are high, T_C = 768 K for $Fe_2CoGa_{0.75}Zn_{0.25}$ and T_C = 830 K for $Fe_2CoGa_{0.25}Ga_{0.75}$ (cf. Table 8.2).
I summarize in Fig. 8.9 the influence of the stepwise addition of Zn to $L1_0$ Fe_2CoGa on the Curie temperature, the energy difference between the cubic phase at $c/a = 1$ and the energy minimum at $c/a > 1$, $\Delta E_{c/a}$, the mixing energy, E_{mix}, and on the energy difference between favorable structures of conventional and inverse phases, ΔE_{order}. The Curie temperature increases almost linearly with increasing Zn content (decreasing e/a ratio), simultaneously, $\Delta E_{c/a}$ decreases only slightly. These are desirable results in order to enhance the operation temperatures of future FSMA. The mixing energy shows a perfect linear increase with decreasing e/a ratio, while ΔE_{order} decreases steadily which establishes the stabilization of the conventional Heusler structure with increasing amount of Zn. The remarkably linear dependence of all functional properties on the valence electron concentration e/a suggests the possibility of discussing the results in a rigid band-like picture. This will be done in Section 8.3.1.4 to obtain further qualitative understanding, in particular of the role of covalent magnetism in favor of the inverse structures. To summarize, successive substitution of Zn for Ga in Fe_2CoGa is beneficial for enhancing the Curie temperature and for the stabilization of the conventional Heusler structure while simultaneously the martensite transformation temperature, which is propotional to $\Delta E_{c/a}$, can be kept high. Although the fabrication of Zn-rich $Fe_2CoGa_{1-x}Zn_x$ samples with slightly negative mixing energies will be demanding, the system has promising properties which make it worthwhile for systematic experimental investigation. From the theoretical point of view, further investigation of the role of disorder in $Fe_2CoZn_{0.75}Ga_{0.25}$ is necessary to establish the relation between flat energy profiles and high Curie and martensite transformation temperatures.

8.3.1.3 Lattice dynamics

In order to check whether the new materials are martensitically unstable at low temperature, the inspection of the phonon dispersion relation is of fundamental interest. This gives information about in how far softening of the austenite phase occurs which is often considered as a precursor of a premartensitic or martensitic transformation. The Heusler structure is an open bcc structure and thus its vibrational properties bear resemblance to lattice dynamics of open bcc phases. One of the main features of open bcc phases is that {110} planes can be easily shifted along the $[1\bar{1}0]$ direction resulting into low values of the energies of the transverse [110]-TA_2 phonon branch (cf. chapter 5.4). In order to clarify if phonon softening also appears in the Fe-Co-Ga-Zn alloys, Mario Siewert has

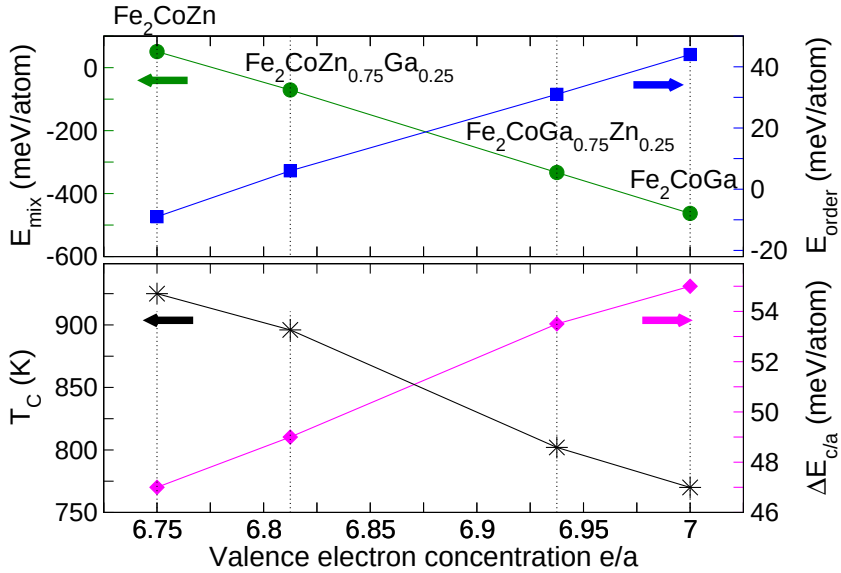

Figure 8.9: The influence of addition of Zn to Fe_2CoGa in the conventional tetragonally distorted Heusler structure ($L1_0$) on the Curie temperature T_C (left axis, lower panel), the energy difference between the cubic phase at $c/a = 1$ and the absolute energy minimum at $c/a > 1$, $\Delta E_{c/a}$ (right axis, lower panel), the mixing energy E_{mix} (left axis, upper panel), and the energy difference between the absolute energy minima of the conventional and the inverse phases, E_{order} (right axis, upper panel), as a function of the valence electron concentration e/a. All functional behavior depends linearly on e/a.

calculated and analyzed the full phonon spectra of Fe_2CoGa, Fe_2CoZn, and, in addition, Fe_2CoCu (discussed in Sections 8.3.1.6 and 8.3.1.7) for the conventional as well as for the inverse Heusler structures. Results of his work are shown here because they provide essential information and serve as a foundation for the following interpretation and discussion. The dispersion relations of the cubic conventional Fe_2CoGa, and Fe_2CoZn structures are not shown here because of the negative curvatures of the total energies upon tetragonal distortions in the vicinity of $c/a = 1$ which lead to an extraordinarily large amount of imaginary dispersions which are obtained for the lattice vibrations in [110] direction. In contrast, for the inverse Heusler systems no imaginary phonons appear along the [110] direction (compare Fig. 8.10) which is consistent with the high stability of the cubic inverse phase in the Fe-excess FeCo-based Heusler systems. Apart from the X-point, the variation of the phonon branches does not differ significantly for (FeCo)FeGa and (FeCo)FeZn. However, the lowest acoustic branch that can be found at the X-point, reveals a clear decrease of the frequency for (FeCo)FeZn compared to (FeCo)FeGa. For (FeCo)FeCu even imaginary frequencies along the [110] direction are found at a wavevector rather similar to the vector where the phonon softening in Ni_2MnGa appears, compare Fig. 8.11. As discussed in Section 8.3.1.7, (FeCo)FeCu exhibit martensitic energy profiles for both Heusler orderings. The imaginary frequencies along the [110] direction could indeed hint towards an anomalous temperature dependence of phonon softening in the vicinity of a martensitic

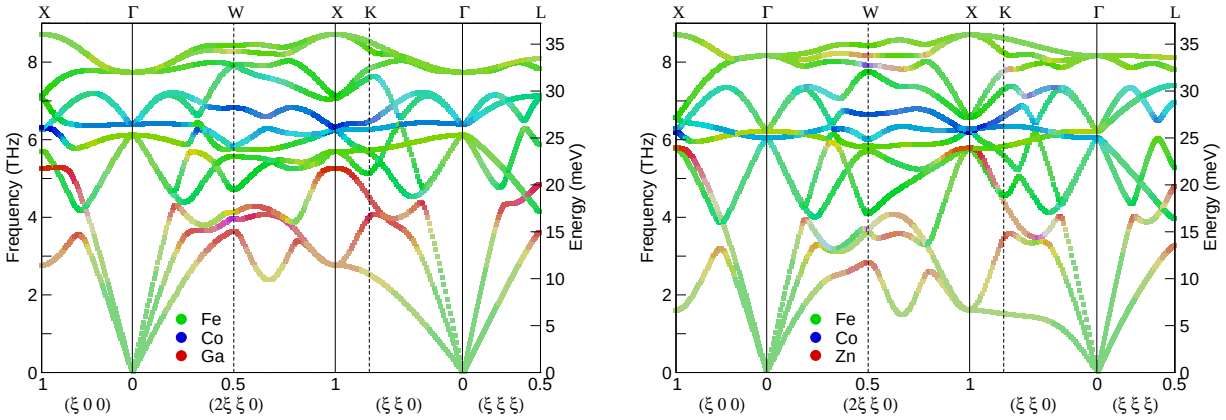

Figure 8.10: Phonon dispersion relations of the inverse cubic Heusler compounds (FeCo)FeGa (left) and (FeCo)FeZn (right) calculated by Siewert *et al.* [110]. For the inverse structure involving zinc, a tendency for phonon softening is observed regarding the TA_2 mode in [110] direction but no imaginary phonons are apparent, contrary to the conventional cubic systems $Fe_2Co(Ga, Zn)$ (not shown). For the latter compounds the negative curvature of $E(c/a)$ at $c/a = 1$ causes instabilities in the [110]-TA_2 phonon branch.

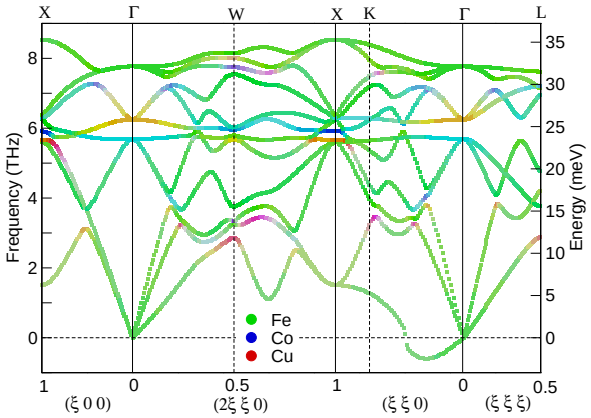

Figure 8.11: Phonon dispersion relations of the inverse cubic (FeCo)FeCu system calculated by Siewert *et al.* [110]. Along the [110] direction pronounced phonon softening up to imaginary frequencies is present which bear strong resemblance to the softening observed for Ni_2MnGa.

instability because imaginary frequencies do not occur in other regions of the Brillouin zone and also for the frequencies of the other branches no noteworthy modification is observed. The fact that the frequencies of the acoustic branches decrease with decreasing valence electron concentration e/a is in contrast to findings for other material classes like Ni_2MnZ, Ni_2CoZ or Co_2MnZ as it has been shown that the nearest neighbor force constants decrease linearly with increasing e/a ratio for these Heusler compounds [132].

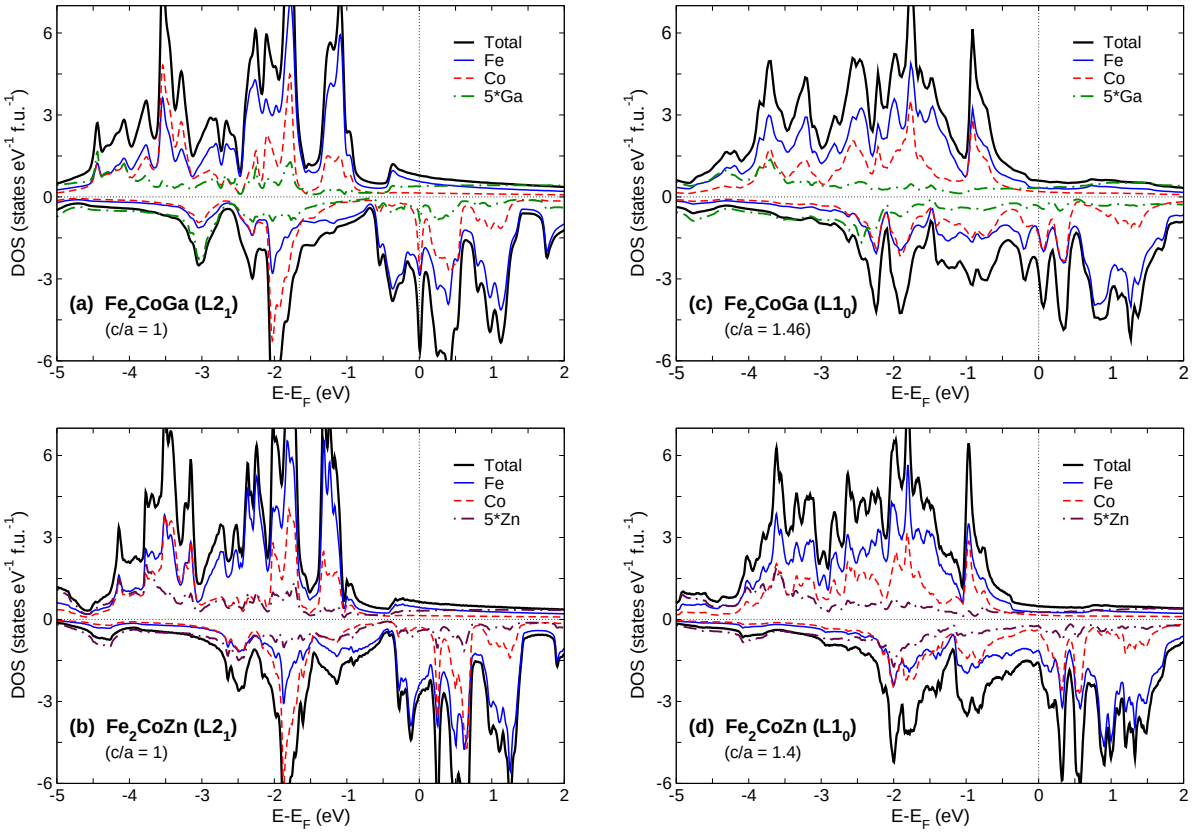

Figure 8.12: The two figures on the left show the total and element-specific DOS of the cubic $L2_1$ phases of (a) Fe_2CoGa and (b) Fe_2CoZn while the two figures on the right show the corresponding total and element-specific DOS of the tetragonal $L1_0$ phases of (c) Fe_2CoGa and (d) Fe_2CoZn. The high peak at the Fermi level in the spin-down channel in case of Fe_2CoGa is of Co-e_g origin and mainly responsible for the instability of the ordered conventional phase and may also favor the tetragonal distortion (band-Jahn-Teller effect) thereby lowering the energy of the $L1_0$ phase with respect to the $L2_1$ phase. For Fe_2CoZn a peak of mainly Fe-e_g and Fe-t_{2g} lies right below E_F (as in case of $L2_1$ Ni_2MnGa) which in this case is responsible for the instability. Note that for the $L1_0$ phase of both compounds the gap-like region of the cubic phase below E_F is now filled with states of Co and Fe. The thicker solid (black) lines show the total DOS, thinner (blue) lines belong to Fe (for $L1_0$ this is the sum of contributions from the two inequivalent atoms Fe_A and Fe_C), dashed (red) lines mark the Co states, dash-dotted (green) lines represent Ga and Zn (maroon), respectively. For better visibility the DOS of Ga and Zn is enhanced by a factor of 5.

8.3.1.4 Electronic structure

It was shown in Section 8.3.1.1 that in all investigated compounds Fe_2CoGa, Fe_2CoZn and structures with mixture of Ga and Zn, the inverse structure is always more stable than the conventional Heusler phase at $c/a = 1$. For the Fe_2CoGa and the $Fe_2CoGa_{1-x}Zn_x$ systems, the inverse structure

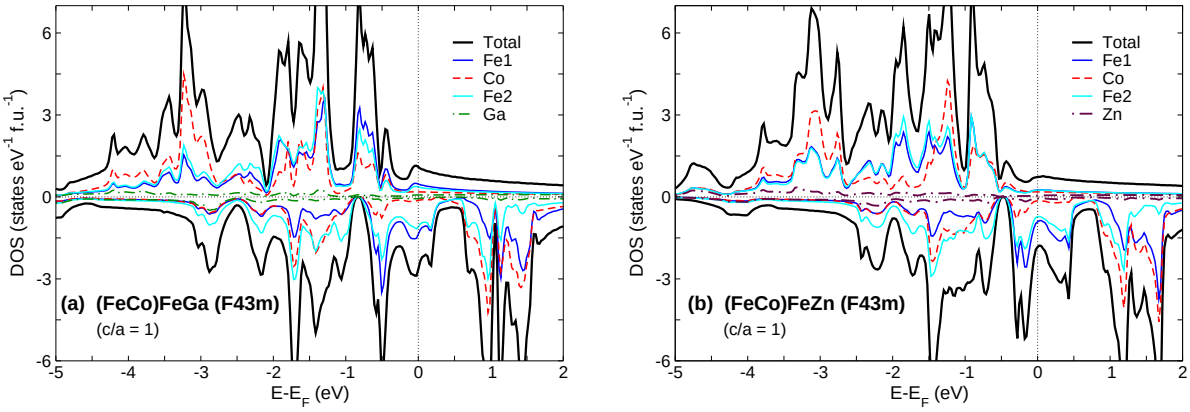

Figure 8.13: The DOS of the inverse structures for the cubic case for (a) (FeCo)FeGa and (b) (FeCo)FeZn. The individual contributions of both inequivalent Fe are shown in blue and violet. There are two pseudogap structures below (-0.8 eV) and above (0.5 eV) the Fermi level. The DOS of the minority-spin appears rather compressed and the peak structure at E_F has disappeared compared with the conventional case.

is even more favorable than the tetragonally distorted conventional Heusler phase. Remarkable is the linear reduction of the energy difference between the conventional and the inverse Heusler structure, ΔE_{order}, with increasing Zn content in $Fe_2CoGa_{1-x}Zn_x$. Hence, addition of zinc stabilizes the tetragonal conventional phases. This raises several questions: (i) What causes the instability of the cubic conventional $L2_1$ structure and what is the origin of the tetragonal distortion? (ii) When Zn is substitutionally replacing Ga: What causes the reduction of the energetic preference of the cubic inverse structure in favor of the tetragonally distorted conventional one? (iii) What is the reason for the high stability of cubic inverse structure and why are all conventional $Fe_2CoGa_{1-x}Zn_x$ structures martensitic and the inverse ones are not? (iv) When increasing the Zn-content in inverse (FeCo)$FeGa_{1-x}Zn_x$ alloys: What causes the trend for a second minimum in the $E(c/a)$ curves (filled triangles (red) and squares (black) in Fig. 8.7)? (v) Also the enhanced magnetic moments with increasing zinc content need to be understood.

In order to clarify these issues, the bandstructures and the electronic density of states of conventional and inverse structures are investigated.

(i) Some explanations can be obtained from the literature: The combinatorial study of inverse and conventional Heusler alloys by Gilleßen and Dronskowski [22] shows that the transformation from the conventional to the inverse structure occurs most easily whenever the atoms have similar (or identical) sizes (this holds for Fe and Co in the present study). In their analysis of chemical bonding in Fe_2CuGa they use the crystal-orbital Hamilton population (COHP) concept. It is a bond-detecting tool for solids (and molecules). Mathematically, COHP partitions the band structure energy (sum of the energies of the Kohn-Sham orbitals) in terms of orbital pair contributions. COHP analysis provides a quantitative measure of bond strengths and is an excellent choice for a first-principles calculation. In

particular, a COHP diagram indicates bonding, nonbonding, and antibonding energy regions within a specified band energy range while a COHP energy integral gives access to the contribution of a specific interatomic contact ("bond") to the band energy [133]. Gilleßen and Dronskowski use the COHP in the framework of the all-electron scalar-relativistic linear muffin-tin orbital (TB-LMTO) method, they could show that the driving force for adopting the inverse Heusler phase, for example in Fe_2CuGa results from strengthening of *nn* Fe-Fe and Cu-Ga bonds. This happens because the *nn* distance of Fe-Fe and Cu-Ga is drastically reduced compared with their corresponding distances in the conventional structure, where they are only next nearest neighbors. However, regarding tetragonal distortions, the conventional structure of Fe_2CuGa, when distorted, is even lower in energy than the inverse cubic structure. This is explained by the observation that Fe-Ga and Fe-Cu bonds which became weaker in the inverse cubic structure due to the loss of nearest neighbor coordination, regain strength while the short Fe-Fe and Cu-Ga bonds of the inverse structure are preserved. Gilleßen and Dronskowski found that in general Heusler compounds with a valence electron concentration $e/a < 7.25$ prefer the inverse cubic atomic arrangement while for those with an e/a ratio larger than 7.25 the tetragonal (inverse or conventional) arrangement of atoms is most favorable. Their results confirm the general trend of my findings since for all $Fe_2CoGa_{1-x}Zn_x$ alloys $e/a < 7.25$ holds for which the inverse structure is most favorable at $c/a = 1$ while for the Fe_2Co(Cu, Ag, and Au) compounds discussed in Section 8.3.1.7 $e/a > 7.25$ holds and the energetically favorable structure is tetragonal. The only exception is Fe_2CoZn with $e/a = 6.75$. But note that Fe_2CoZn has a positive mixing energy and is unstable with respect to spinodal decomposition.

Information about the electronic structure can be gained from the electronic density of states shown in Figs. 8.12-8.14. Figure 8.12 presents the total and element specific DOS for the cubic and the tetragonal phases of conventional and in Fig. 8.13 of inverse cubic structures, respectively. In addition, the e_g and t_{2g} contributions of Fe and Co are given in Fig. 8.14. A similar analysis has been done for the Ga-Zn-mixed phases where the DOS interpolates smoothly between the pure cases, Fe_2CoGa ($e/a = 7.0$) and Fe_2CoZn ($e/a = 6.75$). These figures are not shown here. Figure 8.12(a, b) shows the energetically unfavorable $L2_1$ structures and the corresponding energetically preferred $L1_0$ structures in (c, d). In this context one has to note that zinc has no *p*-electron and thus one valence electron less than gallium.

For all $L2_1$ phases the DOS of the minority-spins at the Fermi level is quite high, especially for Fe_2CoGa, cf. Fig. 8.12(a), where a sharp peak consisting of mainly Co and Fe states appears right at E_F similar to the case of the prototypical compound Ni_2MnGa. This is a hint that the system may undergo a structural transformation which leads to a region of small width of reduced DOS around E_F. The redistribution of spin-up and spin-down electrons may then lower the energy of the tetragonal structure with respect to the cubic structure which was discussed previously in terms of the band-Jahn-Teller effect for Ni_2MnGa [52]. In case of Fe_2CoGa, this redistribution is most clearly visible: The peak structure at E_F and further states below and above E_F develop a multi-valley structure of reduced Fe and Co DOS in the tetragonal phases. As for the prototypical compound Ni_2MnGa, the peak of

high DOS at E_F in the cubic phase is then shifted above E_F with much lower spectral weight (here, *spectral* refers to the energy spectrum) in the tetragonal phase. Thus, the martensitic transformation in Fe_2CoGa and Ni_2MnGa have the same origin.
The e_g and t_{2g} decomposed states in Fig. 8.14 show more clearly the states which are responsible for the instability of the conventional cubic phase. Fig. 8.14(a) shows that Co-e_g states contribute most of the spectral weight to the sharp peak at E_F in Fe_2CoGa which therefore is responsible for energy lowering by the band-Jahn-Teller effect upon tetragonal distortion. This explains the stability of the $L1_0$ phase relative to the cubic phase of Fe_2CoGa. Regarding the $Fe_2CoGa_{1-x}Zn_x$ systems the stability of the $L1_0$ phase has the same physical origin.
Another aspect concerns the occurrence of a pronounced pseudogap: For Ni_2MnGa this gap-like structure is found below E_F (just below the high DOS peak with Ni-e_g spectral weight) whereas for the cubic phases of Fe_2CoGa and Fe_2CoZn two pseudogaps are observed, one at 0.7 eV below E_F and another one at 1.5 eV above E_F. In Ni_2MnGa this near-semiconducting gap or pseudogap is caused by the missing hybridization of t_{1u} and e_u states of Ni with t_{2g} and e_g states of Mn due to the different symmetry of the crystal fields of octahedrally coordinated Ni (in the present case, Fe) and tetrahedrally coordinated Mn (in the present case, Co). See also the discussion in[134] regarding the origin of the half-metallicity of the full-Heusler alloys. This kind of gap structure is filled up with Co and Fe states in the tetragonal $L1_0$ phases of Fe_2CoGa and also Fe_2CoZn.

(ii) Another interesting effect is observed in the $L1_0$ structure when substituting Zn for Ga: With increasing Zn concentration the Co minority-spin DOS at E_F consisting of predominantly antibonding e_g and t_{2g} states is gradually reduced until finally E_F is pinned in a valley for $L1_0$ Fe_2CoZn. This is responsible for the approximately linear decrease of ΔE_{order} with decreasing e/a (increasing Zn concentration) (cf. Fig. 8.7 and Fig. 8.9). The hybridization of the Fe- and Co-*d* states with *sp*-states of Ga and Zn also leads to peak structures which are here only mentioned (the Zn-*d* band lies 7.5 eV below E_F and does not affect the Fe-Co hybridization too much): Part of the conduction-electron *s*-states of zinc strongly hybridize with Co-*d* and Fe-*d* states giving rise to the peak structures at about -4.1, -3.8 eV and -1.8 eV in the majority-spin DOS and at 0.3 eV in the minority-spin DOS.
Thus, one can conclude that the enhanced stability of the tetragonally distorted $L1_0$ phase compared to the cubic inverse phase for the Zn-rich alloys can be explained by stronger Co-Zn and Fe-Zn interactions due to stronger hybridization with zinc-*s* electrons. This is in good agreement with the results of Gilleßen *et al.* who found that in the tetragonal $L1_0$ phase of the conventional structure the Fe-Z (Z = Ga, or Zn, in the present case) bonds regain strength.
(iii) One still needs to understand the preference of the cubic phase of the inverse structure ($c/a = 1$) over the conventional structure and the absence of any sign of structural instability in the Fe-rich Fe-Co-based Heusler alloys. In this context it is helpful again to compare the DOS of conventional and inverse structures at $c/a = 1$ in Figs. 8.12(a, b) and 8.13. Interestingly, for the inverse cubic structures the pseudogap structure in the minority-spin channel (at about -0.8 eV for Fe_2CoGa) is much more

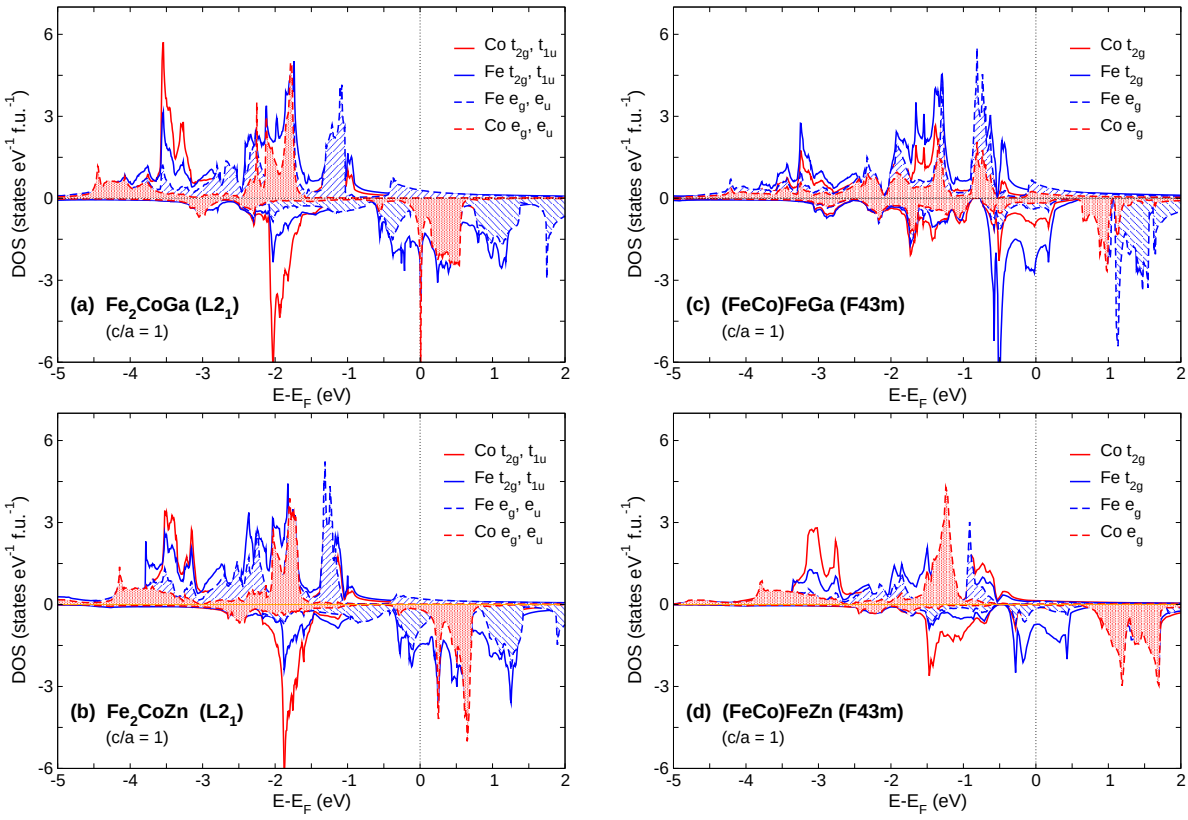

Figure 8.14: The e_g and t_{2g} decomposed DOS of conventional (a) Fe_2CoGa and (b) Fe_2CoZn showing the peak structure near the Fermi level which is responsible for the martensitic instability in both systems. The peak structure is less pronounced in case of Fe_2CoZn. Note also the extra spectral weight of Fe at energies above E_F and the extra spectral weight of Co at 2 eV below E_F in the minority-spin states which bears features of covalent magnetism as in CoFe, see Ref. [63] Figures (c) and (d) show the e_g and t_{2g} decomposed DOS of the corresponding inverse Heusler compounds. The peak structure at E_F has vanished and the DOS is rather different compared with the conventional structures.

pronounced and a second pseudogap at energies above E_F evolves (at about 0.5 eV for (FeCo)FeGa). A pseudogap in the minority-spin channel appears also for other inverse structures such as (FeCo)FeSi and (CoFe)CoSi [135]. The inverse structures show stronger hybridization of Co and Fe states due to the fact that in the inverse phase one Fe is interchanged with Co, see Fig. 3.5 so that now both, Fe and Co atoms, are subject to the same crystal field of tetrahedral symmetry which splits their *d*-orbitals only into t_{2g} and e_g symmetry and no longer into t_{2g} and t_{1u} and e_g and e_u symmetry as in the case of the crystal field of octahedral symmetry which acts on the Fe atom in the conventional structure. Due to symmetry reasons the hybridization is forbidden between antibonding states with *u* symmetry and bonding states with *g* symmetry [134]. Note, however, that this complex hybridization scenario does not lead to specifically low DOS at E_F for the inverse structures compared with the conventional ones.

Furthermore, the DOS of the tetragonal inverse structures (not shown here) reveals that (as for the tetragonal conventional phases), the bump in the majority-spin-channel above E_F which causes a bit of Fermi surface nesting for the spin-up electrons (not shown here) is dissolved and pseudogaps are filled with states although the inverse structures do not show a second energy minimum at $c/a > 1$. This implies that the inspection of the DOS alone is insufficient to explain the stability of the inverse structures at $c/a = 1$.

Therefore, the coordination and nearest neighbor relations in conventional and inverse atomic arrangements has been checked. In the inverse phase two different types of Fe exist, Fe_A and Fe_C (cf. Fig. 3.5). Fe_C is tetrahedrally coordinated by four *nn* Fe_A and four *nn* Co while Fe_A possesses Ga instead of Co as nearest neighbors. However, in the conventional cubic phase Fe atoms are only next nearest neighbors with octahedral coordination and build an unfavorable simple cubic Fe sublattice if one neglects for a moment Y and Z atom in the unit cell. In the conventional cubic $L2_1$ structure, the *nn* of Fe are four Ga and four Co atoms. Thus, only in the cubic inverse structure Fe_C can adopt a bcc-like environment of transition-metal atom neighborhood. This is the reason for the remarkable energetic preference of the inverse cubic structure in case of Fe-Co-Ga alloys. This tendency of Fe to prefer a bcc-like environment is also found in the studies of Co-Fe-Si alloys by Herper *et al* [135]. The authors observed that (FeCo)FeSi prefers an inverse atomic arrangement while Co_2FeSi is stable in the conventional $L2_1$ phase. This originates from the fact that Co atoms, in contrast to Fe atoms, prefer a more close packed, fcc (or hcp) neighborhood and agrees well with the experimental study of Fe-Co-Ga alloys by Jaggi *et al.* [125], and the *ab initio* investigation of Fe-Cu-Ga alloys by Gilleßen *et al.* [22]. One is tempted to consider other transition metal-rich Heusler alloys (with transition metals right to Fe in the periodic table) and check whether similar trends can be observed: For example, the stability of inverse and conventional structures of Ni_2MnGa [136] and Co_2NiGa [48]. For Ni_2MnGa the situation is opposite compared with Fe_2CoGa, i.e. the conventional structure is energetically clearly preferred at $T = 0$ K which confirms the assumption. Furthermore, in off-stoichiometric Ni-Mn-Ga alloys, *nn* Ni-Mn pairs are energetically preferred, although, the situation is more complex because of the change from ferromagnetic to antiferromagnetic order. Regarding Co_2NiGa, a competition of different ordering mechanisms is encountered because both, Ni and Co atoms, prefer a fcc-like crystal structure in their elemental phase. And indeed, this is reflected in the calculations. Inverse and conventional cubic phases are almost degenerate and may thus lead to an inherent preference for disordered arrangements.

This favorable atomic arrangement found for Fe and Co atoms in the cubic inverse structure implies that there is no need for the material to undergo a structural transition to a tetragonally distorted phase.

(iv) When Zn is replacing Ga the strong Fe-Co hybridization in the inverse structure is weakened and the stability of the cubic inverse structure is reduced enhancing the tendency for a second energy minimum at $c/a > 1$. The origin is the competing hybridization of Zn-*s* electrons with Co- and Fe-*d* electrons as already discussed above in the framework of the increasing stability of the $L1_0$ phase for

the Zn-rich alloys. Thus, the almost linear reduction of ΔE_{order} when Zn is substitutionally replacing Ga has the same origin as the enhanced tendency for a martensitic instability in the Zn-based inverse systems.

(v) Again, one has to bear in mind that Zn has one valence electron less than Ga. Because of the strong hybridization of Fe- and Co-*d* with Zn-*s* states, the effect of lower e/a when replacing Ga by Zn, leads to a shift of the whole minority-spin DOS upwards in energy while significant features as, e.g., the peak at -2 eV and the peak at E_F remain almost unchanged for Fe_2CoZn. As a consequence the total magnetic moment increases.

8.3.1.5 Covalent magnetism

It has been mentioned earlier that the simple Stoner-model for the description of itinerant magnetism in the framework of rigid-band theory is not valid for elemental antiferromagnets, certain impurity systems and transition-metal compounds [137]. In these systems, magnetism arises from spin-dependent changes as a result of covalent interactions between the *d* states of neighboring transition-metal atoms. In a first approximation, the DOS of a ferromagnetic element such as Fe in the bcc structure can be obtained be applying the simple rigid-band picture: The non-magnetic DOS is shifted according to the exchange splitting leading to the familiar Stoner-like DOS in which the majority and minority spin DOS are similar in their overall shape, compare Fig. 8.15(a), (b). But such an oversimplified picture is no longer valid in a transition-metal based alloy or intermetallic compound such as FeCo [63]. Here, the magnetization results from a shift in spectral weight to majority-spin states below the Fermi-level and minority-spin states above the E_F as schematically depicted in Fig. 8.15(c), (d). For systems showing covalent magnetism the DOS right at the Fermi level does not play a crucial role in contrast to systems obeying the rigid-band like Stoner-model. In order to get an intuitive idea of the changes occurring under covalent bonding in compounds or alloys consisting of neighboring transition metal atoms a schematic drawing of the molecular orbitals and the corresponding wavefunctions is given in Fig. 8.16. Under covalent interaction of two atoms bonding and anti-bonding hybrid states are formed of the atomic orbitals. In case that the two atomic energy levels are degenerated the spectral weight of atom 1 and atom 2 does not differ in the two hybrid states (upper right panel of Fig. 8.16). But in case that the total number of valence electrons differs for the two interacting atoms the resulting atomic energy levels also differ in energy as represented in the lower left part of Fig. 8.16. By the covalent hybridization of the atomic orbitals two things happen: First, one observes an increased energy separation between the bonding and the anti-bonding hybrid states causing the formation of a transition-metal compound. Second, the spectral weight of majority- and minority-spin states is shifted in both hybrid states which is responsible for covalent magnetism. The atom with the lower energy (atom 2 in Fig. 8.16 which is Co for the Fe-Co-based systems) will have a higher spectral weight in the bonding energy region while the atom with less valence electrons (atom 1 in Fig. 8.16 which is Fe, respectively) will provide a higher spectral weight in the anti-bonding

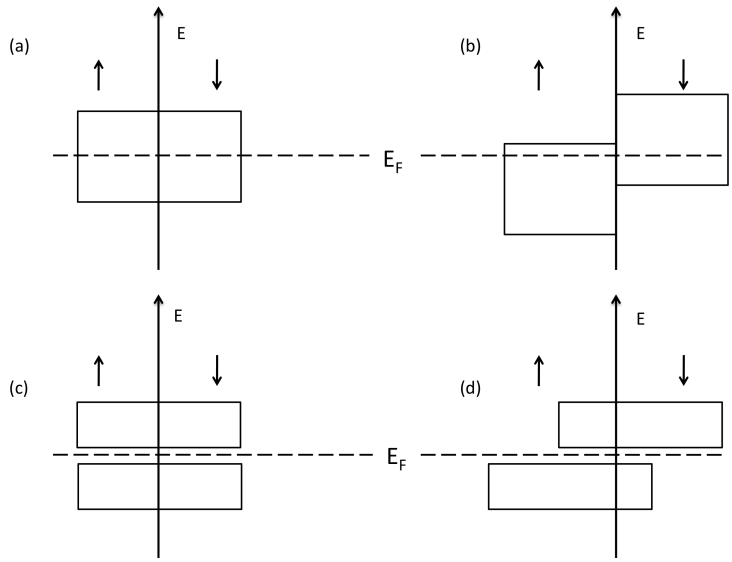

Figure 8.15: Schematic representation of the changes in spin-up and spin-down densities observed in transition metals within (a) the simple Stoner model and (b) the covalent magnetism picture. (a) shows the non-magnetic DOS in the rigid-band like Stoner-model, and (b) when the non-magnetic DOS is shifted upwards in energy for the minority spin channel and downwards in energy for the majority spin channel according to the exchange splitting. (c) The non-magnetic DOS in the covalent magnetism picture. (d) Shift in the spectral weight to majority-spin states below and minority-spin states above the Fermi level. Figure adapted from [137].

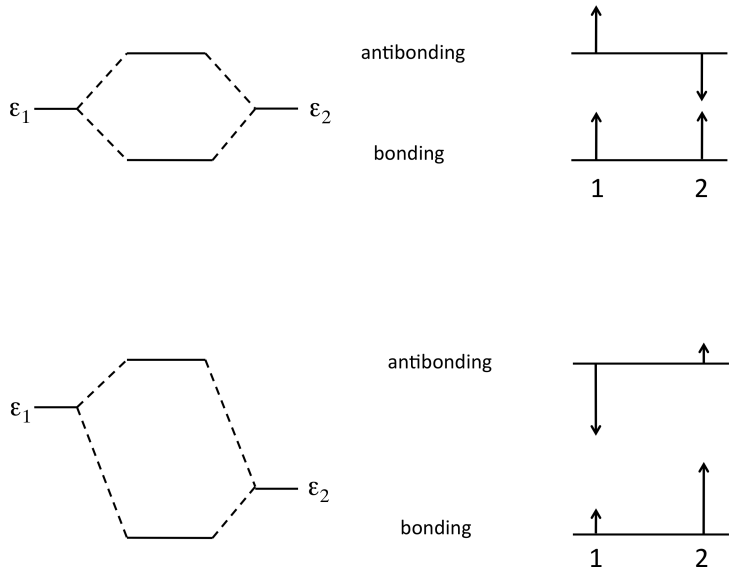

Figure 8.16: Left: Covalent bonds formed of energetically degenerate (upper part) and non-degenerate atomic orbitals with energies $\varepsilon_{1,2}$ (lower part). Right: Corresponding antibonding and bonding wavefunctions. In the lower right part the different length of the arrows indicate the different spectral weight of the atoms 1 and 2. Figure taken from [137].

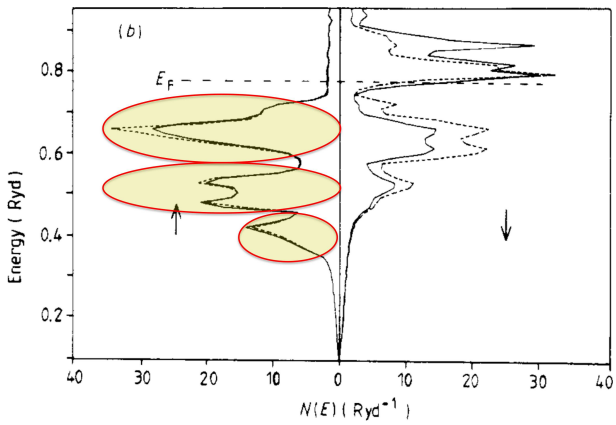

Figure 8.17: Spin- and atom-resolved DOS of FeCo in the CsCl structure as calculated by Schwarz *et al.* Solid lines denote the Fe partial DOS while dashed lines mark the Co partial DOS. The majority-spin DOS of Fe and Co are very similar and also bear strong resemblance to the DOS of bcc Fe (not shown). Clearly visible is the division into bonding, non-bonding and antibonding regions as highlighted by the ellipses. Figure adapted from [63].

hybrid-orbital. This is indicated by the different length of the arrows in the lower right part of Fig. 8.16. Thus, a characteristic feature of covalent magnetism is the spin-dependent hybridization in each spin-channel. Schwarz *et al.* report covalent magnetism in bcc Fe-Co alloys [63]. Their analysis reveals different situations for different spin directions which are a fingerprint of the mechanism of covalent magnetism:

(i) The spin-up DOS is very similar for the two constituent elements Fe and Co, cf. Fig. 8.17. In addition, their majority spin DOS compares well with the DOS of bulk bcc Fe (not shown). According to the molecular orbital picture the covalent interaction between Fe and Co yields bonding and antibonding hybrid-states whose relative weights are approximately the same for Fe and Co majority spins.

(ii) However, for the minority spins the spectral weight of Co is significantly higher than the spectral weight of Fe in the bonding molecular orbital due to the additional valence electron of Co compared to Fe. In the high-lying anti-bonding hybrid-state the Fe spectral weight is dominant, compare Fig. 8.16 and Fig. 8.17. In order to check whether the Fe-Co-based systems also reveal signs of covalent magnetism the calculated DOS of Fe_2CoGa is plotted in direct comparison to a virtual Stoner-like DOS in Figure 8.18.

Figure 8.18(a) shows the actual DOS of $L2_1$ Fe_2CoGa obtained by self-consistent *ab initio* calculation of the majority-spin DOS and (c) shows the minority-spin DOS in comparison with the Stoner-like minority-spin DOS in (b) obtained by a rigid-band shift of the from the spin-down states mirrored spin-up states under maintenance of the total magnetic moment. It is clearly visible in (a) that in the majority-spin DOS Fe and Co have more or less the same spectral weight per atom and do not differ too drastically from each other (note that the DOS of Fe in the figure is twice of that of Co

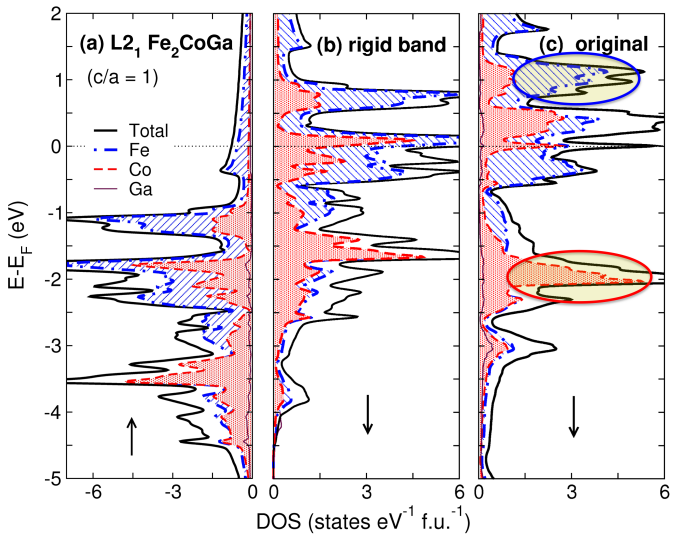

Figure 8.18: (a) Majority-spin density of states of $L2_1$ Fe_2CoGa as obtained by self-consistent *ab initio* calculations showing that the DOS per atom of Fe and Co are very similar. (b) Minority-spin DOS of the rigid band picture of the Stoner model in case of $L2_1$ Fe_2CoGa compared with (c) the actual minority-spin DOS of $L2_1$ Fe_2CoGa. The influence of covalent interaction (hybridization) in the minority-spin channel in case of (c) is clearly different from the rigid-band-like picture in (b) and is the cause of covalent magnetism similar to the case of FeCo discussed in Ref. [63] One has however to keep in mind that the different crystal fields acting on Fe (octahedral) and on Co (tetrahedral) have also influence on the detailed shape of the minority-spin DOS of $L2_1$ Fe_2CoGa.

because there are two Fe per formula unit). This is the first indication of covalent magnetism. The majority-spin DOS also bears resemblance to the majority-spin DOS of bcc Fe and bcc FeCo by showing a clear sub-division of the DOS in the majority-spin channel into bonding, non-bonding, and anti-boding regions (cf. Fig. 8.17), which has been discussed above. Also shown is the different minority-spin DOS of Fe_2CoGa. The strong covalent interaction in both spin channels just as in case of FeCo [63] is clearly visible. As in FeCo, this leads to large additional DOS of Fe at $E > E_F$ and large additional spectral weight of Co at -2 eV in the minority-spin DOS of Fe_2CoGa, compare the highlighted regions in Fig 8.18(c). Similarly, the importance of covalent magnetism is discussed for the inverse structures. Comparing the spin-down DOS of conventional and inverse systems, the impression is that covalent magnetism helps to stabilize the structure of (FeCo)FeGa.

8.3.1.6 Slater Pauling behavior

In order to gain further insight into systematic trends concerning the electronic properties of Heusler alloys, a plot of the total spin moments per formula unit as a function of the total number of valence electrons (Z) is illuminating. Figure 8.19 presents the original full Slater-Pauling (SP) curve for the 3*d* metals and binary alloys [59] which is extended to include also alloys with antiferromagnetic coupling

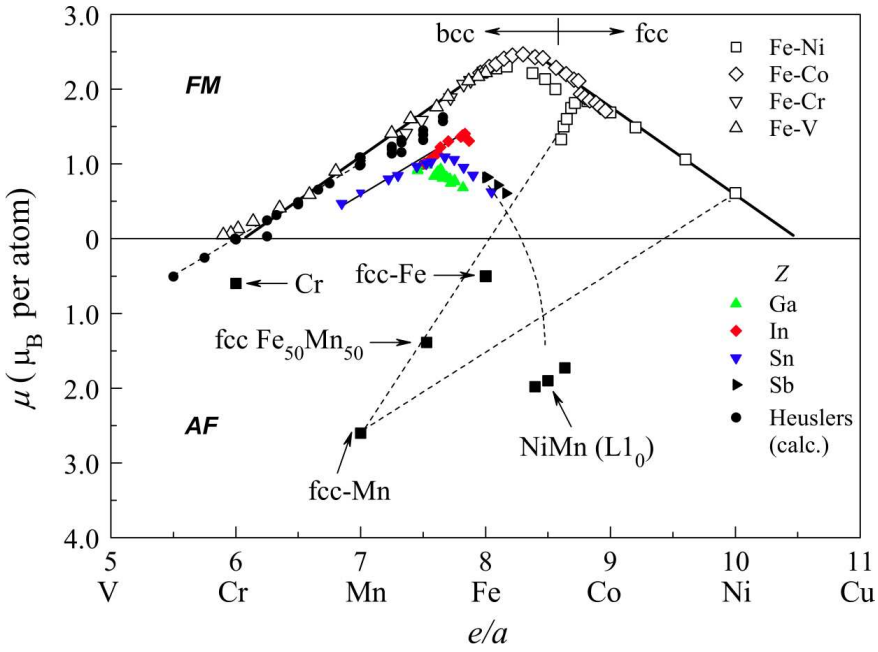

Figure 8.19: The original Slater-Pauling curve (usually plotted for binary ferromagnets) is here extended to include also antiferromagnetic exchange and the magnetism of Ni-Mn-Z Heusler alloys. Emphasized by thick lines is the linear dependence of the total magnetic moments (in μ_B per atom) on the valence electron concentration per atom e/a for 3*d* and Heusler alloys. The filled circles mark the calculated values. Filled squares are specific AF elemente and alloys. Open symbols denote the moments of the 3*d* metals and alloys while filled small symbols represent the moments of Ni-Mn-Z Heusler alloys. Figure adapted from [30].

and the Ni-Mn-Z Heusler alloys. For the pure 3*d* metals and binary alloys the transition from bcc to fcc crystal structure occurs at about 8.5 e/a. For better statistics and in order to establish the trends in the change of the total moment as a function of Z a few more Fe-Co-based systems have been calculated with different Z elements (Z = Ga, Zn, Ag, Au, and Cu) and various off-stoichiometric compositions. The equilibrium values are listed in Table 8.4.

In Fig. 8.20 an enlarged part of the original SP curve is given in which the calculated spin moments for the Fe-Co-Z systems (highlighted in red for the Ga-based and orange for the Zn-based compounds) are compared with results for the half-metallic Heusler alloys found in literature [134] and other *ab initio* data for Ni-Mn-Z (Z = Ga, Al, In, Ge, Si) [132], Co-Ni-Ga, Ni-Co-Z (Z = Al, Ga, Ge, Sb) [132], and $Fe_{1-x}Co_x$ [63]. A summary of the equilibrium parameters of all systems calculated in the framework of this thesis is listed in Table 10.1 in the summary section 10. The reversal from increasing to decreasing inclination occurring in the results for the binary Fe-Co systems can be explained as a result of the crossover from weak to strong ferromagnetism. In zeroth-order the slope of the magnetic moments as function of Z can be approximated by two straight lines. The linear increasing part

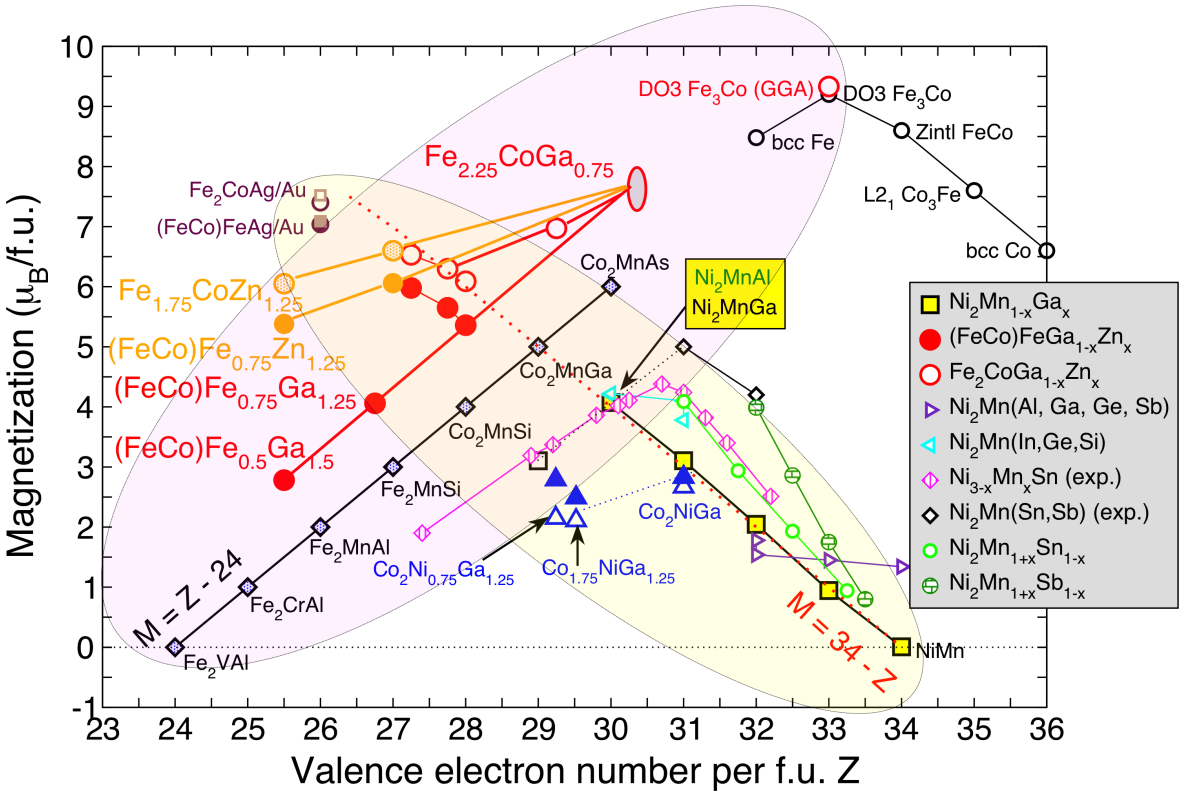

Figure 8.20: Calculated spin moments per formula unit (f.u.) (highlighted in red for Ga-based and in orange for Zn-based alloys) for the cubic conventional (open symbols) and the cubic inverse structures (filled symbols) as a function of the total number of valence electrons per f.u. Z in comparison to data found in literature. Please, note that Z is always given for the Heusler f.u., thus Z of Co in bcc structure is here $4*9=36$. The half-metallic Heusler alloys (open, black diamonds) and the Fe-Co-Ga-Zn systems follow linear increasing functions indicating a fixed number of minority-spin states or reflecting an increasing percentage of Fe atoms in the compound, respectively. The linear decreasing slopes of the Ni-Mn-(Ga, Sn, Sb) systems originate from a constant number of majority-spins or from increasing antiferromagnetic tendencies with increasing Mn concentration. The data of the stoichiometric Fe_2Co(Ga, Zn) systems are perfectly in line with the results for Ni-Mn-Ga. This, and the overall linear character of the spin moments imply that despite hybridization effects the magnetic moments possess localized character.

follows the relation

$$M = Z - 2N_{\downarrow} \tag{8.1}$$

where $N_{\downarrow} = 11.72$ is the total number of spin-down electrons per unit cell. Please, keep in mind that for a better comparison Z is always given for the Heusler cell with 4 atoms. This equation can be applied to magnetic weak systems like Fe in which the minority-spin density of states is fixed in a pronounced dip right at the Fermi energy. This pronounced dip is characteristic for the DOS of bcc

Table 8.4: Calculated equilibrium parameters of stoichiometric Fe-Co-(Ag, Au, and Cu) Heusler alloys and various off-stoichiometric Fe-Co-(Ga, Zn) systems in the conventional X_2YZ and in the inverse (XY)XZ Heusler structure. Parameters as in Tab. 7.1. In addition the valence electron concentration e/a and the stable structure (St) at $T = 0$ K (absolute energy minimum) are given. 'unst' refers to an unstable structure.

System	e/a	St	a_0 (Å)	c/a		M (μ_B/f.u.)	$\Delta E_{c/a}$
Conventional							
Fe_2CoAg	6.5	unst	5.996	0.88	1.38	7.10	62
Fe_2CoAu	6.5	unst	6.02	0.85	1.40	7.13	87
Fe_2CoCu	6.5	unst	5.742	0.90	1.35	6.90	53
$Fe_{1.75}CoZn_{1.25}$	6.375	unst	5.806	0.94	1.38	5.86	33
$Fe_{2.25}CoGa0.75$	6.731	cubic	5.760	1.00	/	6.97	/
Fe_3Co	6.8125	cubic	5.748	1.00	/	5.58	/
Inverse							
(FeCo)FeAg	6.5	unst	5.970	0.92	1.42	7.04	32
(FeCo)FeAu	6.5	unst	5.986	0.90	1.42	7.16	63
(FeCo)FeCu	6.5	unst	5.718	0.94	1.46	6.83	26
$(FeCo)Fe_{0.75}Zn_{1.25}$	6.375	unst	5.776	0.98	1.40	5.71	15
$(FeCo)Fe_{0.75}Ga_{1.25}$	6.6875	cubic	5.745	1.0	/	4.06	/
$(FeCo)Fe_{0.5}Ga_{1.5}$	6.375	cubic	5.748	1.0	/	2.78	/

systems. Thus, additional electrons occupy the majority-spin channel and lead to an increase in the total magnetization. This situation applies accordingly to half-metallic systems which possesses a true gap in the minority spin DOS at E_F.

The linear decreasing inclination encountered for Co concentrations larger than 25% suggest strong ferromagnetism and can be fitted by

$$M = 2N^{\uparrow} - Z \, . \tag{8.2}$$

For strong ferromagnets such as FeCo alloys the majority-spin *d*-states are completely occupied leading to 5 *d* spin-up electrons per atom. The number of non-*d* spin up electrons is fixed to 0.3 per atom by a dip right at E_F in the majority non-*d* spin densities of states [138–140]. This results in a total number of majority-spin electrons of $N\uparrow = 4 * 5.3$ [63, 141]. For the half-metallic Heusler alloys the linear increasing magnetic moments with increasing valence electron number (Z) follow the simple rule $M = Z - 24$ which originates from the filling of the majority-spin channel under a constant number of minority-spin states due to the pinning of the Fermi level in the half-metallic minority-spin gap. The origin of the characteristic gap in the minority-spin channel of the half-metallic Heusler compound Co_2MnGe is discussed briefly in [58] and in the appendix 11.1. For a deeper understanding of the origin of the linear function $M = Z - 24$ the analysis of the different crystal fields acting on the different atoms in the Heusler compound is instructive. Thus, I refer to the appendix where a short overview of the crystal fields and the resulting hybridization scenario is discussed in section 11.1. A linear decreasing slope, as found, e.g., for the Ni-Mn_{1+x}(Ga, In, Sn, Sn)$_{1-x}$ systems, hints towards a fixed number of majority-spins (and corresponding filling of the minority-spin channel) or

an increasing amount of antiferromagnetic tendencies with increasing Mn content in the Mn-based compounds, respectively. The results for the $Ni_2Mn_{1-x}Ga_x$ meet the simple function $M = 34 - Z$ which hints towards $N^{\uparrow} = 17$ occupied majority-spin states per unit cell if the hybridization picture drawn by Galanakis *et al.* is applied.

For the Fe-Co-based Heusler alloys investigated in this work the increasing slope is explained by the increasing percentage of ferromagnetic Fe replacing diamagnetic Ga in the compound. Extraordinarily large magnetic moments can be found for the Fe_2CoZ Heusler alloys (up to $M = 7.5\mu_B$/ f.u. for Fe_2CoAu at $c/a = 1$) for which the Fe moment is significantly higher than in elemental bcc bulk Fe ($M = 2.14\mu_B$/ atom). Variation of the Z element from Ga over Zn to Cu, Ag, and Au (decreasing Z) steadily enhances the total magnetic moment. Thus, one may suggest that the Z-*d* electrons hybridize with the X and Y-*d* electrons and therefore the spin moments localized on Fe and Co atoms are enhanced. This scenario already starts with Zn as Z element showing that the hybridization of Zn-*s* electrons with X- and Y-*d* electrons leads to a depletion of the minority spin channel as discussed in Section 8.3.1.4. Extrapolation of the linear increasing functions with slightly different slopes which are found for the inverse and conventional Fe_2CoGa and Fe_2CoZn systems, coincide at a valence electron number of approximately $Z = 30.5$ which corresponds to a composition of $Fe_{2.5}CoGa_{0.5}$. This nicely reflects the fact that a distinction in between inverse and conventional Heusler structure is no longer meaningful for the case that the Z element has a concentration of less that 12.5% given that the X element has a concentration of 62.5% or more and the Y element has a constant concentration of 25%.

The *ab initio* results for Ni-Mn-(Ga, Sn, Sb) obey linear functions with different slopes which emerge from the fact that all Ni-Mn-Z curves finally coincide at antiferromagnetic NiMn. Thus, *sp*-electrons of the Z element hybridize with *d*-electrons of X and Y and cause a reduction of the total moment with increasing Z by filling of the minority-spin states. The results for Ni_2Co(Ga, Ge, Sb) agree with this observation as the spin moments slightly decrease with increasing Z as in the case of of Ni_2Mn(Ga, Ge, Sb). Interestingly, the investigated stoichiometric Fe_2CoZ alloys are perfectly in line with the Ni-Mn-Ga results indicating that the depletion of the minority-spin channel with decreasing valence electron number takes place independently of the group of Heusler alloys considered.

In general, a set of linear increasing and linear decreasing functions is found which connect the magnetic spin moments of various families of Heusler alloys. This implies that despite hybridization effects the overall character of the magnetic moments in Heusler alloys is of localized nature.

8.3.1.7 Inverse Martensites

The stability of the cubic inverse structures and the absence of a tetragonally distorted phase in $(FeCo)FeGa_{1-x}Zn_x$ systems make these systems inadequate for magnetic shape-memory purposes. To the best of my knowledge, up to now only very FSMA exist which shows a martensitic transformation in the inverse structure. The only prominent example is (MnNi)MnGa which exhibits a martensitic transformation around room temperature and shows a two-way shape memory behavior with strain of

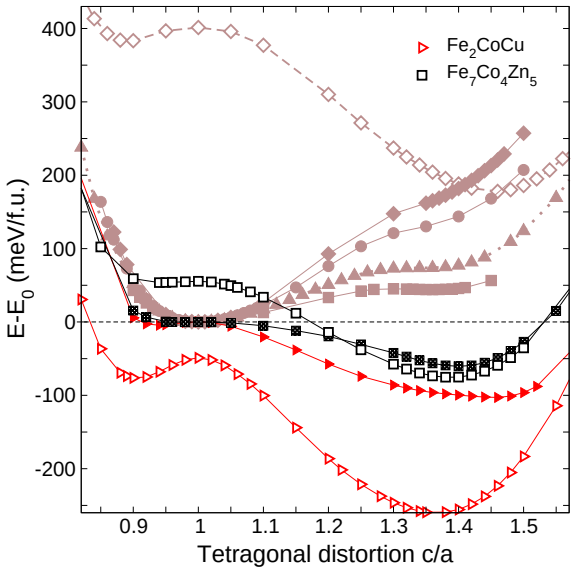

Figure 8.21: Total energy of a few previously unconsidered alloys relative to the energy of the respective cubic inverse phase. As in Fig. 8.7, open and filled symbols distinguish between conventional and inverse structures, respectively. For comparison the corresponding curves of all alloys discussed above in the inverse structure and $L2_1$ Fe_2CoGa (from Fig. 8.7) are shown by grey symbols. In addition, results for two representative alloys, $Fe_7Co_4Zn_5$ (black squares) and Fe_2CoCu (red, rightward triangles) are also shown. For the latter two systems, clear martensitic tendencies are observed.

1.7% in the single crystal [142–145]. For the (FeCo)FeZn system already pronounced tendencies for a second energy minimum at $c/a > 1$ are found which offers the possibility of a martensitic transformation. Therefore, calculations for Fe-Co-based systems with slightly different composition or different Z-components are performed, in order to force these systems to develop a martensitic instability (cf. Fig. 8.21 and Table 8.4). I succeeded by using rather unusual Z-elements like Cu, Ag and Au (results for Fe_2CoAg or Fe_2CoAu are not shown because qualitatively the same behavior is found) or by a further enhancement of the Zn content in the Fe-Co-Zn compound ($Fe_{1.75}CoZn_{1.25}$). Remarkable is the occurrence of a local energy minimum at $c/a < 1$ as soon as an absolute energy minimum at $c/a > 1$ could be induced. This is an important observation because the modulated phases which are relevant for the magnetic shape memory effect are found at c/a ratios smaller than one (cf. chapter 3.4.2). Although all of these systems possess a positive mixing energy I believe that this study shows that it is possible to find an inverse martensite with high Curie and martensite transformation temperatures relevant for magnetic shape memory purposes.

8.3.2 Conclusion

The Curie temperatures of all investigated systems, Fe_2CoGa, $Fe_2CoGa_{0.75}Zn_{0.25}$, $Fe_2CoGa_{0.25}Zn_{0.75}$ and Fe_2CoZn, are remarkably high compared with prototype Ni_2MnGa FSMA ($T_C = 365$ K). The

successive substitution of Ga by Zn in the quaternary system $Fe_2CoGa_{1-x}Zn_x$ helps to reduce the energetic preference of the inverse cubic Heusler structure in favor of the tetragonally distorted conventional structure and increases T_C. However, this is achieved at the expense of structural stability. In $Fe_2CoZn_{0.75}Ga_{0.25}$ the absolute energy minima of cubic inverse and conventional tetragonal Heusler structures are almost degenerate which would support coexisting inverse and conventional structures or even completely disordered alloys. Therefore, I expect that $Fe_2CoZn_{1-x}Ga_x$ alloys are promising candidates which show the magnetic shape-memory effect.

This competition of conventional and inverse Heusler structures is rather intriguing. I found that one important reason for the energetic preference of the inverse structures at $c/a = 1$ with respect to the conventional structure at the same c/a in Ga-rich $Fe_2CoZn_{1-x}Ga_x$ alloys, is the different crystal environment of Fe. In the inverse phase Fe_C is in a bcc-like atomic neighborhood with Fe_A and Co as nearest neighbors. In the unfavorable conventional phase, the hybridization of Fe and Co is partially suppressed by the different symmetry of Fe- and Co-*d* orbitals (e_u, e_g and t_{1u}, t_{2g}) which results from the effect of different crystal fields acting on the octahedrally coordinated Fe and tetrahedrally coordinated Co. On the other hand, aspects of covalent magnetism give rise to enhanced hybridization effects in both spin channels of Fe_2CoGa as discussed above.

One important statement that emerges is that the X atoms which prefer a fcc close-packed crystal structure will stabilize the conventional X_2YZ Heusler structure as Ni in Ni_2MnGa or Co in Co_2FeGa. This is in contrast to X atoms with an elemental bcc-crystal structure which is responsible for the instability of the conventional structure and stabilizes the inverse Heusler structure as Fe in (FeCo)FeGa and (FeCo)FeSi.

By the use of rather extraordinarily Z-elements like Cu, Ag, or Au or by further enhancement of the Zn content a martensitic instability could also be induced in the inverse Fe-Co-based Heusler alloys. Thus, although the latter alloys have a positive mixing energy one may tentatively conclude that it is possible to find exceptional FSMAs with high Curie temperature relevant for the magnetic shape memory effect which show the martensitic transformation in the inverse structure.

With respect to magnetism, I compare the behavior of Fe_2CoGa and (FeCo)FeGa with the magnetic structure of another Heusler or Zintl phase, Fe_3Co or Fe_2FeCo, which also has two inequivalent Fe atoms and shows spin-dependent hybridization of Fe-Co-*d* states (covalent magnetism).

Slater Pauling behavior could be established for all investigated Fe-Co-based Heusler alloys and is confirmed by other *ab initio* and experimental data from literature. The linear increasing or decreasing slope of the spin moments of all Heusler alloys considered implies that despite hybridization effects the overall character of the magnetic moments is of localized nature.

9 New FSMA Ni-Co-Fe-Ga(Zn)?

9.1 Introduction

Up to now the investigations revealed (amongst others results) that Fe and Co enhance the Curie temperatures, Ni stabilizes a martensitic energy landscape, and Zn has beneficial impact on the magnetic properties of the new alloys. But none of the systems studied so far is perfectly suited for a new FSMA alloy. Thus, the idea was to combine the beneficial properties of Fe, Co, and Ni (as discussed in the previous chapters for Ni-Co-Ga(Zn) and Fe-Co-Ga(Zn) Heusler alloys) in an alloy with the same or a similar valence electron concentration as Ni_2MnGa (e/a = 7.5). In this section I will present the results of first-principles calculations of stoichiometric (NiCo)FeZ, (FeNi)CoZ, and (FeCo)NiZ Heusler alloys with Z = Ga and Zn in the (X1X2)YZ structure, cf. Fig. 3.5. In quaternary Heusler alloys the differentiation between conventional and inverse structure becomes obsolete. Ni-Fe-Ga is one of the recently suggested new FSMA's which is characterized by good ductility, wide range of transformation temperatures and high magnetocrystalline anisotropy energy [146–148]. However, T_C^A and T_M, cannot be kept simultaneously above room temperature (T_M = 150 K for stoichiometric Ni_2FeGa [46]). The addition of Co strongly influences both, the martensite temperature T_M and the Curie temperature T_C^A. For example, substitution of Ni by Co in $Ni_{54-x}Fe_{19}Co_xGa_{27}$ causes an increase of T_C^A but decreases T_M. Whereas the replacement of Fe by Co in $Ni_{51}Fe_{22-x}Co_xGa_{27}$ increases T_C^A and T_M [149]. For $Ni_{52}Fe_{17}Ga_{27}Co_4$ the addition of small amounts of Co replacing Fe increases T_C while T_M could be kept above room temperature as recently reported by J. Liu *et al.* [150]. Likewise for the Ni-Al-Fe system, where Co was found to be an effective element by which the martensite and the magnetic transition temperature can be controlled [39]. But still, in order to explore the MSME at temperatures significantly higher than room temperature, further improvement of the material properties is required.

9.2 Results and discussion

In quaternary (X1X2)YZ Heusler alloys the knowledge of the structural ordering tendencies with three transition metals Fe, Co, and Ni on the X1, X2, and Y sites in the neighborhood of Ga (Zn) on the Z-site is of fundamental importance. There are three relevant occupation possibilities under the constraint that the concentration of the Z-element is kept fixed to 25%: (NiCo)FeZ, (FeNi)CoZ, and (FeCo)NiZ. The results of the calculated equilibrium parameters for all three orderings are summa-

Table 9.1: Calculated equilibrium parameters of tetragonally distorted ordered (NiCo)FeZ, (FeCo)NiZ, and (FeNi)CoZ with Z = Ga, Zn and disordered Ni-Co-Fe-Ga. Valence electron concentration, e/a, equilibrium lattice constant a_0 (for $c/a = 1$), local and absolute energy minima at different c/a-ratios, and Curie temperature T_C in K for the case $c/a > 1$, energy difference between the energy minima at $c/a = 1$ and $c/a > 1$, $\Delta E_{c/a}$, and mixing energy. All energies are in meV/atom. "/" means not calculated.

System	e/a	a_0 (Å)	c/a		T_C	$\Delta E_{c/a}$	E_{mix}
(NiCo)FeGa	7.5	5.757	0.95	1.25	590	19	-890
(FeCo)NiGa	7.5	5.716	0.88	1.51	530	100	-718
(FeNi)CoGa	7.5	5.741	1.01	1.42	365	32	-614
Disorder	7.5	5.766	0.85	1.42	/	25	/
(NiCo)FeZn	7.25	5.743	1.0		733		-330
(FeCo)NiZn	7.25	5.741	0.85	1.55	523	126	-118
(FeNi)CoZn	7.25	5.743	0.97	1.41	600	42	-97

rized in Table 9.1. The results of the investigation of the Ni-Co-Fe-Ga(Zn) alloys have been published in [25].

The variation of the total energy as a function of the tetragonal distortion for the different options of lattice occupation is shown in Fig. 9.1.

Clearly, energetically favored are the occupation possibilities with Fe and Ga (or Zn) on the same cubic sublattice as for (NiCo)FeGa and (NiCo)FeZn. The other ordered structures have energies more than 50 meV/atom higher. The high stability of the (NiCo)FeZ ordering type in which Fe/Co and Fe/Ni become nearest neighbors may be a result of excellent miscibility of Fe with Co/Ni [151]. The hierarchy between the three types of ordering does not change when substituting Zn for Ga. The energy profiles for the Ga-based and for the Zn-based alloys are martensitic and qualitatively the same except for (NiCo)FeZn: Here, the energy landscape does not show a second energy minimum and thus will not transform martensitically. This differs from my observation regarding the $Fe_2CoGa_{1-x}Zn_x$ alloys discussed in the previous chapter 8.3 for which Zn addition could significantly enhance the tendency for a second energy minimum in the inverse structures and even induce a martensitic energy profile in the $Fe_7Co_4Zn_5$ system, cf. section 8.3.1.7 in chapter 8.3. On the other hand, the observation of martensitic energy profiles for all three ordering types in the Ni-Co-Fe-Ga alloys may be related to the results presented in chapter 7.2.1 in which I found that for the Ni_2CoGa(Zn) alloys the conventional as well as the inverse Heusler structure are martensitic. Thus, I may tentatively conclude that alloys containing Ni have an enhanced tendency for a martensitic energy profile. On the other hand, this can also be related to the fact that Ni has the largest number of valence electrons compared to Mn, Fe, and Co and thus simply enhances e/a. Heusler alloys with a valence electron concentration e/a larger than 7.25 are most often found to possess a martensitic binding curve as the comprehensive study of Gilleßen and Dronskowski confirms [22, 70]. The energy difference $\Delta E_{c/a}$ of energetically favorable ordered (NiCo)FeGa amounts to 19 meV/atom which is about three times larger than in

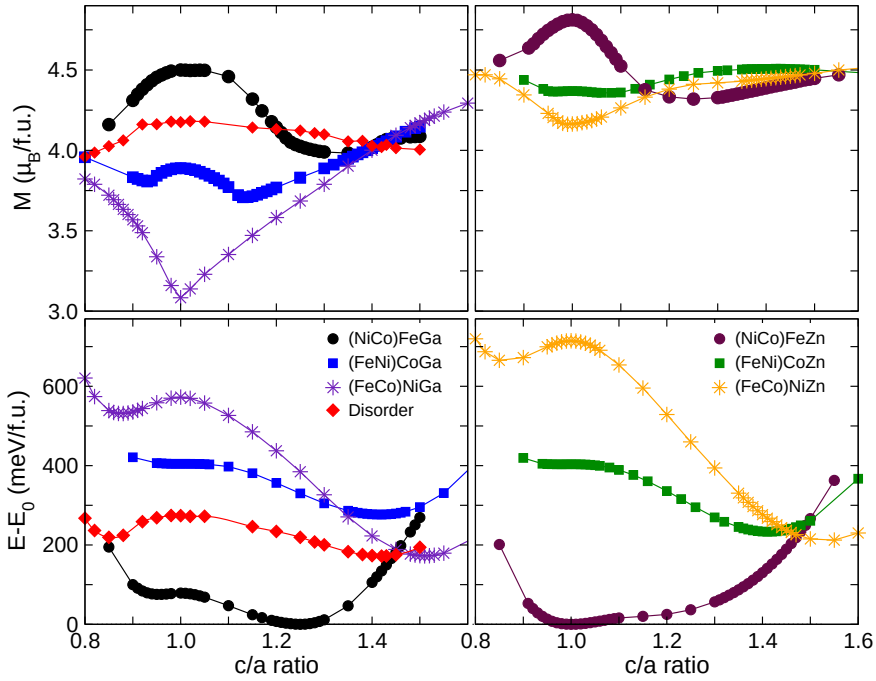

Figure 9.1: Total energy of (NiCo)FeZ (circles), (FeNi)CoZ (squares), and (FeCo)NiZ (stars) with Z = Ga (left) and Z = Zn (right) as a function of the tetragonal distortion (c/a) and the corresponding magnetic moments M in μ_B/f.u. The disordered Ni-Co-Fe-Ga alloy is marked by red diamonds. All energies are relative to the energy of tetragonal (NiCo)FeZ. The ordering (NiCo)FeGa and (NiCo)FeZn are energetically favored, from which follows that half of the Fe atoms preferentially share the cubic sublattice (Y-site) with Ga (or Zn) while Ni and Co occupy the X-sites, cf. . Fig. 3.5.

Ni_2MnGa where $\Delta E_{c/a}$ = 6 meV/atom. Therefore, a significantly higher martensite temperature can be expected of the order of $T_M \gtrsim 650$ K. In order to justify the assumption that the volume of the cubic phase does not significantly change under tetragonal distortion, I have calculated for the promising (NiCo)FeGa system the energy surface as a function of atomic volume and tetragonal distortion, cf. Fig. 9.2. The contour plot of the total energy E(c/a, V) of ordered (NiCo)FeGa reveals that the atomic volume of the local and the absolute energy minimum at $c/a = 0.95$ and $c/a = 1.25$, respectively, do not differ significantly (about 1%). The analysis of the contour plot allows an estimation of the error made when using the atomic volume of the cubic phase along the whole Bain path. If one makes an intersection in the contour plot parallel to the x-axis at constant volume of the cubic phase, one observes that at the absolute energy minimum at $c/a = 1.25$ the equilibrium volume and the volume of the cubic phase only differ by half of two neighboring contour lines. Two neighboring contour lines differ in energy by 4 meV/atom, thus, the error amounts to approximately 2 meV/atom and is almost negligible. With this, the assumption of a constant volume independently of the c/a ratio is verified. For martensitic materials showing a thermoelastic transition the exact matching of the lattice constant of austenite and martensite phases is an important requirement. Otherwise, the

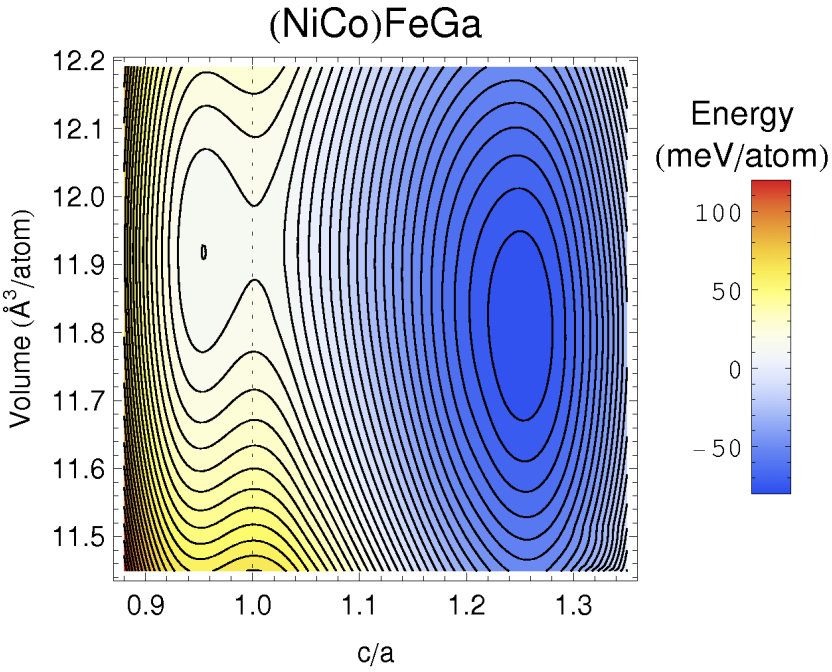

Figure 9.2: Contour plot of the total energy E(c/a, V) of ordered (NiCo)FeGa as a function of atomic volume V and tetragonal distortion c/a. The difference in energy between two contour lines amounts to 4 meV/atom. The absolute energy minimum is located at V = 11.81 Å^3/atom and $c/a = 1.25$. A further minimum is found at V = 11.91 Å^3/atom and $c/a =$ 0.95. The atomic volume between the two energy minima differs by only 1% which justifies the assumption of a constant volume under tetragonal distortion.

kinetics of the martensitic transformation is disturbed because the mismatch of the atomic volumes in cubic and martensite phases induces dislocations and other defects. In order to account for the potential occurrence of a completely disordered alloy, I have performed a 128 atom supercell calculation with a random distribution of Fe, Co, Ni, and Ga on the crystal lattice. Disorder is especially interesting because during experiment thermal ordering is often suppressed due to rapid cooling. First experimental observations report a disordered bcc phase (A2) [152, 153] which is in contradiction to my first-principles calculations. One possible and very likely explanation is a decomposition of the quaternary (NiCo)FeGa alloy into two (or more) bcc phases which are more stable. To prove this assumption I have checked the mixing energies of various similar Heusler structures which are stable in the bcc phase. And indeed, the averaged sum of the mixing energies of $L2_1$ Co_2FeGa and austenitic Ni_2FeGa (T_M = 150 K) is lower than the mixing energy of (NiCo)FeGa: Co_2FeGa has a mixing energy E_{mix} = -958 eV/atom and for Ni_2FeGa I found E_{mix} = -870 eV/atom. Thus, in average, E_{mix} = -914 eV/atom which is lower than E_{mix} = -890 eV/atom for (NiCo)FeGa. This shows that a decomposition of quaternary (NiCo)FeGa into ternary Co_2FeGa and Ni_2FeGa has presumably occurred during the fabrication of the sample. Two possibilities to avoid segregation and decomposition are annealing followed by rapid quenching or epitaxial growth. Experimental work along these lines is in progress.

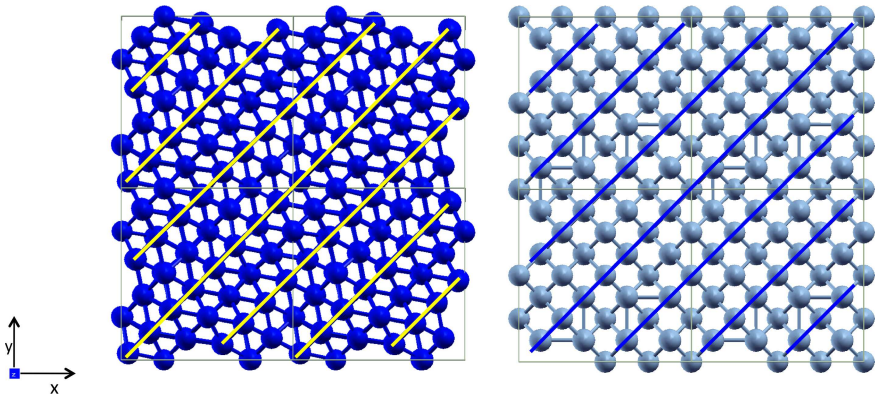

Figure 9.3: Top view on the x/y-plane of the relaxed crystal structure of the 128 atom supercell of disordered Ni-Co-Fe-Ga at the local energy minimum at $c/a = 0.85$ on the left and of Mn-excess $Ni_{64}Mn_{38}Ga_{26}$ at $c/a = 0.94$ on the right. For a better visualization all atoms are colored in dark blue for Ni-Co-Fe-Ga and light blue for $Ni_{64}Mn_{38}Ga_{26}$. For Ni-Co-Fe-Ga a fine, two-fold modulated twin structure has emerged during relaxation as indicated by the solid yellow lines. Thus, the energy for the creation of twin boundaries must be extraordinarily low. The absolute energy minimum at $c/a = \sqrt{2}$ corresponds to a cubic fcc structure. In contrast, the technologically relevant $Ni_{64}Mn_{38}Ga_{26}$ system does not show any sign of a modulation.

The position in energy of the disordered alloy compared to the ordered structures reflects the mixture of the three different ordering types. A comparatively flat energy profile with two minima is observed (cf. Fig. 9.1). The smooth absolute energy minimum occurs at $c/a = 1.42$ which corresponds to a cubic fcc structure (A1).

At these large tetragonal distortions the disordered phase is the energetically preferred phase, almost degenerated with the structural order of (FeCo)NiGa. A sudden decrease in energy occurs around $c/a \sim 0.92$ and a local energy minimum is found at $c/a = 0.85$. It is rather steep compared to the absolute energy minimum. A closer look onto the fully relaxed atomic positions at this energy minimum reveals that a two-fold twin structure has emerged (cf. Fig. 9.3). In the x/y plane of the 128 atom simulation cell already two twin boundaries can be traced from which one can conclude that the energy needed to create twin boundaries in disordered Ni-Co-Fe-Ga has to be extraordinarily low. If the creation energy of twin boundaries is low and results into a high density of twin boundaries in the material and if, in addition, these twin boundaries are also highly mobile, one important prerequisite for new smart materials which are intended to be used for magnetically induced reorientation actuation mechanism is fulfilled [18]. Thus, Ni-Co-Fe-Ga offers a lot of interesting features for future FSMA applications. In order to be able to draw a direct comparison to the technologically relevant Mn-excess $Ni_{50}Mn_{30}Ga_{20}$ sample ($Ni_2Mn_{1.2}Ga_{0.8}$), I have performed a corresponding relaxation calculation for the 128 atom $Ni_{64}Mn_{38}Ga_{26}$ system ($Ni_2Mn_{1.1875}Ga_{0.8125}$). Here, the excess Mn atoms replace Ga at randomly chosen sites of the Ga-sublattice. Interestingly, the prototype FSMA Ni-Mn-

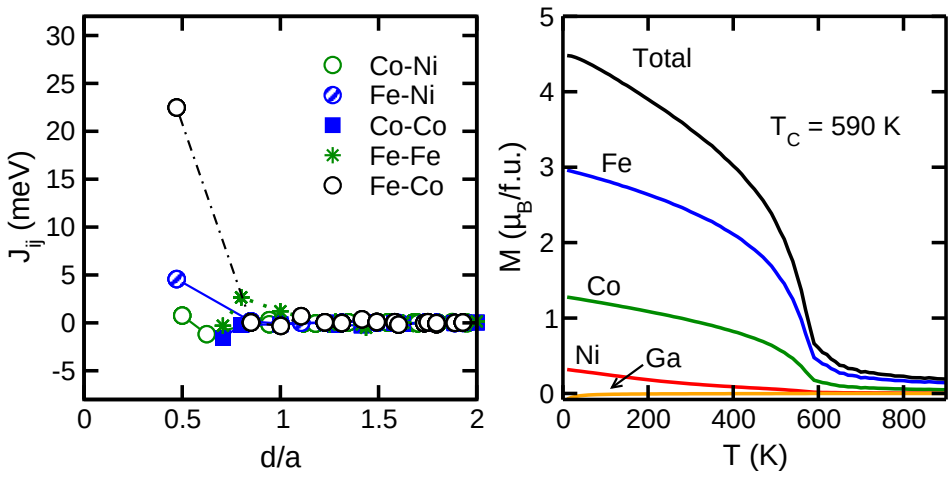

Figure 9.4: Magnetic exchange coupling constants J_{ij} of (NiCo)FeGa for $c/a = 1.25$ as a function of the distance d in units of the lattice constant a of the tetragonal phase (left) and variation of the individual magnetic moments as a function of temperature obtained from the corresponding Monte Carlo simulations (right). Parameter labeling as in Fig. 7.3. In addition, the Fe-Ni interaction is labeled by blue dashed circles. The strongest ferromagnetic coupling is obtained for nearest neighbor Fe and Co spins. Right: Results of Monte Carlo simulation for the magnetic moments as a function of temperature using the coupling constants shown in the left panel.

Ga does not show a corresponding modulation at the tetragonal distortion $c/a = 0.94$ after relaxation, cf. Fig. 9.3. However, this must be checked further by using modulated structures as initial guess in calculations with a high number of k-points.

The magnetic moments emphasize the energetic order observed in the energy profiles at $c/a = 1$. The binding curve with the lowest energy has the highest magnetic moment from which it is clear that magnetism has a stabilizing effect. In accordance to the observations made in the previous chapters, the replacement of Ga by Zn leads to an enhancement of the magnetic moments.

The mixing energies are negative for the Ga-based as well as for the Zn-based compounds, cf. Table 9.1. However, their absolute values are reduced for the Ni-Co-Fe-Zn systems. The mixing energy increases with decreasing structural stability of the ordered alloys in agreement with the sequence of the absolute energy minima.

The magnetic coupling constants of (NiCo)FeGa show ferromagnetic coupling which is most pronounced for the nearest neighbor Fe-Co interactions, see Fig. 9.4. The resulting Curie temperature is comparatively high of the order 590 K. The phonon dispersions of (NiCo)FeGa and of Ni_2MnGa have been evaluated by Mario Siewert by means of supercell calculations using 108 atoms. The atoms in the unit cell were individually displaced from their ideal positions and the resulting forces, which are needed to achieve the dynamical matrix, were calculated. In Fig. 9.2 the calculated and experimental lattice dynamics of Ni_2MnGa are compared with the calculated dispersions of isoelectronic

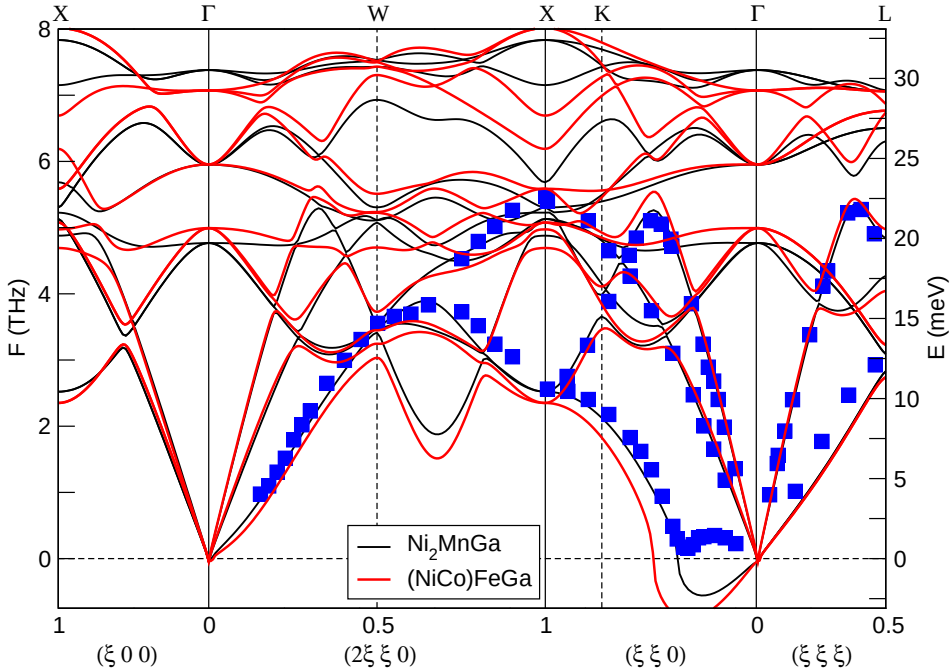

Figure 9.5: Calculated phonon dispersions of ordered (NiCo)FeGa (red lines) and Ni_2MnGa (black lines) by Siewert *et al.* [110] in comparison to experimental frequencies for Ni_2MnGa (squares) [154]. The overall character of the lattice dynamics of (NiCo)FeGa bears strong resemblance to Ni_2MnGa. Phonon softening is observed regarding the TA_2 mode in [110] direction for both systems.

(NiCo)FeGa. First it is important to point out, that excellent agreement between the experimental [154] and the theoretical phonon dispersions of Ni_2MnGa can be observed. Comparing the two calculated phonon dispersions of Ni_2MnGa and (NiCo)FeGa, strong resemblance is found throughout the whole spectrum. Noteworthy differences only occur in the [110]-TA_2 branch which is found at slightly lower frequencies for the (NiCo)FeGa compound. For both alloys a softening of the [110]-TA_2 branch is observed, cf. chapter 3.4, which is a strong indication for a modulated martensitic phase characterized by the corresponding q-vector in [110] direction for which the softening occurs [46].

9.3 Conclusion

The first-principles calculations of ordered (NiCo)FeZ, (FeNi)CoZ, (FeCo)NiZ alloys with Z = Ga, Zn reveals that the ordered (NiCo)FeZ systems are clearly energetically favored from which follows that Fe preferentially occupies the same cubic sublattice as Ga (Zn) causing Fe/Co and Fe/Ni to become nearest neighbors. Thus, the excellent miscibility of Fe with Co/ Ni may be one reason for the observed structural ordering tendencies. According to the $T = 0$ K calculation, the ordered (NiCo)FeGa system with a fcc crystal structure is the most stable and most interesting system. It has the same

valence electron concentration as Ni_2MnGa (e/a = 7.5), its energy profile is martensitic, its Curie temperature is significantly above room temperature (T_C = 590K) and the estimated martensite temperature is high of the order of $T_M \gtrsim 600$ K. In addition, the phonon dispersion relation shows a softening of the TA_2 mode in [110] direction as found for Ni_2MnGa indicating a martensitic instability. The low TA_2 [110] branch is present in all bcc martensitic materials and is accompanied by a micromodulated structure. A hint towards a modulated structure may be the occurrence of a 2-fold modulated twin structure found for the local energy minimum (at $c/a = 0.85$) in the relaxed disordered NiCoFeGa system which was monitored by a 128 atom supercell calculation. In contradiction to the first-principles results, first experiments report a disordered cubic bcc structure (A2). This is presumably the result of a decomposition of the quaternary Ni-Co-Fe-Ga alloy into two (or more) compounds which are stable in the bcc phase. Our mixing energy analysis suggests $L2_1$ Co_2FeGa and austenitic Ni_2FeGa as possible candidates for stable bcc phases. Segregation and decomposition could be avoided using annealing followed by quench hardening or epitaxial growth. Experimental work along these lines is in progress. In summary, it may be anticipated that (NiCo)FeGa has good prospects to become a future ferromagnetic shape memory alloy provided that the quaternary phase can be experimentally stabilized. The values of T_C and T_M estimated from $\Delta E_{c/a}$ in Tab. 9.1 hints towards a martensitic transformation in the ferromagnetic phase. Also the onset of twin boundary formation with little cost in energy in the martensitic state looks promising, see Fig. 9.3. Although, the energetics associated with this "nanotwin boundary" formation in comparison to the "Nanotwins" in Ni_2MnGa in Fig. 3.7 will require further investigations which is beyond the scope of the present thesis. Here, I have focused more on the realization of new FMSA by using the most pronounced transition-metal elements Fe, Mn, Co, and Ni instead of the NiMn-based Heusler alloys.

10 Summary

The main aspect of this work was to provide a comprehensive characterization of the structural, magnetic, electronic, and vibrational properties of various transition metal based Heusler alloys using *ab initio* and Monte Carlo simulations with the aim to propose new FSMA with higher operation temperatures and an optimized ductility appropriate for future smart material applications in the automotive or aeronautical sector.

- In the first part of this work I have presented the reconstruction of the experimental phase diagram of the prototypical series Ni-Mn-Z with Z = Ga, In, Sn, Sb which is a shared work of M. Siewert and me. The linear trends of the experimental data with e/a are nicely reproduced by the theoretical calculations. But despite the strong dependence of T_M on e/a is was not possible so far to shift both, T_C and T_M, to values of 100 - 200 K above room temperature. Thus, there is an urgent need for new FSMA.

- In the light of this, I investigated the physical properties of ternary X_2YZ Heusler alloys based on Ni, Co, and Fe as X, and Y elements and Ga, and Zn as Z-elements. Thereby, I successively exchanged the elements on the X, Y, and Z sites with the aim to minimize the disadvantage and maximize the beneficial impacts of the single constituents.
  - The very first systems were Ni_2Co(Ga, Zn) in which Mn was replaced by Co in order to avoid the unfavorable antiferromagnetic tendencies of Mn. These systems are martensitic but the Curie temperatures are below room temperature. Thus, I changed the composition from Ni-rich to Co-rich Co_2Ni(Ga, Zn) systems in order to ensure a high T_C. Co_2NiGa had already been proposed as new FSMA but still T_C and T_M are only slightly above room temperature.
  - Therefore, the next idea was to use Fe instead of Ni in order to guarantee strong ferromagnetic coupling. And indeed, in the Fe-rich as well as the Co-rich Fe-Co-Ga(Zn) systems fairly high T_C are found (700 - 1000 K). Here, the inverse Heusler structure, which does not show a martensitic instability, appears to be energetically favorable. With one exception, Fe_2CoZn in which the martensitic conventional Heusler structure is energetically favorable but a positive mixing energy implies segregation of Zn during experimental making.
  - This inspired me to start a very detailed investigation of the influence of Zn on the physical properties of $Fe_2CoGa_{1-x}Zn_x$ alloys. With the result that Zn was found to have benefi-

cial impact on the magnetic properties of the alloy and enhances T_C but at the same time reduces the miscibility. During my studies on the influence of Zn, I encountered other very interesting and exciting physics: Zn also promotes the tendency for a second energy minimum in the inverse Heusler phase and the idea of inverse martensites, i.e. materials which show the martensitic transformation in the inverse phase, emerged. Fe_2Co(Ag, Au, Cu) and $Fe_7Co_4Zn_5$ are promising candidates but positive mixing energies still hamper their making. Nevertheless, I believe that these systems are worthwhile for future theoretical as well as experimental studies. Concerning magnetism in these Fe-rich Fe-Co-based systems the simple ridgid-band Stoner model is no longer valid, instead, the theory of covalent magnetism has to be applied in agreement with the results of previous theoretical studies of Fe-Co alloys of Schwarz *et al.* The conclusion of this chapter is that disordered $Fe_2CoGa_{1-x}Zn_x$ alloys are interesting systems with respect to future smart materials applications although the production may be challenging due to the high vapor pressure of Zn.

  - The conclusion for the ternary systems is that although Ni, Co, and Fe have beneficial properties none of the ternary systems investigated so far is, at least in the stoichiometric composition, appropriate for future FSMA applications. Thus, in order to combine the advantageous properties of the three transition metals Fe, Co, and Ni within an alloy which has the same or similar e/a as prototype FSMA Ni_2MnGa (e/a = 7.5), quaternary (X1X2)YZ Heusler alloys with X1, X2, Y = Ni, Co, Fe, and Z = Ga, Zn have been considered in the last part of this thesis. Concerning the structural ordering of the three transition metal atoms on the X- and Y-sites the (NiCo)FeGa (e/a = 7.5) ordering type is clearly energetically favored. The Curie temperature of (NiCo)FeGa is high of the order of 590 K and the approximate martensitic transformation temperature is about 3 times higher than in Ni_2MnGa. The phonon dispersions of (NiCo)FeGa bear strong resemblance to Ni_2MnGa and the softening of the TA_2 branch in [110] direction is even more pronounced indicating the possibility of a structural phase transformation. To account for structural disorder, a completely disordered alloy was simulated by means of a computationally demanding 128 atom supercell calculation with random distribution of atoms. During relaxation, a 2 fold modulated twin structure appeared at the local energy minimum of $c/a = 0.85$ which suggests an extraordinarily low twin boundary creation energy and indicates the possibility of an adaptive phase. These observations render Ni-Co-Fe-Ga a very interesting candidate for future ferromagnetic shape memory purposes.

- A central goal of this thesis was to explain the strong preference of the cubic inverse Heusler structure for the Fe-rich Fe-Co-based systems. By a detailed inspection of the electronic structure I could figure out significant features in the element specific density of states causing the instability of the $L2_1$ Heusler structure. And a carefully investigation of the nearest neighbor

coordination allowed to conclude that the favorable bcc-like crystal environment of the Fe atom is one of the central reasons for the high stability of the cubic inverse structure.

- Very interesting is the observation of Slater-Pauling behavior in various families of Heusler alloys which indicates that despite of the complicated hybridization effects between the transition-metals the overall character of the 3*d* electrons is still localized.

A summary of the *ab initio* equilibrium data of all alloys calculated in the framework of this thesis is given in Table 10.1 .

Table 10.1: Calculated equilibrium parameters of all systems investigated in the framework of this thesis. All alloys have been considered in the Heusler structure. Average valence number per atom e/a, stable structure (St) at $T = 0$ K (absolute energy minimum), equilibrium lattice constant a_0 for the cubic $(c/a = 1)$ phase, tetragonal distortions c/a of the two energy minima, Curie temperatures T_C of the $c/a > 1$ phases, energy difference between the cubic phase at $c/a = 1$ and the absolute energy minimum at $c/a > 1$, $\Delta E_{c/a}$, and mixing energy E_{mix} at the absolute energy minimum ($c/a > 1$). 'unst' refers to an unstable structure, i.e. the mixing energy is positive. *The Curie temperature of (PtNi)MnGa has been calculated by Denis Comtesse [155].

System	e/a	St	a_0 (Å)	c/a		T_C	$\Delta E_{c/a}$	E_{mix}
Co_3Ga	7.5	cubic	5.702	1.00	1.34	658	-5	-410
Ni_3Ga	8.25	cubic	5.702	0.94	1.30	NM	24	-1155
Fe_3Ga	6.75	cubic	5.702	0.96	1.21	836	4	-458
Fe_3Co	8.25	cubic	5.706	1.00	/			
Co_3Fe	8.75	$L1_0$	5.655	1.00	1.42			
Fe_2CoGa	7	$L1_0$	5.774	0.88	1.46	770	56	-463
(FeCo)FeGa	7	cubic	5.736	1.0	/	780	/	-642
$Fe_2CoGa_{0.75}Zn_{0.25}$	6.9375	$L1_0$	5.779	0.91	1.44	802	54	-333
$Fe_9Co_4Ga_3$	7.3125	$L1_0$	5.76					
$(FeCo)Fe_{1.25}Ga_{0.75}$	7.3125	cubic	5.726					
$(FeCo)Fe_{0.5}Ga_{1.5}$	6.375	cubic	5.754					
$(FeNi_{0.5})Fe_{1.5}Ga$	7	cubic	5.754					
$(FeCo)FeGa_{0.75}Zn_{0.25}$	6.9375	cubic	5.744	1.0	/	768	/	-458
$Fe_2CoGa_{0.25}Zn_{0.75}$	6.8125	$L1_0$	5.780	0.9	1.42	896	49	-721
$(FeCo)FeGa_{0.75}Zn_{0.75}$	6.8125	cubic	5.748	1.0	/	830	/	-328
Fe_2CoZn	6.75	unst	5.782	0.92	1.40	925	48	51
(FeCo)FeZn	6.75	unst	5.750	1.0	1.36	850	-11	135
$Fe_7Co_4Zn_5$	6.375	$L1_0$	5.806	0.94	1.38		5	338
$(FeCo)Fe_{0.75}Zn_{1.25}$	6.375	$L1_0$	5.776	0.98	1.40		60	
$(FeCo)FeGa_{0.5}Mn_{0.5}$	7.5	cubic	5.711					
Fe_2CoCu	6.5	$L1_0$	5.742	0.9	1.35		53	
(FeCo)FeCu	6.5	$L1_0$	5.718	0.94	1.46		/	479
Fe_2CoAg	6.5	$L1_0$	5.996	0.88	1.38		62	1164
(FeCo)FeAg	6.5	$L1_0$	5.970	0.92	1.42		32	
Fe_2CoAu	6.5	$L1_0$	6.020	0.85	1.40		87	
(FeCo)FeAu	6.5	$L1_0$	5.986	0.90	1.42		63	
Fe_2CoGe	7.25	$L1_0$	5.738					
(FeCo)FeGe	7.25	cubic	5.718				/	
Fe_2CoSb	7.5	$L1_0$	5.978	0.9	1.35		53	
(FeCo)FeSb	7.5	cubic	5.992	0.94	1.46		/	479
$(FeCo)Fe_{0.75}Si_{1.25}$	7.00	cubic	5.718					
(FePd)CoGa	7.50	$L1_0$	5.968	0.98	1.38			
(CoPd)FeGa	7.50	$L1_0$	5.968	0.94	1.26		/	-864
(FeCo)PdGa	7.50	$L1_0$	5.956	0.85	1.56			

System	e/a	St	a_0 (Å)	c/a		T_C	$\Delta E_{c/a}$	E_{mix}
Ni_2MnGa	7.5		5.71	1.0	/	375		
$Ni_8Mn_5Ga_3$	7.75		5.815	1.0	1.3	314		
$Ni_8Mn_6Ga_2$	8		5.81		1.35	180		
$Ni_8Mn_5In_3$	7.75		6.0125	1.0	/	349		
$Ni_8Mn_6In_2$	8		5.95	1.0	0.95	353		
Ni_8Mn_7In	8.25		6.07	/	0.91	0		
$Ni_8Mn_5Sn_3$	7.9375		6.01	1.0	/	415		
$Ni_8Mn_6Sn_2$	8.125		5.95	1.0	0.94	398		
Ni_8Mn_7Sn	8.3125		5.885	/	0.91	262		
$Ni_8Mn_5Sb_3$	8.125		5.815	1.0	/	402		
$Ni_8Mn_6Sb_2$	8.25		5.81	1.0	1.30	458		
Ni_8Mn_7Sb	8.375		5.71	/	0.91	375		
(PtNi)MnGa	7.5	$L1_0$	6.04	0.90	1.32	375*		
(NiCo)FeGa	7.5	$L1_0$	5.757	0.95	1.25	590	19	-890
(FeCo)NiGa	7.5	$L1_0$	5.716	0.88	1.51	530	100	-718
(FeNi)CoGa	7.5	$L1_0$	5.741	1.01	1.42	365	32	-614
Disorder	7.5		5.766	0.85	1.42	/	25	/
(NiCo)FeZn	7.25	cubic	5.743	1.0	/	733	/	-330
(FeCo)NiZn	7.25	$L1_0$	5.741	0.85	1.55	523	126	-118
(FeNi)CoZn	7.25	$L1_0$	5.743	0.97	1.41	600	42	-97
Ni_2CoGa	8	$L1_0$	5.720	0.86	1.38	213	66	-825
(NiCo)NiGa	8	$L1_0$	5.704	0.91	1.32	175	39	-810
Ni_2CoZn	7.75	$L1_0$	5.710	0.88	1.38	273	59	-212
(NiCo)NiZn	7.75	$L1_0$	5.703	0.94	1.40	312	42	-157
Co_2NiGa	7.75	$L1_0$	5.695	1.00	1.41	377	27	-569
(CoNi)CoGa	7.75	$L1_0$	5.710	0.89	1.31	452	44	-650
Co_2NiZn	7.5	$L1_0$	5.688	0.94	1.5	556	81	30
(CoNi)CoZn	7.5	$L1_0$	5.706	1.00	1.35	574	33	0

10.1 Conclusion

The remarkable aspect of this work is that with the systematic and successive approach in search for new FSMA, combining the results for the ternary systems studied before, I was able to propose the quaternary Ni-Co-Fe-Ga system as new FSMA which provides, at least from a theoretical point of view, very promising features with respect to future smart materials. The comparison with experimental results shows that the calculation of mixing energies is an important task in order to be able to predict decomposition tendencies which may lead to the occurrence of two or more stable phases in one sample. In summary, I can conclude that despite the fact that it is a very challenging and demanding task to find material classes which combine high T_C and high T_M with the outstanding magnetoelastic properties of smart materials, *ab inito* calculations of structural, electronic, magnetic, and vibrational properties are essential to yield results which are reliable and of predictive nature. Only this allows to predict promising candidates for future FSMA and helps the experimentalists to find interesting groups of new materials. In this context I refer also to the appendix 11.3 where preliminary results of another shape-memory-system (Pt-Ni-Mn-Ga) are briefly discussed.

11 Appendix

11.1 Phonons

Phonons in crystals are correlated to the displacements of the atoms in one unit cell. They are extended vibrational modes which propagate with a wave-vector $\mathbf{q}$ and vibrational frequency $\omega(\mathbf{q})$. The $\mathbf{q}$ wave-vector is equivalent to the Bloch vector for the electronic states. It resides in the unit cell of the reciprocal lattice, the first Brillouin zone. In analogy to the electronic states, phonon frequencies form dispersion bands. If a system has N atoms in the unit cell, $3N$ phonons exist for a given $\mathbf{q}$. Let $u_i[\mathbf{R}]$ describe the displacement of atom i at lattice site $\mathbf{R}$

$$F = M_i \frac{\partial^2 u_i[\mathbf{R}]}{\partial t^2} = -\frac{\partial V}{\partial u_i[\mathbf{R}]}, \tag{11.1}$$

where V is the crystal potential. It is here treated as harmonic potential which means that in the Taylor expansion of V terms higher than quadratic order are not taken into account. Thus, $V \sim u^2$. The dynamical matrix contains the information on the vibrational properties of a crystal. The second derivatives of the elastic potential with respect to the atomic positions $\mathbf{R}$ are the elements of the dynamical matrix $\mathbf{D}_{ij}$.

$$\mathbf{D_{ij}}(k) = \sum_{R_p} \left(\frac{\partial^2 V}{\partial u_i[\mathbf{R}+\mathbf{R_p}] u_j[\mathbf{R}]}\right) e^{-ik\mathbf{R_p}} \tag{11.2}$$

where the sum is over all lattice vectors. The dispersion relation can then be determined through

$$\mathbf{M}^{-1}\mathbf{D}(\mathbf{k}) = \omega^2 \tag{11.3}$$

where M is a diagonal matrix with the masses of the atoms in the unit cell. The eigenvalues of the dynamical matrix are the squares of the vibrational frequencies while the atomic displacements are related to its eigenvectors. The transverse modes are denoted by capital T while longitudinal modes are marked by a capital L. The transverse accustical modes along the [110] direction are consequently denoted by TA_1[110] and TA_2[110].

11.2 Crystal fields in Heusler alloys

I will consider the representative case of Co_2MnGe. The whole crystal field of full-Heusler alloys has tetrahedral symmetry. Figure 11.1 demonstrates the different crystal environment of Co (Ni) and Mn

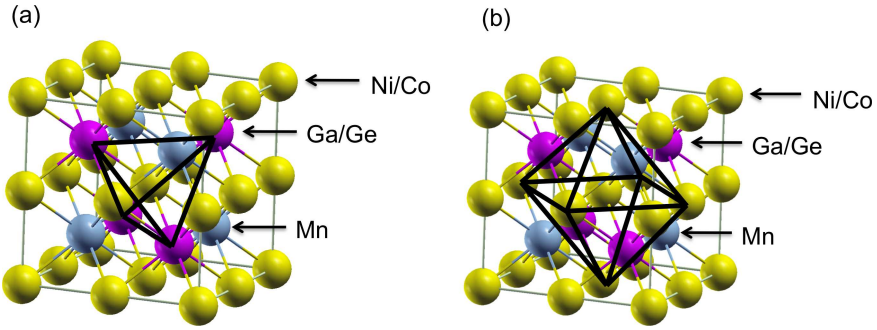

Figure 11.1: 16 atom unit cells of Co_2MnGe or Ni_2MnGa, respectively. The yellow spheres mark the Co (or Ni) atoms, magenta spheres denote Ge (or Ga) atoms and grey spheres belong to Mn atoms. Black solid lines schematically represent (a) the tetrahedral crystal field acting on the Mn and Ge (or Ga) atoms, (b) the octahedral crystal field which exerts on the Co (or Ni) atoms.

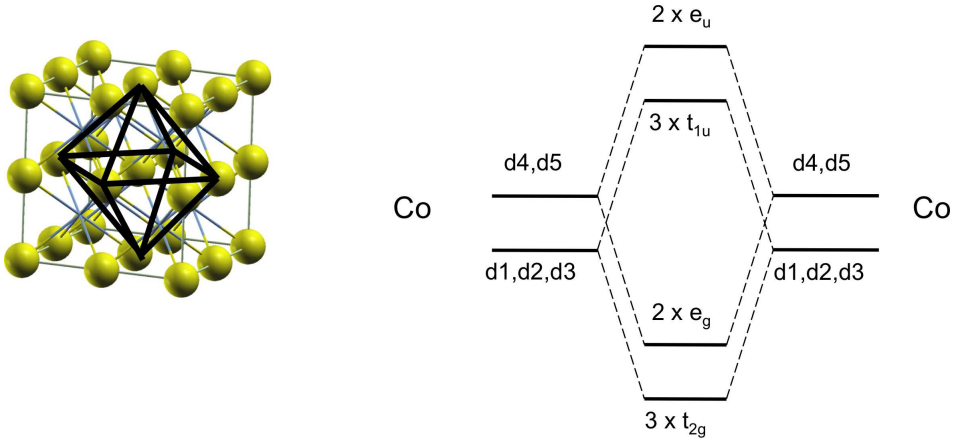

Figure 11.2: Left: Cubic lattice of a hypothetical Co-Co compound in a $L2_1$ structure without Mn and Ge atoms respecting the octahedral symmetry. Right: Resulting hybridization between spin-down orbitals of two neighboring Co-atoms. The d1, 2, 3, 4, 5 orbitals correspond to the d_{xy}, d_{yz}, d_{zx}, $d_{3z^2-r^2}$, and the $d_{x^2-y^2}$ orbitals. The atomic d4 and d5 orbitals form two degenerated bonding e_g and two degenerated antibonding e_u orbitals. The d1, d2, and d3 orbitals also hybridize and create triple-degenerated bonding t_{2g} and anti-bonding t_{1u} orbitals.

(or Ge, Ga) atoms. The two Co atoms are exposed to an octahedral crystal field, compare also Fig. 11.2, while the Mn and the Ge atoms are affected by a tetrahedral crystal field. The hybridization scenario of the spin-down orbitals of two neighboring Co atoms is schematically depicted in Fig. 11.2. The minority-spin d1, 2, 3 orbitals of the two Co atoms form triple-degenerated bonding t_{2g} and anti-bonding t_{1u} orbitals while the d4, 5 orbitals create double-degenerated bonding e_g orbitals and anti-bonding e_u orbitals. The Mn and the Ge atoms are affected by a crystal field of tetrahedral symmetry which results into orbitals with only t_{2g} and e_g symmetry so that the t_{1u} and e_u states are

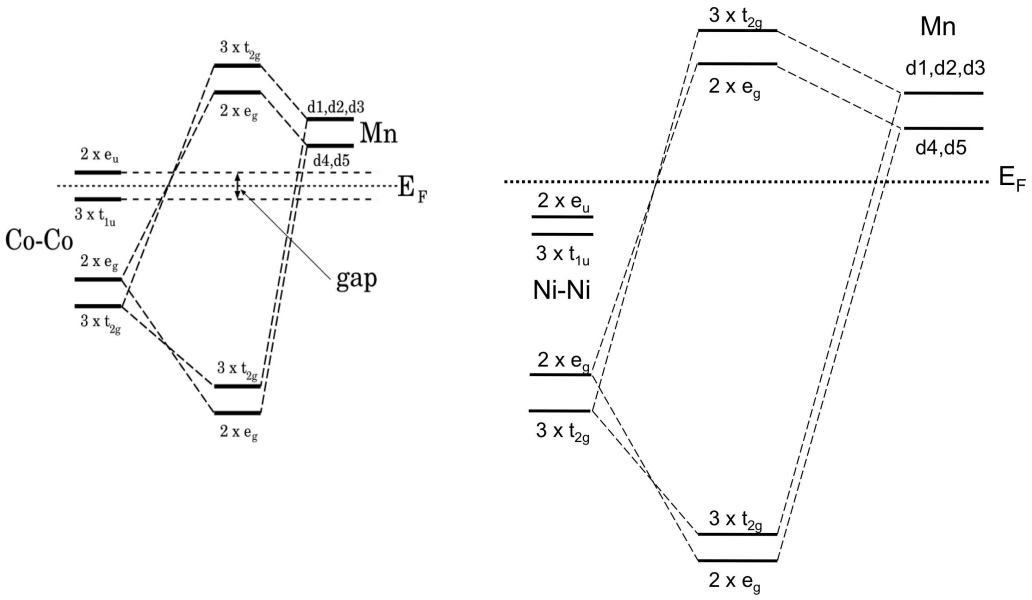

Figure 11.3: Hybridization between spin-down orbitals of Co-Co and Mn atoms on the left and Ni-Ni and Mn atoms on the right hand. The Mn atoms are exerted by a crystal field with tetrahedral symmetry. Thus the $d1,2,3$ orbitals hybridize into double-degenerated bonding and antibonding e_g orbitals. The $d4,5$ orbitals create triple-degenerated bonding and anti-bonding t_{2g} orbitals. The e_u and t_{1u} orbitals of the Co (Ni) atoms cannot couple with any of the Mn orbitals as there are nontransforming with the u representation. The left part of the figure is adapted from [134].

missing, see Figure 11.3. Thus, the two e_u and the three t_{1u} states of the Co atoms cannot couple with any of the Mn orbitals and are located exclusively at the Co sites, compare Fig. 11.4(a) and (c). The Co t_{1u} states lie below the Fermi-level and are occupied while the Co e_u states appear just above E_F. This is the origin of the characteristic gap in the minority-spin channel of the half-metallic Heusler compound Co_2MnGe, cf. Fig. 11.4(a, c). In total, there are eight occupied minority-spin states below E_F and seven unoccupied minority-spin states above the Fermi level. If one also accounts for the one s state and the three states with p character, altogether 12 minority states are occupied per unit cell which explains the simple rule $M = Z - 2 * N_{\downarrow} = Z - 24$ relevant for the half-metallic Heusler systems. As a result of the seven unoccupied minority spin states the largest possible moment of a full-Heusler alloy is 7 μ_B. This discussion follows the work of Galanakis *et al.* [134] Crystal defects, disorder, and many-body effects will of course change this one-electron picture. A direct comparison of the atom- and orbital-resolved DOS of half-metallic Co_2MnGe (e/a = 7.25) and metallic Ni_2MnGa (e/a = 7.5) Heusler alloys allows further insight into the underlying physics, see Fig. 11.4. The DOS of Mn in Co_2MnGe possesses a broad gap in the minority spin channel which is not present for Co, cf. Fig. 11.4(a, c). Hence, the states around the Fermi-energy are only Co states, namely the states with t_{1u} and e_u symmetry as discussed above. In the corresponding DOS of Ni_2MnGa the half-metallic gap has disappeared as a result of the enhanced number of valence electrons, cf. Fig. 11.4(b, d).

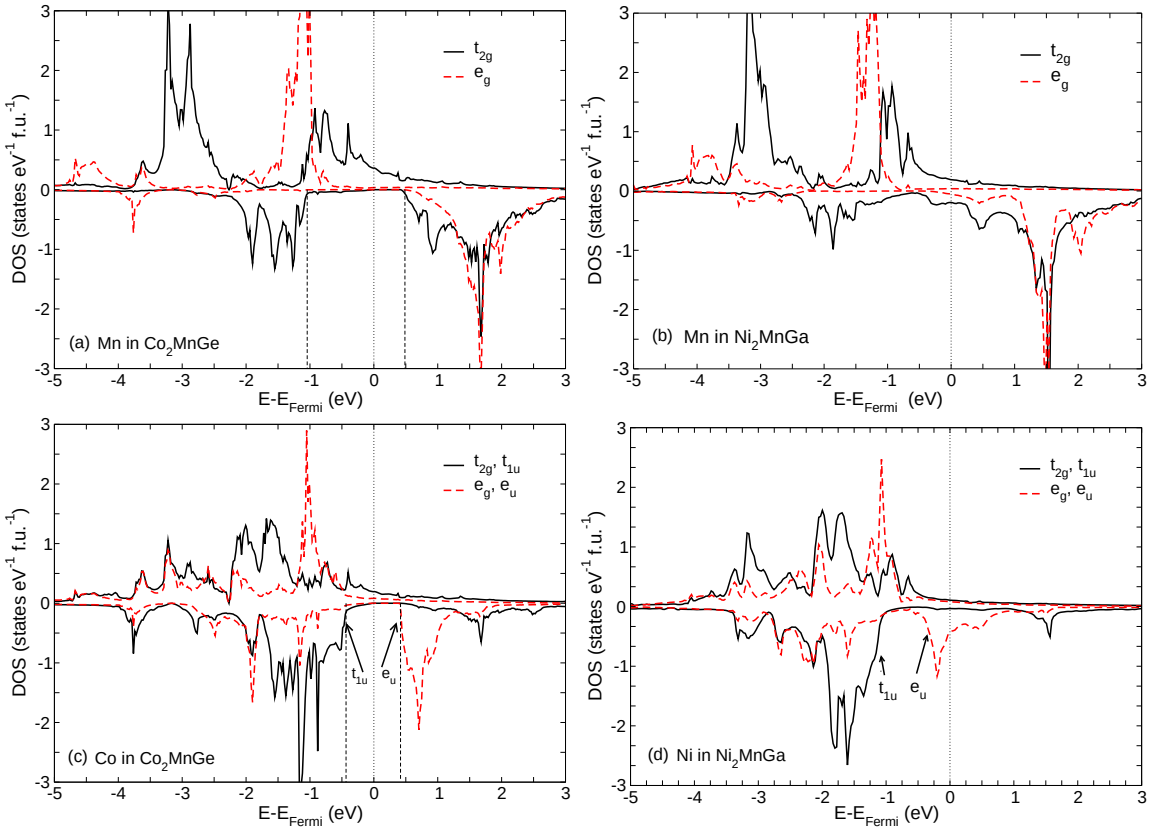

Figure 11.4: Atom- and orbital-resolved DOS of Co_2MnGe (e/a = 7.25) on the left and Ni_2MnGa (e/a = 7.5) on the right. Black solid lines label states with t_{2g} (and t_{1u} for the case of Co and Ni) symmetry and red dashed lines mark states with e_g (and e_u for the case of Co and Ni) symmetry. (a) DOS of Mn in Co_2MnGe with a wide gap in the minority spin channel. (b) DOS of Mn in Ni_2MnGa without any sign of a gap. (c) DOS of Co in Co_2MnGe with the t_{1u} and e_u states around E_F. (d) DOS of Ni in Ni_2MnGa for which the t_{1u} and e_u states are shifted to energies below E_F due to the larger number of valence electrons in Ni_2MnGa.

11.3 Adaptive Martensite

Technologically relevant for the FSME are the modulated phases (e.g., the 5M, or the 7M phase). These phases can be understood by employing the concept of adaptive martensite which states that the modulated phase can be conceived by nanotwinned variants of the tetragonal martensite phase. The concept of adaptive martensite [156–159] links the formation of habit plane and twins down to the nanometer range and seems to become an important issue in the discussion of martensitic transformations and magnetic shape memory effect (MSME) [27, 160]. When the surface energy of a twin boundary between two variants of the tetragonal martensite phase is low and the lattice-mismatch-related elastic energy is high an adaptive martensite can be formed. In a variety of functional materials relatively weak electrical or magnetic fields can change the microstructure of the solid provided that a

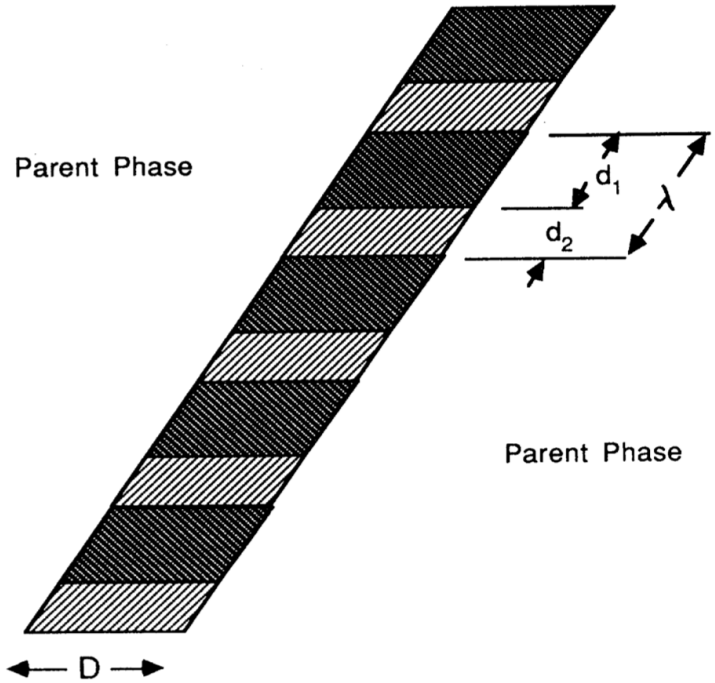

Figure 11.5: Schematics of the martensitic phase plate composed of two martensite variants with different orientations. The lattice mismatch between the parent austenitic phase and the product martensitic phase is fixed by the appropriate d_1 to d_2 ratio. Figure taken from [159].

modulated structure is present [161, 162]. In the theory of Khachaturyan *et al.* these modulated structures are considered as twinned metastable structures and not as thermodynamically stable structures. The parent cubic and martensite phase determine the crystal-lattice parameters of the adaptive phase. A martensitic transformation can occur when the elastic energy generated by the lattice mismatch between the parent austenitic phase and the product martensite phase is greater than the transformation chemical driving force:

$$\mu\varepsilon_0^2 / |\Delta f| \gg 1. \tag{11.4}$$

Here, $\mu\varepsilon_0^2$ is the elastic energy, ε_0 is the strain resulting from the mismatch between the parent and the product phase, μ is the shear modulus, and $|\Delta f|$ is the transformation driving force which is equal to the difference between the free energies of the parent and product phases. The constrain for the structural transformation from a high-symmetry austenite to a low-symmetry martensite phase is that the martensite is accommodated to a habit plane which fixes the geometrical relationship between the two phases. The lattice mismatch is adjusted by periodic alternation of two twins, i.e. two orientational variants of the martensite. It has been shown by Khachaturyan [163] and Roytburd [164] that the formation of a martensitic phase plate as given in Fig. 11.5 does not generate the volume-dependent elastic energy. This elastic energy and the surface energy of the twin boundaries determine the period

Table 11.1: Twinning periodicity d_1/d_2 for the promising new systems.

System	e/a	a_0(Å)	c/a		$\frac{d_1}{d_2}$
Fe_2CoGa	7	5.774	0.88	1.46	0.531
$Fe_2CoGa_{0.75}Zn_{0.25}$	6.9375	5.779	0.91	1.44	0.525
$Fe_2CoGa_{0.25}Zn_{0.75}$	6.8125	5.780	0.90	1.42	0.527
Fe_2CoZn	6.75	5.782	0.92	1.40	0.520
(NiCo)FeGa	7.5	5.757	0.95	1.25	0.510
Disorder	7.5	5.766	0.85	1.42	0.542
(CoNi)CoGa	7.75	5.710	0.89	1.31	0.529

λ of the lamellae:

$$\lambda \sim \left[\frac{\gamma_{tw}}{\mu\varepsilon_0^2 D}\right]^{1/2}, \tag{11.5}$$

where D is the width of the plate, and γ_{tw} is the twin surface energy. The large unit cell of the metastable modulated phase can be constructed by nanotwin lamellae of the simple, thermodynamically stable, tetragonal unit cell of the martensite phase. If D and the twin surface energy γ_{tw} are small and the elastic energy $\mu\varepsilon_0^2$ is large the twin size λ is also small given that the ratio of the volumes of the twins ω is kept constant. The limitation is defined by the fact that the lamellae thickness cannot be less than the interplanar distance a_{tw} of the twinning plane and that the thickness of the two twins d_1 and d_2 must be a multiple of a_{tw}:

$$\omega_0 = \frac{\varepsilon_{11}^0}{\varepsilon_{11}^0 - \varepsilon_{33}^0} > 0. \tag{11.6}$$

$$\frac{d_1}{d_2} = \frac{\omega}{1-\omega},\ d_1 = m a_{tw},\ d_2 = n a_{tw},\ d_1 + d_2 = \lambda, \tag{11.7}$$

where m and n are small integers. The geometrical martensite theory predicts a periodic twinning of the tetragonal martensite lattice which is expressed through the fraction of the twin lamella width d_1 and d_2 [27]:

$$\frac{d_1}{d_2} = \frac{(a_t - a_0)}{(a_0 - c_t)}. \tag{11.8}$$

Here, a_t and c_t are the lattice constants for the a-axis and the corresponding c-axis for the tetragonal distorted energy minimum at $c/a < 1$, cf. Fig. 3.9. In Table 11.1 the calculated twinning periodicity for the most promising new systems is listed. The microtwin boundaries repel each other which limits the miniaturization of twins. There are three characteristic features of an adaptive martensite:
(1) The unit cell of the adaptive martensite is related to the unit cell of the parent austenitic unit cell by an invariant plane strain.
(2) The shuffling planes must always be parallel to the twinning plane. (For the cubic to tetragonal transformation this condition is discussed in the next section 11.3.1 and predicts the (110) plane which

is in fact observed for the prototype FSMA Ni-Mn-Ga.)
(3) Equation 11.7 yields:

$$\frac{\omega_0}{1-\omega_0} = \frac{m}{n}, \tag{11.9}$$

where ω_0 is related to the volume fraction of one martensitic variant (cf. Fig. 11.5). Thus, the third condition is unambiguously determined by the lattice parameters of the martensite and the austenite phase. In the next subsection 11.3.1 the basic features of the cubic to tetragonal martensitic transformation are introduced.

11.3.1 Cubic to tetragonal martensitic transformation

In the cubic to tetragonal martensitic transformation one of the three cubic lattice parameters, a_0, transforms to the c-axis of the tetragonal martensite phase, c_t, while the other two cubic parameters are transformed into the a_t parameter (compare the Bain-transformation schematically depicted in Fig. 3.9). The crystal lattice deformations which result in the three symmetry-related variants (cf. Fig. 3.1) are given by the three stress-free tensors:

$$\begin{aligned}
\varepsilon(1)^0_{ij} &= \begin{Bmatrix} \varepsilon^0_{33} & 0 & 0 \\ 0 & \varepsilon^0_{11} & 0 \\ 0 & 0 & \varepsilon^0_{11} \end{Bmatrix}, \\
\varepsilon(2)^0_{ij} &= \begin{Bmatrix} \varepsilon^0_{11} & 0 & 0 \\ 0 & \varepsilon^0_{33} & 0 \\ 0 & 0 & \varepsilon^0_{11} \end{Bmatrix}, \\
\varepsilon(3)^0_{ij} &= \begin{Bmatrix} \varepsilon^0_{11} & 0 & 0 \\ 0 & \varepsilon^0_{11} & 0 \\ 0 & 0 & \varepsilon^0_{33} \end{Bmatrix}.
\end{aligned} \tag{11.10}$$

The strain components $\varepsilon(1)^0_{33} = (c_t - a_0)/a_0$, $\varepsilon(1)^0_{11} = (a_t - a_0)/a_0$ define the lattice mismatch between the austenite and the tetragonal martensite structure. The mismatch between any two variants, e.g. (2) and (1), then reads

$$\begin{aligned}
\Delta\varepsilon(12)_0 &= \varepsilon(1)^0_{ij} - \varepsilon(2)^0_{ij} \\
&= (\varepsilon^0_{33} - \varepsilon^0_{11}) \begin{Bmatrix} 1 & 0 & 0 \\ 0 & \overline{1} & 0 \\ 0 & 0 & 0 \end{Bmatrix}.
\end{aligned} \tag{11.11}$$

The tensor $\Delta\varepsilon(12)_0$ can be rewritten as

$$\begin{aligned}
\Delta\varepsilon(12)_0 &= \varepsilon(1)^0_{ij} - \varepsilon(2)^0_{ij} \\
&= (\varepsilon^0_{33} - \varepsilon^0_{11})(l_i m_j + l_j m_i),
\end{aligned} \tag{11.12}$$

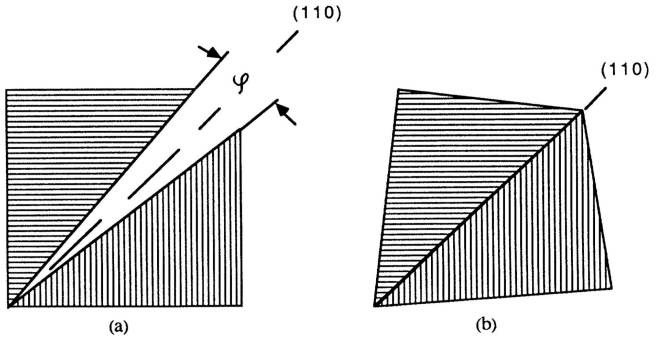

Figure 11.6: Schematic representation of the rotation under adjustment of two variants of martensite along the (110) plane. (a) A gap opens up without rotation. (b) Rotation of the angle ϕ restores a crystal-continuity across the (110) boundary plane. Figure taken from [159].

where $l = (1/\sqrt{2}, \overline{1}/\sqrt{2}, 0)$ and $m = (1/\sqrt{2}, \overline{1}/\sqrt{2}, 0)$ are unit vectors along the $[1\overline{1}0]$ and [110] directions. In order to avoid a gap opening up between two variants of the martensite (cf. Fig. 11.6) the neighboring twins rotate by the angle:

$$\phi = 2\left[\arctan\frac{c_t}{a_t} - \frac{\phi}{4}\right]. \tag{11.13}$$

The total stress-free macroscopic shape change is given by the average of the respective strains:

$$\overline{\varepsilon}_{ij} = \omega\varepsilon(1)^0_{ij} + (1-\omega)\varepsilon(2)^0_{ij}, \tag{11.14}$$

where ω and $1-\omega$ are the volume fractions of the two martensite variants. In order to guarantee a stress-free boundary between parent and product phases the mismatch tensor $\overline{\varepsilon}_{ij}$ should be an invariant plain strain which is possible if one of the components of $\overline{\varepsilon}_{ij}$ disappears. This is given when ε^0_{33} and ε^0_{11} have different signs and if $\left|\varepsilon^0_{33}\right| > \left|\varepsilon^0_{11}\right|$ which is fulfilled for practically all known martensitic transformations. Following Ref. [163, 164] we get $\omega = \omega_0$ for small strain which leads to an invariant plane strain:

$$\omega_0 = \frac{\varepsilon^0_{11}}{\varepsilon^0_{11} - \varepsilon^0_{33}} > 0. \tag{11.15}$$

The average strain tensor $\overline{\varepsilon}_{ij}$ with ω_0 defined by Eq. 11.15 can be written as

$$\overline{\varepsilon}_{ij} = \begin{Bmatrix} 0 & 0 & 0 \\ 0 & \varepsilon^0_{33} + \varepsilon^0_{11} & 0 \\ 0 & 0 & \varepsilon^0_{11} \end{Bmatrix}. \tag{11.16}$$

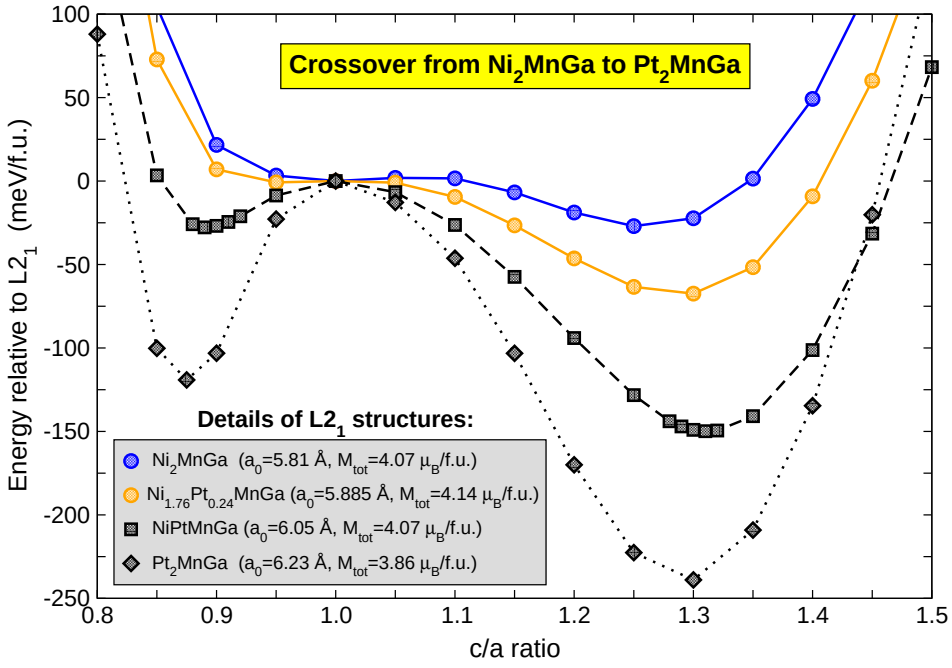

Figure 11.7: The martensitic energy landscape of Ni_2MnGa (blue circles), $Ni_{1.76}Pt_{0.24}MnGa$ (orange circles), NiPtMnGa (black squares), and Pt_2MnGa (black diamonds). By subsequently substituting Pt for Ni, $\Delta E_{c/a}$ (and with this also T_M) can be changed.

With the constraint that ε^0_{33} and ε^0_{11} have different signs as discussed above, $\overline{\varepsilon}_{ij}$ is an invariant plane strain with its habit plane normal to the vector

$$n = \left[0, \left[\frac{|\varepsilon^0_{33}+\varepsilon^0_{11}|}{|\varepsilon^0_{11}|+|\varepsilon^0_{33}+\varepsilon^0_{11}|}\right]^{1/2}, \left[\frac{|\varepsilon^0_{11}|}{|\varepsilon^0_{11}|+|\varepsilon^0_{33}+\varepsilon^0_{11}|}\right]^{1/2}\right]. \tag{11.17}$$

The concept of adaptive martensite and the resulting twinning periodicity, as listed in Table 11.1 for a few new FSMA, has been introduced by the group of S. Fähler [27] and discussed in greater detail in [160] for Ni_2MnGa. This concept, as briefly introduced in 11.3 and 11.3.1, is important because it may in part explain the reason for the high twin mobility in FSMA because the twins can form with *practically zero energy* (i.e. very low energy). Since this concept has not yet been fully formulated on a theoretical basis but seems to be *at the heart* of the FSMA [165]. I just note that the formation of twins in Ni-Co-Fe-Ga as shown in Fig. 9.3 is the same as the appearance of nanotwins in Ni_2MnGa as anticipated in Ref. [27], see Fig. 3.7 which shows the nanotwins in case of the 14M structure of Ni_2MnGa. Regarding the adaptive feature of magnetic shape-memory materials I would like to mention that our group recently discovered another candidate filling into this category, namely Pt-Ni-Mn-Ga of which the martensitic energy landscape in form of $E_{c/a}$ curves is shown in Fig. 11.7. The addition of a small amount of Pt to Ni-Mn-Ga alloys allows to continuously change $\Delta E_{c/a}$ and

thereby T_M [166]. The hitherto too low magnetic transition temperatures T_C can be enhanced by adding Co. The remarkable feature is that the nonmodulated tetragonal structure corresponding to the minimum of $c/a = 1.32$ for NiPtMnGa and Pt_2MnGa can be constructed from 14M modulated structures at $c/a = 0.9$. For both structures the energy seems to converge to the same value. This is the same trend as for Ni_2MnGa [167]. This also allows to give an estimate of the maximum magnetic shape-memory effect that can be achieved in Pt-Ni-Mn-Ga: Since twin boundary formation and hence magnetically induced strain (MIS) is easily activated for the twins which form at $c/a < 1$ (and not for the twins at $c/a > 1$ when the system undergoes a martensitic transformation), one may tentatively take the position of the energy minimum at $c/a < 1$ for the estimate. This yields for Pt-Ni-Mn-Ga a maximum magnetic shape-memory effect (MSME) of 10% ($c/a \sim 0.9$) which is of the same order as the maximal MSME in $Ni_{48.8}Fe_{29.7}Ga21.5$ [162].

Bibliography

[1] Z. Nishiyama, *Martensitic transformation*, Academic Press, New York 1978.

[2] A. L. Roytburd, *Martensitic transformation as a typical phase transformation in solids*, in Solid State Physics, edited by H. Ehrenreich, F. Seitz and D. Turnbull, vol. 33, pp. 317–390, Academic Press, New York 1978.

[3] K. Otsuka and C. M. Wayman, *Martensitic transformation*, University Press, Cambridge 1998.

[4] R. W. Cahn, P. Haasen and E. J. Kramer, in Materials Science and Technology - A Comprehensive Treatment, edited by R. W. Cahn and P. Haasen, vol. 5, pp. 1–648, VCH Publishers Inc., Weinheim 1991.

[5] O. Söderberg, A. Sozinov, Y. Ge, S. P. Hannula and V. Lindroos, *Giant magnetostrictive materials*, in *Handbook of Magnetic Materials*, edited by J. Buschow, pp. 1–39, Elsevier, Amsterdam 2006.

[6] Y. A. Izyumov and V. Syromyatnikov, *Phase transitions and crystal symmetry*.

[7] S. Kartha, T. Castán, J. A. Krumhansl and J. P. Sethna, *Spin-glass nature of tweed precursors in martensitic transformations*, Phys. Rev. Lett. **67**, 3630 (1991).

[8] F. E. Fujita and R. W. Cahn, *Physics of New Materials*, in *Series in Materials Science*, vol. 27, Springer, New York 1998.

[9] K. Bhattacharya, *Microstructure of Martensite-Why it forms and how it gives rise to the shape-memory effect*, Oxford Series on Materials Modelling, Oxford University Press, New York 2003.

[10] M. Cohen, G. B. Olson and P. C. Clapp, *On the classification of displacive phase transformations*, in *Proceedings of the International Conference on Martensitic Transformations ICOMAT'79*, pp. 1–11, Dep. of Mat. Science and Techn. M.I.T, Cambridge (MA) 1980.

[11] H. Czichos, *Adolf Martens and the research on martensite*, in *ESOMAT 1989 - Ist European Symposium on Martensitic Transformations in Science and Technology*, edited by E. Hornbogen and N. Jost, pp. 3–14, DGM, Oberursel, Bochum, Germany 1989.

[12] P. A. Lindgård, *Theory and modeling of the martensitic transformation*, J. Phys. IV **1**, C4 3–12 (1991).

[13] L. Delaey, R. V. Krishnan, H. Tas and H. Warlimont, *Thermoplasticity, pseudoelasticity and the memory effects associated with martensitic transformations Part 1 Structural and microstructural changes associated with the transformations*, J. Mater. Sci. **9**, 1521 (1974).

[14] H. Warlimont, L. Delaey, R. V. Krishnan and H. Tas, *Thermoplasticity, pseudoelasticity and the memory effects associated with martensitic transformations Part 2 The macroscopic mechanical behaviour*, J. Mater. Sci. **9**, 1536 (1974).

[15] R. V. Krishnan, L. Delaey, H. Tas and H. Warlimont, *Thermoplasticity, pseudoelasticity and the memory effects associated with martensitic transformations Part 3 Thermodynamics and kinetics*, J. Mater. Sci. **9**, 1545 (1974).

[16] P. Müllner, Z. Clark, L. Kenoyer, W. Knowlton and G. Kostorz, *Nanomechanics and magnetic structure of orthorhombic Ni-Mn-Ga martensite*, Mater. Sci. Eng. A **481-482**, 66–72 (2008).

[17] P. Müllner, V. A. Chernenko and G. Kostorz, *A microscopic approach to the magnetic-field-induced deformation of martensite (magnetoplasticity)*, J. Magn. Magn. Mater. **267**, 325 (2003).

[18] S. Fähler, *An introduction to actuation mechanism of magnetic shape memory alloys*, Electrochemical Society Transactions **25**, 155–163 (2007).

[19] G. B. Johnston and E. O. Hall, *Studies on the Heusler alloys I. Cu_2MnAl and associated structures*, J. Phys.: Conf. Ser. **29**, 193 (1968).

[20] P. J. Webster and K. R. A. Ziebeck, *Heusler alloys*, in Landolt-Börnstein New Series Group III: *Crystal and Solid State Physics - Magnetic Properties of Metals*, edited by H. P. J. Wijn, vol. 19C, pp. 75–185, Springer, Berlin 1988.

[21] K. R. A. Ziebeck and K. U. Neumann, *Heusler alloys*, in Landolt-Börnstein New Series Group III: *Condensed Matter - Magnetic Properties of Metals*, edited by H. P. J. Wijn, vol. 32C, Supplement to Vol.19, pp. 75–185, Springer, Berlin 1988.

[22] M. Gillessen and R. Dronskowski, *A combinatorial study of inverse Heusler alloys by first-principles computational methods*, J. Comput. Chem. **31**, 612 (2010).

[23] A. Dannenberg, M. E. Gruner, M. Wuttig and P. Entel, *Characterization of new ferromagnetic Fe-Co-Zn-Ga alloys by ab initio investigations*, in *ESOMAT 2009 - The 8th European Symposium on Martensitic Transformations*, edited by P. Šittner, L. Heller and V. Paidar, no. 04004, pp. 1200–Go4–03, EDP Sciences (www.esomat.org), Berlin 2009, DOI: 10.1051/esomat/200904004.

[24] A. Dannenberg, M. E. Gruner, M. Wuttig and P. Entel, *First-principle study of ferromagnetic $Ni_2CoGa(Zn)$ alloys in the Heusler and the inverse Heusler structure*, Mater. Res. Soc. Symp. Proc. **1200E**, 1200–G04–03 (2010).

[25] A. Dannenberg, M. E. Gruner, M. Wuttig and P. Entel, *Structural ordering tendencies in the new ferromagnetic Ni-Co-Fe-Ga-Zn Heusler alloys*, Physics Procedia **10**, 144–148 (2010).

[26] P. Entel, V. D. Buchelnikov, M. E. Gruner, A. Hucht, V. V. Khovailo, S. K. Nayak and A. T. Zayak, *Shape memory alloys: a summary of recent achievements*, Mater. Sci. Forum **583**, 21 (2008).

[27] S. Kaufmann, U. K. Rößler, O. Heczko, M. Wuttig, J. Buschbeck, L. Schultz and S. Fähler, *Adaptive modulations of martensites*, Phys. Rev. Lett. **104**, 145702 (2010).

[28] R. Kainuma, F. Gejima, Y. Sutou, I. Ohnuma and K. Ishida, *Ordering, martensitic and ferromagnetic transformations in Ni-Al-Mn Heusler shape memory alloys*, Mater. Trans **41**, 943 (2000).

[29] Y. Sutou, Y. Imano, N. Koeda, T. Omori, R. Kainuma, K. Ishida and K. Oikawa, *Magnetic and martensitic transformations of NiMnX(X=In,Sn,Sb) ferromagnetic shape memory alloys*, Appl. Phys. Lett. **85**, 4358 (2004).

[30] M. Acet, L. Mañosa and A. Planes, *Magnetic-field-induced effects in martensitic Heusler-based magnetic shape memory alloys*, in *Handbook of Magnetic Materials*, vol. 19, p. 231, Elsevier 2011.

[31] W. Maziarz, J. Dutkiewicz, R. Santamarta and E. Cesari, *Microstructure changes in two phase $\beta + \alpha$ Co-Ni-Al ferromagnetic shape memory alloys in relation to Al/Co ratio*, Eur. Phys. J. Spec. Top. **158**, 137 (2008).

[32] Y. Tanaka, K. Oikawa, Y. Sutou, T. Omori, R. Kainuma and K. Ishida, *Martensitic transition and superelasticity of Co-Ni-Al ferromagnetic shape memory alloys with $\beta + \gamma$ two-phase structure*, Mater. Sci. Eng. A **438-440**, 1054 (2006).

[33] P. J. Brown, K. Ishida, R. Kainuma, T. Kanomata, K. U. Neumann, K. Oikawa, B. Ouladdiaf and K. R. A. Ziebeck, *Crystal structures and phase transitions in ferromagnetic shape memory alloys based on Co-Ni-Al and Co-Ni-Ga*, J. Phys.: Condens. Matter **17**, 1301 (2005).

[34] V. A. Chernenko, J. Pons, E. Cesari and I. K. Zasimchuk, *Transformation behaviour and martensite stabilization in the ferromagnetic Co-Ni-Ga Heusler alloy*, Scr. Mater. **50**, 225 (2004).

[35] K. Oikawa, T. Ota, F. Gejima, T. Ohmori, R. Kainuma and K. Ishida, *Phase equilibria and phase transformations in new B2-type ferromagnetic shape memory alloys of Co-Ni-Ga and Co-Ni-Al systems*, Mater. Trans. **42**, 2472 (2001).

[36] K. Oikawa, L. Wulff, T. Iijima, F. Gelima, T. Ohmori, A. Fujita, K. Fukamichi, R. Kainuma and K. Ishida, *Promising ferromagnetic Ni-Co-Al shape memory alloy*, Appl. Phys. Lett. **79**, 3290 (2001).

[37] M. Wuttig, J. Li and C. Craciunescu, *A new ferromagnetic shape memory alloy system*, Scr. Mater. **44**, 2393 (2002).

[38] C. Craciunescu, Y. Kishi, T. A. Lograsso and M. Wuttig, *Martensitic transformation in Co_2NiGa ferromagnetic shape memory alloys*, Scr. Mater. **47**, 285 (2002).

[39] K. Oikawa, Y. Tanaka, Y. Sutou, T. Omori, F. Luo, R. Kainuma and K. Ishida, *Effects of aging and Co addition on martensitic and magnetic transitions in Ni-Al-Fe* β*-based shape memory alloys*, ISIJ International **46**, 1287 (2006).

[40] K. Oikawa, T. Ota, Y. Tanaka, T. Omori, R. Kainuma and K. Ishida, *Magnetic and martensitic phase transitions in the Ni-Al-Fe shape memory alloys*, Trans. Mater. Res. Soc. Jpn. **28**, 265 (2003).

[41] N. Koeda, Y. Sutou, T. Omori, K. Oikawa, R. Kainuma and K. Ishida, *Martensitic Transformation of Cu-10at.%Al-9at.%Ga-11at.%Mn ferromagnetic* β *alloy*, Scr. Mater. **52**, 1153 (2005).

[42] K. Oikawa, N. Koeda, Y. Sutou, T. Omori, R. Kainuma and K. Ishida, *Martensitic Transformation and Magnetic Properties of Cu-Ga-Mn* β *Alloys*, Mater. Trans. **45**, 2780 (2004).

[43] C. Felser, G. H. Fecher and B. Balke, *Spintronics: a challenge for materials science and solid-state chemistry*, Angew. Chem. Int. Ed. **46**, 668–699 (2007).

[44] L. Mañosa, A. Gonzàlez-Comas, E. Obradó and A. Planes, *Anomalies related to the TA_2-phonon-mode condensation in the Heusler Ni_2MnGa alloy*, Phys. Rev. B **55**, 11068 (1997).

[45] X. Moya, D. Gonzàlez-Alonso, L. Mañosa, A. Planes, V. O. Garlea, T. A. Lograsso, D. L. Schlagel, J. L. Zarestky, S. Aksoy and M. Acet, *Lattice dynamics in magnetic superelastic Ni-Mn-In alloys: Neutron scattering and ultrasonic experiments*, Phys. Rev. B **79**, 214118 (2009).

[46] O. Heczko, S. Fähler, T. M. Vasilchikova, T. N. Voloshok, K. V. Klimov, Y. I. Chumlyakov and A. N. Vasiliev, *Thermodynamic, kinetic, and magnetic properties of a $Ni_{54}Fe_{19}Ga_{27}$ magnetic shape-memory single crystal*, Phys. Rev. B **77**, 174402 (2008).

[47] Q. M. Hu, C. M. Li, R. Yang, S. E. Kulkova, D. I. Bazhanov, B. Johansson and L. Vitos, *Site occupancy, magnetic moments, and elastic constants of off-stoichiometric Ni_2MnGa from first-principles calculations*, Phys. Rev. B **79**, 144112 (2009).

[48] M. Siewert, M. E. Gruner, A. Dannenberg, A. Hucht, S. M. Shapiro, G. Xu, D. L. Schlagel, T. A. Lograsso and P. Entel, *Electronic structure and lattice dynamics of the magnetic shape memory alloy Co_2NiGa*, Phys. Rev. B **82**, 064420 (2010).

[49] G. Barsch and J. Krumhansl, in *Proc. Int. Conf. on Martensitic Transformations (ICOMAT-92)*, p. 53, Monterey Institute of Advanced Studies, California 1993.

[50] P. Entel, M. E. Gruner, A. Hucht, A. Dannenberg, M. Siewert, H. C. Herper, T. Kakeshita, T. Fukuda, V. V. Sokolovskiy and V. D. Buchelnikov, *Phase diagrams of conventional and inverse functional magnetic Heusler alloys: new theoretical and experimental investigations*, in *Topics in Applied Physics*, edited by T. Kakeshita and Y. Kuroda, Springer, Berlin 2011, in print.

[51] S. Ö. Kart, M. Uludoğan, I. Karaman and T. Çağin, *DFT studies on structure, mechanics and phase behavior of magnetic shape memory alloys: Ni_2MnGa* **205**, 1026 (2008).

[52] A. Ayuela, J. Enkovaara and R. M. Nieminen, *Ab initio study of tetragonal variants in Ni_2MnGa alloy*, J. Phys.: Condens. Matter **14**, 5325 (2002).

[53] K. Tsuchiya and K. Marulawa, *The mechanism of rubber-like behavior in Cu-Zn-Al martensite* **5**, C8–901 (1995).

[54] A. Planes, L. Mañosa, E. Vives, J. Rodriguez-Carvajal, M. Morin, G. Guenin and J. L. Macqueron, *Neutron diffraction study of long-range atomic order in Cu-Zn-Al shape memory alloys*, J. Phys.: Condens. Matter **4**, 553 (1992).

[55] A. Gonzàlez-Comas, L. Mañosa, M. Cankurtaran, G. A. Saunders and F. C. Lovey, *Non-linear acoustic properties and acoustic-mode vibrational anharmonicity of 18R martensite Cu-Zn-Al shape-memory alloy*, J. Phys.: Condens. Matter **43**, 9737 (1998).

[56] J. Worgull, E. Petti and J. Trivisonno, *Behavior of the elastic properties near an intermediate phase transition in Ni_2MnGa*, Phys. Rev. B **54**, 15695 (1996).

[57] A. Sozinov, A. A. Likhachev, N. Lanska and K. Ullakko, *Giant magnetic-field-induced strain in NiMnGa seven-layered martensitic phase*, Appl. Phys. Lett. **80**, 1746 (2002).

[58] P. Entel, M. E. Gruner, A. Dannenberg, M. Siewert, S. K. Nayak, H. C. Herper and V. D. Buchelnikov, *Fundamental aspects of magnetic shape memory alloys: insights from ab initio and Monte Carlo studies*, Mater. Sci. Forum **635**, 3–12 (2010).

[59] A. Planes, L. Mañosa and M. Acet, *Magnetocaloric effect and its relation to shape-memory properties in ferromagnetic Heusler alloys*, J. Phys.: Condens. Matter **21**, 233201 (2009).

[60] Y. N. Zhang, J. X. Cao and R. Q. Wu, *Rigid band model fpr prediction of magnetostriction of iron-gallium alloys*, Appl. Phys. Lett. **96**, 062508 (2010).

[61] R. Wu, *Origin of large magnetostriction in FeGa alloys*, J. Appl. Phys. **91**, 7358 (2002).

[62] J. R. Cullen, A. E. Clark, M. Wun-Fogle, J. B. Restor and T. A. Lograsso, *Magnetoelasticity of FeGa and FeAl alloys*, J. Magn. Magn. Mater. **226-230**, 948 (2001).

[63] K. Schwarz, P. Mohn, P. Blaha and J. Kübler, *Electronic and magnetic structure of BCC Fe-Co alloys from band theory*, J. Phys. F: Met. Phys. **14**, 2659 (1984).

[64] J. G. Booth and J. D. Marshall, *Ferromagnetic properties of Co-Ga alloys with B2 structure*, Phys. Lett. **32**, 149 (1970).

[65] T. Takayama, S. Shinohara, K. Ishida and T. Nishizawa, *Anomalies in Phase Equilibra due to Magnetic Transition in Fe-Zn, Co-Zn, and Fe-Co-Zn Systems*, J. Phase Equilib. **16**, 390 (1995).

[66] A. J. Morton, *Inversion Domains in γ-Brass Type Phases*, Phys. Status Solidi (A) **44**, 2205 (1977).

[67] R. Corson, S. Thuanboon and S. Guruswamy, *Processing and study of magnetic and magnetostrictive properties of Fe-Zn alloys*, TMS Annual Meeting p. 221 (2006), Processing and study of magnetic and magnetostrictive properties of Fe-Zn alloys.

[68] H. Numakura, M. Ishimoto and M. Wuttig, *Magnetoelastic damping in Fe-Ga solid solution alloys*, Mater. Sci. Eng. A **442**, 195 (2006).

[69] Z. Lei, J. Cheng-Bao, S. Jia-Xiang and X. Hui-Bin, *First principles study on the magnetocrystalline anisotropy of Fe-Ga magnetostrictive alloys*, Chin. Phys. B **18**, 1647 (2009).

[70] M. Gillessen and R. Dronskowski, *A combinatorial study of full Heusler alloys by first-principles computational methods* ().

[71] E. C. Bain, *Nature of martensite*, Trans. AIME **70**, 25 (1924).

[72] C. M. Wayman, *The growth of martensite since E. C. Bain (1924) - Some milestones*, Mater. Sci. Forum **56-58**, 1 (1990).

[73] H. Ebert, *Fully relativistic band structure calculations for magnetic solids-Formalism and Application*, in *Lecture Notes in Physics*, edited by H. Dreysse, vol. 50, p. 191, Springer, Berlin 2000.

[74] H. Ebert et al, http://olymp.cup.uni-muenchen.de/ak/ebert/SPRKKR.

[75] Hohenberg and Kohn, *Inhomogeneous electron gas*, Phys. Rev. **136**, 864 (1964).

[76] W. Kohn and L. J. Sham, *Self-consistent equations including exchange and correlation effects*, Phys. Rev. **140**, A1133 (1965).

[77] J. Hafner, *Ab-initio simulations of materials using VASP: density-functional theory and beyond*, J. Comput. Chem. **29**, 2044 (2008).

[78] N. Metropolis, A. W. Rosenbluth, M. N. Rosenbluth, A. H. Teller and E. Teller, *Equation of state calculations by fast computing machines*, J. Chem. Phys. **21**, 1087 (1953).

[79] L. H. Thomas, *The calculation of atomic fields*, Proc. Cambridge. Philos. Soc. **23**, 542 (1927).

[80] R. Zeller, *Introduction to Density-Functional Theory*, in *Computational Condensed Matter Physics*, edited by R. G. Winkler, vol. 32, p. A1, Forschungszentrum Jülich GmbH, 52425 Jülich 2006.

[81] S. Blügel, *Density Functional Theory in Practice*, in *Computational Condensed Matter Physics*, edited by R. G. Winkler, vol. 32, p. A8, Forschungszentrum Jülich GmbH, 52425 Jülich 2006.

[82] D. M. Ceperley and B. J. Alder, *Ground state of the electron gas by a stochastic method*, Phys. Rev. Lett. **45**, 566 (1980).

[83] J. P. Perdew, *Electronic structure of solids '91*, Akademie Verlag, Berlin 1991.

[84] J. P. Perdew, K. Burke and M. Ernzerhof, *Generalized gradient approximation made simple* ().

[85] P. Blöchl, *Projector augmented-wave method*, PRB **450**, 17953 (1994).

[86] K. Reuter, C. Stampfl and M. Scheffler, *Methods*, in *Handbook of Materials Modeling*, edited by S. Yip, p. Part A, Springer, Berlin 2005.

[87] K. Binder and D. W. Heermann, *Monte Carlo Simulation in Statistical Physics*, Springer Verlag, Berlin Heidelberg 1988.

[88] M. E. J. Newman and G. T. Barkema, *Monte Carlo Methods in Statistical Physics*, Clarendon Press, Oxford 1999.

[89] G. Kresse and J. Furthmüller, *Efficient iterative schemes for ab initio total-energy calculations using a planewave basis set*, Phys. Rev. B **54**, 11169 (1996).

[90] G. Kresse and D. Joubert, *From ultrasoft pseudopotentials to the augmented-wave method*, Phys. Rev. B **59**, 1758 (1999).

[91] J. P. Perdew, J. A. Chevary, S. H. Vosko, K. A. Jackson, M. R. Pederson, D. J. Singh and C. Fiolhais, *Atoms, molecules, solids, and surfaces: applications of the generalized gradient approximation for exchange and correlation*, Phys. Rev. B **46**, 6671 (1992).

[92] D. Alfè, *PHON: A program to calculate phonons using the small displacement method*, Comput. Phys. Commun. **180**, 2622 (2009).

[93] P. Entel, A. Dannenberg, M. Siewert, H. C. Herper, M. E. Gruner, V. D. Buchelnikov and V. A. Chernenko, *Composition-dependent basics of smart Heusler materials from first-principles calculations*.

[94] P. Entel, A. Dannenberg, M. Siewert, H. C. Herper, M. E. Gruner, D. Comtesse, H.-J. Elmers and M. Kallmeyer, *Basic properties of magnetic shape-memory materials from first-principles calculations*, Metall. Mater. Trans. A (2011), submitted.

[95] S. Aksoy, M. Acet, E. F. Wassermann, T. Krenke, X. Moya, L. Mañosa, A. Planes and P. P. Deen, *Structural properties and magnetic interactions in martensitic Ni-Mn-Sb alloys*, Philos. Mag. **89**, 2093 (2009).

[96] V. A. Chernenko, E. Cesari, V. V. Kokorin and I. N. Vitenko, *The development of new ferromagnetic shape memory alloys in Ni-Mn-Ga system*, Scripta Metall. Mater. **33**, 1239 (1995).

[97] K. Ullakko, Y. Ezer, A. Sozinov, G. Kimmel, P. Yakovenko and V. Lindroos, *Magnetic-field-induced strains in polycrystalline Ni-Mn-Ga at room temperature*, Scr. Mater. **44**, 475 (2001).

[98] N. Lanska, O. Söderberg, A. Sozinov, Y. Ge, K. Ullakko and V. K. Lindroos, *Composition and temperature dependence of the crystal structure of Ni-Mn-Ga alloys*, J. Appl. Phys. **95**, 8074 (2004).

[99] V. V. Khovaylo, V. D. Buchelnikov, R. Kainuma, V. V. Koledov, M. Ohtsuka, V. G. Shavrov, T. Takagi, S. V. Taskaev and A. N. Vasiliev, *Phase transitions in $Ni_{2+x}Mn_{1-x}Ga$ with a high Ni excess*, Phys. Rev. B **72**, 224408 (2005).

[100] M. Richard, J. Feuchtwanger, D. Schlagel, T. Lograsso, S. Allen and R. O'Handley, *Crystal structure and transformation behavior of Ni-Mn-Ga martensites*, Scr. Mater. **54**, 1797 (2006).

[101] E. Wachtel, F. Henninger and B. Predel, *Constitution and magnetic properties of Ni-Mn-Sn alloys - solid and liquid state*, J. Magn. Magn. Mater. **38**, 305 (1983).

[102] T. Krenke, M. Acet, E. F. Wassermann, X. Moya, L. Mañosa and A. Planes, *Martensitic transitions and the nature of ferromagnetism in the austenitic and martensitic states of Ni-Mn-Sn alloys*, Phys. Rev. B **72**, 014412 (2005).

[103] T. Krenke, M. Acet, E. F. Wassermann, X. Moya, L. Mañosa and A. Planes, *Ferromagnetism in the austenitic and martensitic states of Ni-Mn-In alloys*, Phys. Rev. B **73**, 174413 (2006).

[104] J. Du, Q. Zheng, W. J. Ren, W. J. F. amd X. G. Liu and Z. D. Zhang, *Magnetocaloric effect and magnetic-field-induced shape recovery effect at room temperature in ferromagnetic Heusler alloy Ni-Mn-Sb*, J. Phys. D: Applied Physics **40**, 5523 (2007).

[105] S. Y. Yu, L. Ma, G. D. Liu, Z. H. Liu, J. L. Chen, Z. X. Cao, G. H. Wu, B. Zhang and X. X. Zhang, *Magnetic field-induced martensitic transformation and large magnetoresistance in NiCoMnSb alloys*, Appl. Phys. Lett. **90**, 242501 (2007).

[106] S. Chatterjee, S. Giri, S. Majumdar, A. K. Deb, S. K. De and V. Hardy, *Magneto-structural instability in $Ni_2Mn_{1.4}Sb_{0.6}$ alloy*, J. Phys.: Condens. Matter **19**, 346213 (2007).

[107] M. Khan, I. Dubenko, S. Stadler and N. Ali, *Inverse magnetocaloric effect in ferromagnetic $Ni_{50}Mn_{37+x}Sb_{13-x}$ Heusler alloys*, J. Appl. Phys. **101**, 053919 (2007).

[108] M. Khan, N. Ali and S. Stadler, *Magnetostructural phase transitions in $Ni_{50}Mn_{25+x}Sb_{25-x}$ Heusler alloys*, J. Phys.: Condens. Matter **20**, 235204 (2008).

[109] L. Mañosa, X. Moya, A. Planes, S. Aksoy, M. Acet, E. F. Wassermann and T. Krenke, *Magnetostrain in Multifunctional Ni-Mn Based Magnetic Shape Memory Alloys*, Mater. Sci. Forum **583**, 111 (2008).

[110] M. Siewert *et al.*, unpublished.

[111] M. A. Uijttewaal, T. Hickel, J. Neugebauer, M. E. Gruner and P. Entel, *Understanding the phase transitions of the Ni_2MnGa magnetic shape memory system from first-principles*, Phys. Rev. Lett. **102**, 035702 (2009).

[112] V. D. Buchelnikov, P. Entel, S. V. Taskaev, V. V. Sokolovskiy, A. Hucht, M. Ogura, H. Akai, M. E. Gruner and S. K. Nayak, *Monte Carlo study of the influence of antiferromagnetic exchange interactions on the phase transitions of ferromagnetic Ni-Mn-X alloys (X=In,Sn,Sb)*, Phys. Rev. B **78**, 184427 (2008).

[113] S. Aksoy, T. Krenke, M. Acet, E. F. Wassermann, X. Moya, L. Mañosa and A. Planes, *Tailoring magnetic and magnetocaloric properties of martensitic transitions in ferromagnetic Heusler alloys*, Appl. Phys. Lett. **91**, 241916 (2007).

[114] M. Sato, T. Okazaki, Y. Furuya, Y. Kishi and M. Wuttig, *Phase transformation and magnetic property of Heusler type Co_2NiGa alloys*, Mater. Trans. **45**, 204 (2004).

[115] S. E. Kulkova, S. S. Kulkov and A. V. Subashiev, *Ab-initio investigation of electronic and magnetic properties of Heusler alloys*, Comput. Mater. Sci. **36**, 249 (2006).

[116] R. Ducher, R. Kainuma and K. Ishida, *Phase equilibria in the Ni-Co-Ga system*, J. Alloys Compd. **466**, 208–213 (2008).

[117] J. Gil and J. M. Guilemany, *Pseudoelastic hysteresis in Cu-Zn-Al shape memory single crystals*, J. Mater. Sci. Lett. **11**, 493 (1992).

[118] W. H. Zou, C. W. H. Lam, C. Y. Chung and J. K. L. Lai, *Microstructural studies of a Cu-Zn-Al shape-memory alloy with manganese and zirconium addition*, Metall. Mater. Trans. A **29**, 1865 (1998).

[119] P. Entel, V. D. Buchelnikov, V. V. Khovailo, A. T. Zayak, W. A. Adeagbo, M. E. Gruner, H. C. Herper and E. F. Wassermann, *Modelling the phase diagram of magnetic shape memory alloys*, J. Phys. D: Appl. Phys. **39**, 865 (2006).

[120] J. Liu and J. Li, *Magnetic force microscopy observations of Co-Ni-Ga and Co-Ni-Al alloys with two-phase structures*, Scr. Mater. **55**, 755 (2006).

[121] X. F. Dai, G. D. Liu, Z. H. Liu, G. H. Wu, J. L. Chen, F. B. Meng, H. Y. Liu, L. Q. Yan, J. P. Qu and L. Y. X. et al., *Superelasticity of CoNiGa:Fe single crystals*, Appl. Phys. Lett. **87**, 112504 (2005).

[122] K. C. Hass, L. C. Davis and A. Zunger, *Electronic structure of random $Al_{0.5}Ga_{0.5}As$ alloys: Test of the special-quasirandom-structures description*, Phys. Rev. B **42**, 3757 (1990).

[123] A. Zunger, S.-H. Wei, L. G. Ferreira and J. E. Bernard, *Special quasirandom structures*, Phys. Rev. Lett. **65**, 353 (1990).

[124] S. Wei, L. G. Ferreira, J. E. Bernard and A. Zunger, *Electronic properties of random alloys: Special quasirandom structures*, Phys. Rev. B **42**, 9622 (1990).

[125] N. K. Jaggi, K. R. P. M. Rao, A. K. Grover, L. C. Gupta, R. Vijayaraghavan and L. D. Khoi, *Mössbauer and NMR study of site preference and local environement effects in Co_2FeGa and Fe_2CoGa*, Hyperfine Interactions **4**, 402 (1978).

[126] K. Buschow and P. van Engen, *Magnetic and magneto-optical properties of Heusler alloys based on Aluminium and Gallium*, J. Magn. Magn. Mater. **25**, 90–96 (1981).

[127] R. Y. Umetsu, K. Kobayashi, A. Fujita, K. Oikawa, R. Kainuma, K. Ishida, N. Endo, K. Fukamichi and A. Sakuma, *Magnetostructural phase transitions in $Ni_{50}Mn_{25+x}Sb_{25-x}$ half-metallic properties of $Co_2(Cr_{1-x}Fe_x)Ga$ Heusler alloys*, Phys. Rev. B **72**, 214412 (2005).

[128] L. Basit, C. Wang, C. A. Jenkins, B. Balke, V. Ksenofontov, G. H. Fecher, C. Felser, E. Mugnaioli, U. Kolb, S. A. Nepijko, G. Schönhense and M. Klimenkov, *Heusler compounds as ternary intermetallic nanoparticles: Co_2FeGa*, J. Phys. D: Applied Physics **42**, 084018 (2009).

[129] A. Dannenberg, M. Siewert, M. E. Gruner, M. Wuttig and P. Entel, *Competing structural ordering tendencies in Heusler-type alloys with high Curie temperatures: $Fe_2CoGa_{1-x}Zn_x$ studied by first-principles calculations*, Phys. Rev. B **82**, 214421 (2010).

[130] Y. N. Zhang, J. X. Cao and R. Q. Wu, *Rigid band model for prediction of magnetostriction of iron-gallium alloys*, Appl. Phys. Lett. **96**, 062508 (2010).

[131] A. R. Williams, V. L. Moruzzi, J. C. D. Gelatt, J. Kübler and K. Schwarz, *Aspects of transition-metal magnetism*, J. Appl. Phys. **53**, 2019 (1982).

[132] A. T. Zayak, W. A. Adeagbo, P. Entel and K. M. Rabe, e/a *dependence of the lattice instability of cubic Heusler alloys from first principles*, Appl. Phys. Lett. **88**, 111903 (2006).

[133] R. Dronskowski and P. E. Blöchel, *Crystal orbital Hamilton populations (COHP): energy-resolved visualization of chemical bonding in solids based on density-functional calculations*, J. Phys. Chem. **97**, 8617 (1993).

[134] I. Galanakis, P. H. Dederichs and N. Papanikolaou, *Slater-Pauling behaior and origin of the half-metallicity of the full-Heusler alloys*, Phys. Rev. B **66**, 174429 (2002).

[135] H. C. Herper *et al.*, unpublished.

[136] M. E. Gruner *et al.*, unpublished.

[137] A. R. Williams, R. Zeller, V. L. Moruzzi, C. D. Gelatt and J. Kubler, *Covalent magnetism: An alternative to the Stoner model*, J. Appl. Phys. **52**, 2067 (1981).

[138] A. Kashyap, K. B. Garg, A. K. Solanki, T. Nautiyal and S. Auluck, *Electronic structure, fermi surface, and Curie temperature calculations for the Co-Pt system*, Phys. Rev. B **29**, 1620 (1984).

[139] K. Terakura, *The electronic structure of non-transition element impurity atoms in iron and nickel*, Physica B **91**, 162 (1977).

[140] K. Terakura and J. Kanamori, *A calculation of the electronic structure of an impurity atom of non-transition element in nickel*, Prog. Theor. Phys. **46**, 1007 (1971).

[141] A. Williams, V. Moruzzi, A. Malozemoff and K. Terakura, *Generalized Slater-Pauling curve for transition-metal magnets*, IEEE Trans. Magn. **19**, 1983 (1983).

[142] G. D. Liu, J. L. Chen, Z. H. Liu, X. F. Dai, G. H. Wu, B. Zhang and X. X. Zhang, *Martensitic transformation and shape memory effect in a ferromagnetic shape memory alloy: Mn_2NiGa*, Appl. Phys. Lett. **87**, 262504 (2005).

[143] P. J. Brown, T. Kanomata, K. Neumann, K. U. Neumann, B. Ouladdiaf, A. Sheikh and K. R. A. Ziebeck, *Atomic and magnetic order in the shape memory alloy Mn_2NiGa*, J. Phys.: Condens. Matter **22**, 506001 (2010).

[144] G. D. Liu, X. F. Dai, S. Y. Yu, Z. Y. Zhu, J. L. Chen and G. H. Wu, *Structure and perpendicular magnetic anisotropy of a new $CoPt_x$ alloy grown by MBE*, JMMM **193**, 166 (1999).

[145] S. R. Barman, S. Banik, A. K. Shukla, C. Kamal and A. Chakrabarti, *Martensitic transition, ferrimagnetism and Fermi surface nesting in Mn_2NiGa*, Europhys. Lett. **80**, 57002 (2007).

[146] K. Oikawa, T. Ota, T. Ohmori, Y. Tanaka, H. Morito, A. Fujita, R. Kainuma, K. Fukamichi, R. Kainuma and K. Ishida, *Magnetic and martensitic phase transitions in the Ni-Ga-Fe shape memory alloys*, Appl. Phys. Lett. **81**, 5201 (2002).

[147] H. Morito, A. Fujita, K. Fukamichi, R. Kainuma, K. Ishida and K. Oikawa, *Magnetic-field-induced strain of Fe-Ni-Ga in single-variant state*, Appl. Phys. Lett. **83**, 4993 (2003).

[148] K. Oikawa, T. Ota, Y. Sutou, T. Ohmori, R. Kainuma and K. Ishida, *Magnetic and martensitic phase transformations in a $Ni_{54}Ga_{27}Fe_{19}$ alloy*, Mater. Trans. **43**, 2360 (2002).

[149] K. Oikawa, Y. Imano, V. A. Chernenko, F. Luo, T. Omori, Y. Sutou, R. Kainuma, T. Kanomata and K. Ishida, *Influence of Co addition on martensitic and magnetic transitions in Ni-Fe-Ga-based shape memory alloys*, Mater. Trans. **46**, 734 (2005).

[150] J. Liu, N. Scheerbaum, D. Hinz and O. Gutfleisch, *A high-temperature coupling of martensitic and magnetic transformations and magnetic entropy changes in Ni-Fe-Ga-Co alloys*, Scr. Mater. **59**, 1063 (2008).

[151] H. Okamoto, *Co-Fe (Cobalt-Iron)*, J. Phase Equilib. Diff. **29**, 383 (2008).

[152] S. Weiss and M. Wuttig and S. Fähler *et al.*, unpublished.

[153] I. Titov and M. Acet *et al.*, unpublished.

[154] A. Zheludev, S. M. Shapiro, P. Wochner and L. E. Tanner, *Precursor effects and premartensitic transformation in Ni_2MnGa*, Phys. Rev. B **54**, 15045–15050 (1996).

[155] D. Comtesse *et al.*, unpublished.

[156] A. L. Roytburd and J. Slutsker, *Deformation of adaptive materials. Part I. Constrained deformation of polydomain crystals*, J. Mech. Phys. Solids **47**, 2299 (1999).

[157] A. L. Roytburd and J. Slutsker, *Deformation of adaptive materials. Part II. Adaptive composite*, J. Mech. Phys. Solids **47**, 2331 (1999).

[158] A. L. Roytburd and J. Slutsker, *Deformation of adaptive materials. Part III. Deformation of crystals with polytwin product phases*, J. Mech. Phys. Solids **47**, 1795 (2001).

[159] A. G. Khachaturyan, S. M. Shapiro and S. Semenovskaya, *Adaptive phase formation in martensitic transformation*, Phys. Rev. B **43**, 10832 (1991).

[160] S. Kaufmann, R. Niemann, T. Thersleff, U. K. Rößler, O. Heczko, J. Buschbeck, B. Holzapfel, L. Schultz and S. Fähler, *Modulated martensite: why it forms and why it deforms easily*, New J. Phys. **108** (2011), accepted.

[161] Y. M. Jin, Y. U. Wang, A. G. Khachaturyan, J. F. Li and D. Viehland, *Conformal miniaturization of domains with low domain-wall energy: monoclinic ferroelectric states near the morphotropic phase boundaries*, Phys. Rev. Lett. **91**, 197601 (2003).

[162] A. Sozinov, A. A. Likhachev, N. Lanska and K. Ullakko, *Giant magnetic-field-induced strain in NiMnGa seven-layered martensitic phase*, Appl. Phys. Lett. **80**, 1746 (2002).

[163] A. G. Khachaturyan, Zh. Eksp. Teor. Fiz. **56**, 1037 (1969).

[164] A. L. Roytburd, Fiz. Tverd. Tela (Leningrad) **10**, 3619 (1968).

[165] M. E. Gruner, private communications.

[166] M. Siewert, A. Dannenberg, A. Chakrabarti, P. Entel, T. Hickel, A. Al-Zubi, J. Neugebauer, M. Gillessen and R. Dronskowski, *Designing shape-memory Heusler alloys from first-principles*, Appl. Phys. Lett. (2011), submitted.

[167] M. E. Gruner, unpublished.

12 Acknowledgements

At the end of my thesis I would like to thank all people which have been involved in the creative process of this work. First of all, I would like to express my gratitude to my thesis supervisor Prof. Dr. Peter Entel and my colleague Markus Ernst Gruner. Prof. Dr. Peter Entel inspired me with never-ending new ideas and helpful discussions and I'm very glad that he gave me the opportunity to work and write my thesis in his group. I am very grateful for the competent assistance and the full support supplied by Markus E. Gruner concerning computational as well as physical questions. His numerous advices and clever ideas significantly shaped my research at the group of Prof. Entel. Special thanks goes to his patience with all my queries which I addressed to him regarding all kinds of physical topics. He carefully read this manuscript and gave useful criticism.

I would also like to thank Heike C. Herper and Dr. Alfred Hucht for their assistance concerning my calculations and the variety of problems encountered during the development of this thesis. With respect to computer facilities I always obtained full support from our system administrator Dr. Alfred Hucht.

Especially the discussions with Mario Siewert were very illuminating and helpful and my work benefited a lot from the mutual inspiration. The collaboration with Dr. Aparna Chakrabarti was also very enlightening and I'm thankful for her reading of this manuscript and her critical notations.

I also thank Prof. Manfred Wuttig for his inspirations and cooperation.

I very much thank all my colleagues for the pleasant atmosphere which supported working in our group.

In addition, I really want to express my gratitude to my family, my partner and my friends. Especially my mother helped me wherever possible and took care of me during this work. In my childhood my father inspired me with his fascinating stories about the miracles in everyday physics.

I acknowledge the financial support by the Deutsche Forschungsgemeinschaft (SPP1239).

13 Publications

Part of this work has been published in:

1. A. Dannenberg, M. Siewert, M. Wuttig and P. Entel, *Competing structural ordering tendencies in Heusler-type alloys with high Curie temperatures: $Fe_2CoGa_{1-x}Zn_x$ studied by first-principles calculations*, Phys. Rev. B **82**, 214421 (2010).

2. A. Dannenberg, M. E. Gruner, A. Hucht and P. Entel, *Surface energies of stoichiometric FePt and CoPt alloys and their implications for nanoparticle morphologies*, Phys. Rev. B **80**, p. 245438 (2009).

3. A. Dannenberg, M. E. Gruner, M. Wuttig and P. Entel, *Characterization of new ferromagnetic Fe-Co-Zn-Ga alloys by ab initio investigations*, in *ESOMAT 2009 - The 8th European Symposium on Martensitic Transformations*, edited by P. Šittner, L. Heller and V. Paidar, no. 04004, pp. 1200–Go4–03, EDP Sciences (www.esomat.org), Berlin 2009, DOI: 10.1051/esomat/200904004.

4. A. Dannenberg, M. E. Gruner, M. Wuttig and P. Entel, *First-principle study of ferromagnetic $Ni_2CoGa(Zn)$ alloys in the Heusler and the inverse Heusler structure*, Mater. Res. Soc. Symp. Proc. **1200E**, 1200–G04–03 (2010).

5. A. Dannenberg, M. E. Gruner, M. Wuttig and P. Entel, *Structural ordering tendencies in the new ferromagnetic Ni-Co-Fe-Ga-Zn Heusler alloys*, Physics Procedia **10**, 144–148 (2010).

6. A. Dannenberg, M. E. Gruner and P. Entel, *First-principles study of the structural stability of $L1_1$ order in Pt-based alloys*, Journal of Physics: Conference Series 200, p. 072021 (2010).

7. P. Entel, A. Dannenberg, M. Siewert, H. C. Herper, M. E. Gruner, V. D. Buchelnikov and V. A. Chernenko, *Composition-dependent basics of smart Heusler materials from first-principles calculations*, in *Ferromagnetic Shape Memory Alloys III*, edited by V. A. Chernenko, Mater. Sci. Forum **684**, p. 1–29 (2011).

8. P. Entel, M. E. Gruner, G. Rollmann, A. Hucht, S. Sahoo, A. T. Zayak, H. C. Herper, A. Dannenberg, *First-principles investigations of multimetallic transition metal clusters*, Phil. Mag. **88**, p. 2725 (2008).

9. M. E. Gruner and A. Dannenberg, *Structure and magnetism of near-stoichiometric FePd nanoparticles*, JMMM **321**, p. 861 (2009).

10. P. Entel, A. Dannenberg, M. Siewert, H. C. Herper, M. E. Gruner, D. Comtesse, H.-J. Elmers and M. Kallmeyer, *Basic Properties of Magnetic Shape-Memory Materials from First-Principles Calculations*, Metall. Mater. Trans. A (2011), submitted.

11. P. Entel, M. E. Gruner, A. Dannenberg, M. Siewert, S. K. Nayak, H. C. Herper and V. D. Buchelnikov, *Fundamental aspects of magnetic shape memory alloys: Insights from ab initio and Monte Carlo studies*, Mater. Sci. Forum **635**, 3–12 (2010).

12. P. Entel, M. E. Gruner, A. Hucht, A. Dannenberg, M. Siewert, H. C. Herper, T. Kakeshita, T. Fukuda, V. V. Sokolovskiy and V. D. Buchelnikov, *Phase diagrams of conventional and inverse functional magnetic Heusler alloys: New theoretical and experimental investigations*, in *Topics in Applied Physics*, edited by T. Kakeshita and Y. Kuroda, Springer, Berlin 2011, in print.

13. M. Siewert, M. E. Gruner, A. Dannenberg, A. Hucht, S. M. Shapiro, G. Xu, D. L. Schlagel, T. A. Lograsso and P. Entel, *Electronic structure and lattice dynamics of the magnetic shape memory alloy Co_2NiGa*, Phys. Rev. B **82**, 064420 (2010).

14. M. Siewert, A. Dannenberg, A. Chakrabarti, P. Entel, T. Hickel, A. Al-Zubi, J. Neugebauer, M. Gillessen and R. Dronskowski, *Designing shape-memory Heusler alloys from first-principles*, Appl. Phys. Lett., submitted (2011).

15. P. Entel, M. Siewert, A. Dannenberg, M. E. Gruner and M. Wuttig *New functional magnetic shape memory alloys from first-principles calculations*, Mater. Res. Soc. Symp. Proc. **1200**, 1200–G04–01 (2009).

14 Erklärung

Die vorliegende Dissertation reiche ich zum Erlangen des Doktors der Naturwissenschaften (Dr. rer. nat.) gemäß §1 Satz 2 der Promotionsordnung der Fakultät für Physik der Universität Duisburg-Essen ein.

Ich erkläre hiermit, dass ich die Dissertation in keinem weiteren Verfahren eingereicht habe.

Die Dissertation habe ich selbstständig verfasst, alle Hilfsmittel und Quellen sind angegeben und wörtliche oder sinngemäße Zitate entsprechend gekennzeichnet.

Duisburg, den

Unterschrift